X-ray diagnostics of the SPEED2 focus plasma.

I n a u g u r a l - D i s s e r t a t i o n

zur

Erlangung des Doktorgrades der

Mathematisch-Naturwissenschaftlichen Fakultät

der Heinrich-Heine-Universität Düsseldorf

vorgelegt von

Denis Glouchkov

aus Orehovo-Zuevo

Düsseldorf 2001

Gedruckt mit der Genehmigung der Mathematisch-Naturwissenschaftlichen Fakultät
der Heinrich-Heine-Universität Düsseldorf

Referent:	Prof. Dr. W. Kies
Korreferent:	Prof. Dr. D. Reiter
Tage der mündlichen Prüfung:	10.07.2001, 12.07.2001, 13.07.2001

Abstract

SPEED2 is a unique plasma focus device with short current rise time (400ns) able to drive high currents (2.5 MA) through a load. At voltage 300kV, the maximum energy stored in the driver is 187kJ. The discharge is initiated in a deuterium pre-filled chamber, with injection of heavy gases (Argon, Neon) along the discharge axis in the region above the anode.

Discharges produced in the SPEED2 are divided into two modes, at which the produced plasma distinctly has different configurations – a micropinch mode (MPM) and a stable column mode (SCM). The SCM is characterized by forming homogeneous stable plasma columns. In the MPM with injection of high-Z gases instabilities and micropinches are observed. The SCM is favored by high energy densities of the plasma sheaths, while the MPM is achieved at low energy densities. In the transition regime both plasma configurations can be observed. At constant energy of the current driver the discharge mode can be influenced by changing the amount of injected gas and/or the atomic number.

In order to prove that the SCM regime can be established in low-energy machines, the energy of the SPEED2 was decreased to 37kJ and to smaller anode dimensions. To ensure the SCM operating regime Neon was used for injection. The pinch plasma was studied with time-integrated and time-resolved imaging as well as with X-ray spectroscopy. On time-integrated X-ray images bright column-like plasma structures <0.5 mm in diameter, ≤ 4mm in length radiating in a wavelength region below 2nm embedded within diffuse plasma columns 1.4-1.8 mm in diameter, 10-20 mm in length were observed. Temperatures of the bright plasma column were determined by comparing image optical densities behind different filters. It was found that 1-2keV can be achieved, which is much hotter than that of the diffuse column.

With time-resolved pinhole imaging, formation and evolution of plasma columns were observed. Simultaneously spectroscopy of K-ions with spatial and temporal resolution allowed for determining plasma parameters along the discharge axis during the pinch phase. The electron temperature was determined from the intensity ratio of dielectronic satellites to the resonance line of H-like neon. The electron density was determined from the intensity ratio of the resonance (W) to the intercombination (Y) line of He-like neon.

After plasma sheath stagnation on axis, plasma columns with temperatures about 400eV and densities $5 \cdot 10^{24}$ m^{-3} (determined from the W/Y ratio) are formed. Relative line intensities in the group of satellites to the resonance line of H-like neon indicate that densities of about 10^{27} m^{-3} can be achieved. These two results show that plasma columns have a radial density and temperature distribution.

Large-scale instabilities (m=0 mode) are then actuated near the anode, which develop into columns ≤0.3mm in diameter and ≤4mm in lengths with electron densities above $2 \cdot 10^{25}$ m^{-3}. Particle outflow from the compressed regions results in stronger heating of the instability actuated small plasma columns.

With the new discharge parameters SPEED2 was operated in the transition regime. The energy density presumably cannot be straightforwardly scaled with the parameters anode diameter and stored energy only. The quality of the initially produced current sheath or the energy coupling to the final pinch plasma could have changed with this configuration. Additional parameters influencing the SCM should be taken into account. Therefore further studies of the SCM mode in small-scale experiments are necessary.

Table of contents

1 Dynamical pinches

1.1 Apparatus

Electrode coupled dynamical pinches like z-pinches or plasma foci produce hot (up to 1keV) and dense (up to 10^{26} m^{-3}) pinch plasmas that are under investigation for more than four decades.

The common feature of most of these experiments is the production of a plasma sheath in a fill gas on the surface of a dielectric insulator that is dynamically accelerated and compressed on the axis of symmetry (z-axis) by **j**×**B** forces (where **j** is the current density and **B** is the self magnetic field of the current sheath). Finally, this current carrying plasma tube forms a cylinder, the pinch plasma, the equilibrium of which is given by the so-called Bennett-relation [Bennett 1934]

$$\frac{\mu_0 I^2}{8\pi} = (Z+1)N_i kT, \qquad \textbf{Eq 1-1}$$

where μ_0 is the magnetic field constant ($4\cdot10^{-7}$ V·s/A·m), I the pinch current, Z the effective charge number, N_i the ions per unit length, k the Boltzmann constant (k=1.38·10^{-23} J/K) and T the plasma temperature ($T=T_e=T_i$). Figure 1-1 schematically shows the configuration of these pinches.

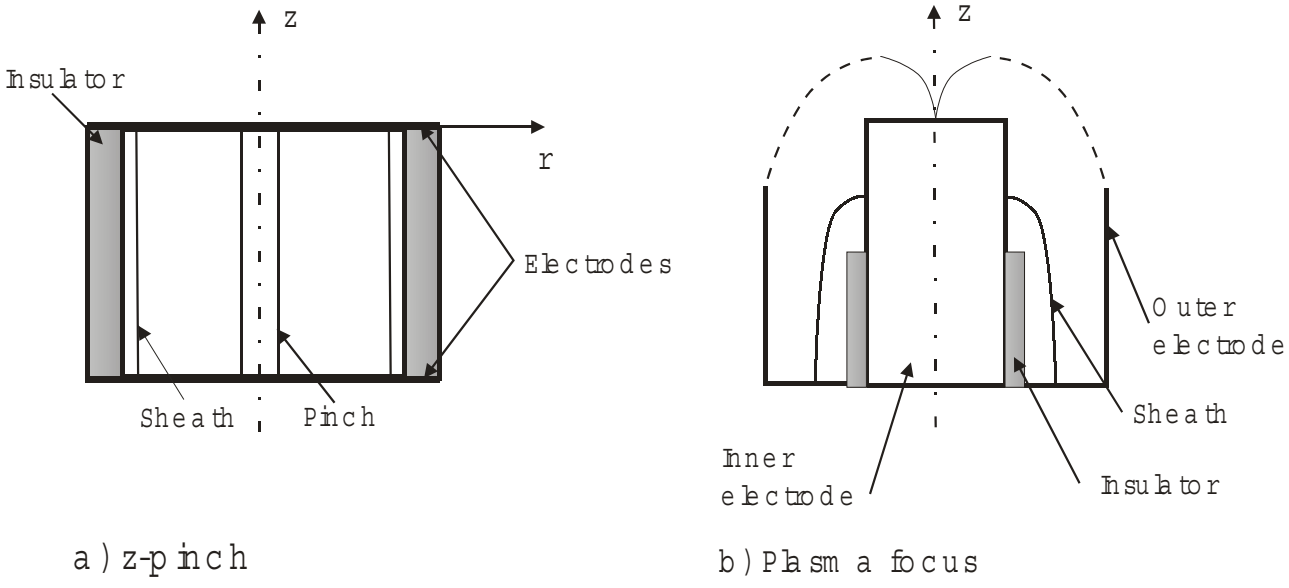

Figure 1-1. Configurations of dynamical pinches

Neither shape or structure nor radial dimensions r of the pinch plasma are determined by this relation. However, maximizing the plasma energy density

$$nkT = \frac{\mu_0}{8\pi^2}\left(\frac{I}{r}\right)^2 \qquad \textbf{Eq 1-2}$$

(with n=(Z+1)·N_i·πr^2) requires large pinch currents and small pinch radii, which means maximizing the current transfer from the driver (capacitor bank) to the load (the pinch) and limiting the line density. This requires thin plasma sheaths which depend on initial conditions (current rise rate $\boldsymbol{I_{dot}}$ and filling pressure $\boldsymbol{p}$) and accelerator dimensions (length and radius of insulator and/or electrodes).

On the other hand, too low line density and thus too high temperatures (see eq. 1.1) result in high plasma pressure so that equilibrium (stagnation) might be established at too large pinch radius, so cooling of the pinch by additional radiative losses could make the pinch shrink to small radial dimensions.

Pease [Pease 1957] and independently Braginskii [Braginskii 1961] showed that ohmic heating of the pinch could be balanced by Bremsstrahlung loss at a critical current level, called the Pease-Braginskii current that for hydrogen plasmas is about 1.5MA and much less for high Z filling gases.

1.2 Driver-load impedance requirements

Initially, dynamical pinches were explored as nuclear fusion sources. A scaling of the fusion yield Y with the driver (bank) energy W empirically found with comparatively slow drivers [Rapp 1973] $Y = 10^7 \cdot W_{kJ}^2$ favored high-energy drivers for pinches as neutron sources. Yield saturation at high driver energy were then explained by current losses since a more physical scaling [Decker et al 1980] $Y = 10^{11} \cdot I_{p,\mathrm{MA}}^4$, ($I_p$ is the pinch current) showed good agreement for all experiments. Little attention was paid to the problem of driver-load impedance requirements and the current transfer to the pinch. From the current scaling and also from eqs. 1.1 and 1.2 it is obvious that the pinch current is the figure of merit rather than driver energy. Trying to enhance the current via increasing the bank energy by increasing the capacitance C_0 at a fixed voltage level (U_0=20 to 40kV) is successful only as long as the driver impedance $Z=(L_0/C_0)^{1/2}$ is larger than the load impedance L_{dot}+R (where L_0, L_{dot}, the time derivative are the driver and load inductance, respectively and L_{dot} and R the plasma impedance). Unfortunately, this procedure soon results in low impedance drivers since also L_0 is decreased and the current is determined by the load behavior $I=U_0/(L_{dot}+R)$ and conventional large banks therefore acted as voltage sources unfit to drive a highly reactive

load like a dynamical pinch. On the other hand a current source, requiring $Z>>L_{dot}+R$ and a large pinch current is not at all easy to realize since the time dependent load impedance rises steeply at pinch compression. Figure 1-2 schematically depicts the load impedance evolution during the discharge. For comparison two constant driver impedances Z_1 and Z_2 are given, Z_1 representing the typical situation of a conventional driver.

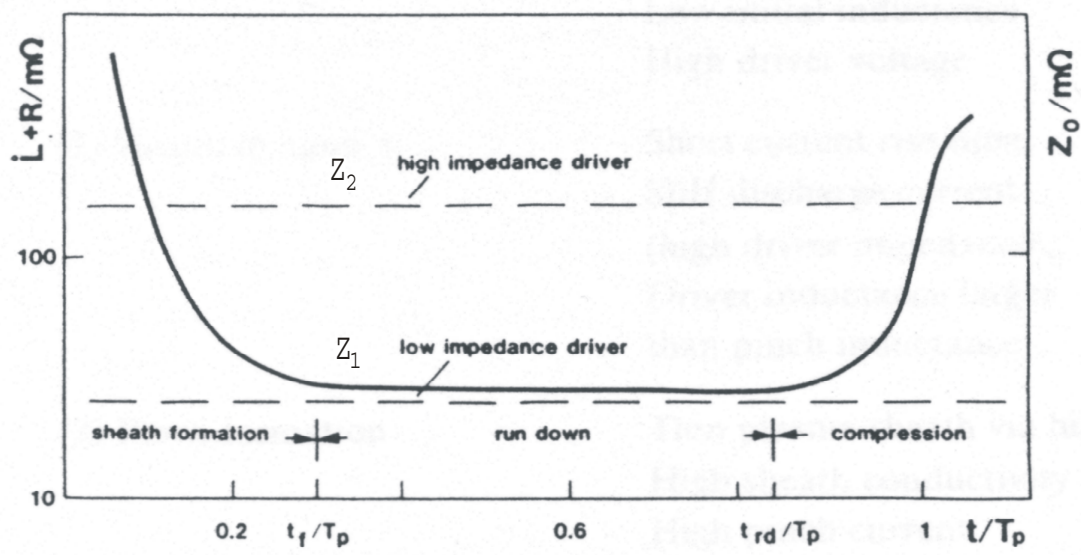

Figure 1-2: Schematic

The current I delivered to the load (discharge current) is

$$I = \frac{U_0}{Z + L_{dot} + R} \qquad \textbf{Eq 1-3}$$

and only approaches maximum (short circuit) current $I_0=(2W/L_0)^{1/2}$ if $Z>>L_{dot}+R$ which is practically not achievable at least not during compression. This leads to early and strong current damping by the load in conventional experiments, but also to late (but short and less) damping with high-impedance drivers.

1.3 High impedance and fast drivers SPEED.

The purpose of the driver concept SPEED at Düsseldorf University was (i) to increase the current efficiency I/W of a bank with a given energy $W = 1/2 \cdot C_0 U_0^2$ and (ii) to improve the current transfer to the pinch plasma. Thus not only the inductance L_0 was to be decreased but also the capacitance C_0 in order to enhance the driver impedance. This inevitably results in high voltage and fast drivers since also the current rise time $\tau = \frac{1}{2}\pi\sqrt{L_0 C_0}$ is decreased.

Since pinch stagnation (stop of dynamical compression) should take place at maximum magnetic flux ($\Phi=L\cdot I$) the accelerator of these experiments is extremely short.

Figure 1-3 shows the configuration of the SPEED2 plasma focus with typical dimensions. (Additionally shown is the gas injection system for heavy gases into the pinch region).

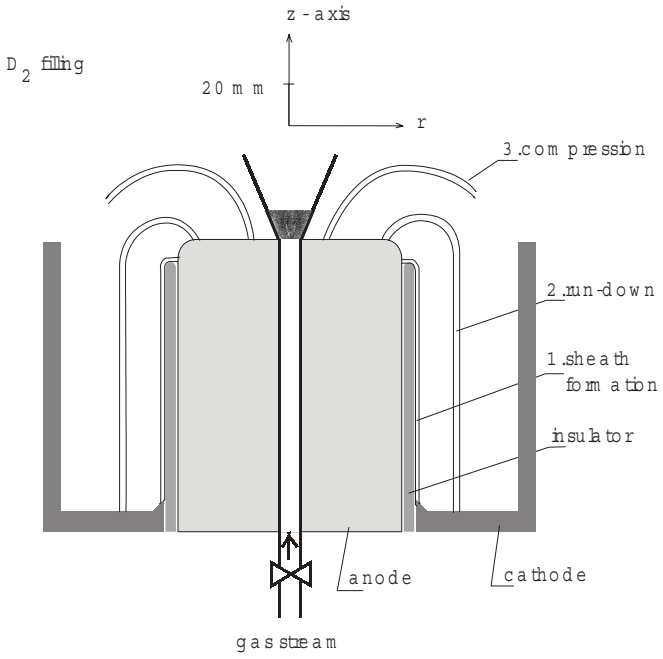

Figure 1-3: Configuration of the SPEED2 plasma focus

The discharge current derivative $I_{dot}(t)$ and the voltage U(t), as shown in the discharge equivalent electric circuit of Figure 1-4,

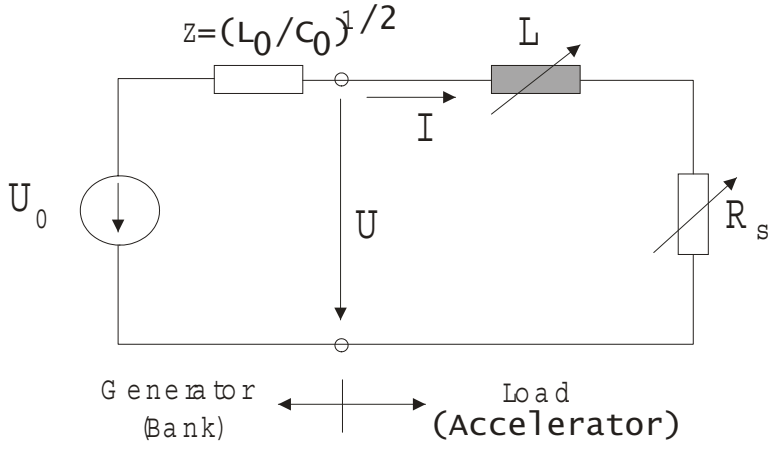

Figure 1-4. Equivalent circuit.

are measured at the breech of the accelerator and two time-correlated typical signals are shown in Figure 1-5.

The compression phase is distinctly realized from the steep spike in the I_{dot} signal that depicts current damping via high values of L_{dot} (exceeding the driver impedance) whereas the

later pinch voltage spike mainly is due to anomalous enhancement of the plasma resistance R at late compression that preferably takes place at low deuterium filling pressure and the earlier the more the filling is contaminated by high Z impurities or heavy doping gases. A detailed analysis of these signals is given in [Decker et al.1983]. Pure deuterium filling (a few mbar) was used for nuclear fusion

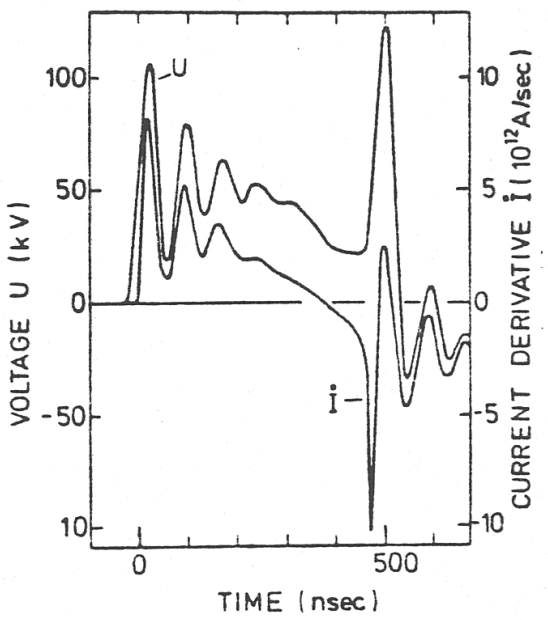

Figure 1-5: Time-correlated typical dI/dt and voltage signals

investigation, injection of heavy gases into the deuterium filling increases the radiation loss from the pinch and is used for investigations of the pinch as a plasma radiation source the latter being exclusively the subject of this work.

Table 1-1: Characteristics of the SPEED devices.

		SPEED1	SPEED2
Energy, (max.)	W [kJ]	30	187
Voltage, (max.)	U_0 [kV]	200	300
Capacitance	C [µF]	1.56	4.16
Inductance	L_0 [nH]	40	15
Short circuit current	I_0 [MA]	1.5	5
Pinch current	I_p [MA]	1.1	3
Initial current rise	I_{dot} [TA/s]	4	20
Current rise time	$\tau/4$ [ns]	400	400
Impedance	Z [mΩ]	160	60

Nevertheless, the discharges are always initiated in pure deuterium since (i) the high power input does not allow premixed fillings and (ii) neutron pulse traces (signals) and yields serve as sensitive indicators of sheath and pinch conditions.

1.4 Pinch phenomena

The clear picture of pinch experiments pointed out in the previous sections gets clouded looking deeper into the pinch physics. The pinch plasma exhibits quite a number of phenomena like inhomogeneities, macroscopic distortion and instabilities, microinstabilities and disruptions, particle acceleration mechanisms, bursts of particle emission and electromagnetic radiation (line and continuum) from the visible light to the soft and hard X-ray region. For example, the notorious m=0 instability (necking instability) typically appears in low energy density discharges on a time scale given by the ratio of the pinch radius r and the Alfven velocity $v_A=B\cdot(\mu_0\cdot m_i\cdot n)^{-1/2}$ (with B the magnetic induction and m_i the ion mass)

$$\tau/s \cong (10^7 m_i N \frac{A\cdot m}{V\cdot s})^{1/2}\left(\frac{r}{I}\right) \qquad \textbf{Eq 1-4}$$

so that a small pinch carrying high current should break up on a ns time scale. However, discharges in light gases (e.g. Neon) and/or high energy density result in stable and homogeneous pinch columns called the stable column mode (SCM) whereas discharges in heavy gases (e.g. Argon) preferentially show pinch neckings and subsequent short-lived micropinches (hot spots) called the micropinch mode (MPM) with extraordinary high densities (up to 10^{28} m^{-3}) and temperatures (up to 2keV).

Since all these phenomena and especially the occurrence of the MPM or the SCM in pinch experiments depend on discharge parameters and on initial conditions it makes no sense to speak of typical pinch phenomena. The similarity of pinches stated in the past reflects the similarity of parameter ranges and initial conditions of conventional pinch experiments.

1.5 Pinch diagnostics

Global parameters like discharge voltage, current, velocity and shape of the current sheath, structure, overall dimensions and lifetime of the pinch change on time scales of tens of nanoseconds so that the requirements for temporal (and spatial) resolution of the diagnostic tools are not too high. However, many pinch phenomena (e.g. micropinches) occur on sub-ns time scale and sub-mm dimensions, so that high temporal and spatial resolution is inevitable.

Voltage and current signals are measured using fast (sub-ns) capacitive dividers and probes and correlated with ns accuracy, pictures in the VUV and SXR range are taken using microchannelplate cameras (MCP) with ns and sub-mm resolution.

The specific diagnostics used in this work and their parameters will be briefly discussed in corresponding chapters.

1.6 Micropinches and columns in PF with heavy gas doping

Admixtures of heavy elements in high power discharges were primarily used for diagnostic purposes. Nevertheless, it was shown later that heavy impurities added to the filling gas (usually hydrogen or deuterium) may result in essential changes of compression dynamics and may be of crucial importance in attaining high temperatures and densities of plasmas and for increasing of $n_e \times \tau$ parameter [Vikhrev 1978].

In a hydrogen plasma column in Bennett equilibrium the energy loss by Bremsstrahlung (BR) balances Joule heating with Spitzer conductivity at the Pease-Braginskii current $I_{PB} \approx 1.6$ MA [Pease 1957; Braginskii 1961]. For hydrogen plasmas I_{PB} hardly depends on plasma temperature. Bremsstrahlung of heavy ions with a charge $Z_{eff} >> 1$ (proportional to Z_{eff}^2) is significantly higher than BR of a hydrogen plasma. Moreover, the power of line radiation of heavy ions can exceed BR by orders of magnitude. As a result a corresponding value of Pease-Braginskii current for the plasma doped with heavy impurities is essentially lower than for hydrogen or deuterium plasmas.

An estimate of a critical (Pease-Braginskii) current of hydrogen plasma doped with impurity with a nuclear charge Z_N was given in [Khautiev et al 1989]. A value of a critical current for such a plasma essentially depends on electron plasma temperature (T_e) and effective charge of ions

$$I_{CR}[MA] \approx 2 \times 10^{-2} \times \frac{Z_{eff}}{Z_n^{\,2}} \times T_e^{\,0.75} \times \frac{(2 + \eta \times Z_{eff})}{(1 + \eta \times Z_{eff})}, \qquad \textbf{Eq. 1-1}$$

where $\boldsymbol{\eta}$ is the amount of heavy impurity, T_e is the electron temperature and Z_{eff} the mean charge of heavy ions present in the plasma at this temperature. For a deuterium plasma containing 2% of Xe at $T_e \approx 1$ keV and $Z_{EFF} \approx 40$ a critical current $I_{CR} \approx 0.1 - 0.2$ MA, which is nearly an order of magnitude lower than the values for a pure deuterium plasma. This estimate was a strong indication that the so-called "hot spots" or micropinches, resulting from

m=0 instabilities in presence of strong radiative losses, are mainly due to line radiation of Xe ions.

"Hot spots" were first discovered in low inductive vacuum sparks – discharges in metallic vapors (Fe, Cu) with a current of about 0.1 MA [Cohen et al 1968]. The history of "micropinches" is found in two review papers [Korop et al 1979; Koshelev et al 1991]. Very high electron temperatures (up to a few keV) and densities (above 10^{29} m^{-3}) have been measured in micropinches at comparatively low discharge currents. The physics of micropinches was well understood when the so-called "Simple model of plasma focus" [Vikhrev 1977] had been modified for strongly radiating plasmas with high effective ion charge [Vikhrev et al 1982].

1.6.1 Experimental studies of micropinch appearance in PF discharges.

The first evidence of a possible influence of heavy impurities on dynamics of plasma compression in PF discharges was reported in [Filippov 1983]. The appearance of "hot spots" - micropinches of about 10 μm in size at the "second compression" phase was attributed to evaporation of copper from the electrodes during the "first compression" of the plasma focus. Similar phenomena are seen also earlier in plasma focus experiments in a mixture of deuterium and heavy noble gases [Peacock et al 1969].

A short survey of experimental studies of plasma focus dynamics with heavy impurities in the fill gas, which have been made for the last decade in different groups, is given below.

Sukhumi Physical-Technical Institute.

A systematic study of PF plasmas doped with heavy gas impurities have started in 1988 in Sukhumi Physical-Technical Institute using two Mather-type PF: "KPF-3" with a stored energy W ≈ 100 – 150 kJ and discharge current I ≈ 1.5 MA and "KPF-1M" (40 kJ, 20 kV) [Koshelev et al 1988; Antsiferov et al 1990; Antsiferov et al 1991].

In experiments on "KPF-3" heavy gas was added to deuterium prior to the discharge (pre-filled mode). A necessity to keep the dynamics of the "run-down" phase and compression unaltered restricted the amount of added heavy noble gas in the experiment on "KPF-3" to a few percent.

Soft X-rays (SXR) have been recorded by means of a two-channel pinhole camera which was directed normal to the system axis. Al filters of 9 μm and 18μm were used. For

pure deuterium discharges, there is a zone of plasma of considerable size (5 – 6 mm in diameter and ~ 20 mm in length) radiating in the SXR. It has a slight inhomogeneity and diffuse boundaries. Adding a small percentage of Ar leads to a substantial growth in luminosity intensity over the SXR range. The pinch size is reduced and its boundaries become sharper. At the same time, local "spot-like" inhomogeneities appear, in some cases at considerable distances from the main pinch. MPs sizes vary from 50 to 300 μm.

In "pre-filled" type experiments by adding Xe, the background luminosity disappears, and the pinch breaks up into a series of "spots" (up to 10 and even more), which are mainly concentrated along the system axis. The MP sizes have been measured by the so-called penumbra method. The MPs were 10 to 100 μm in diameter. In axial direction the visible MP size is usually 3 – 5 time bigger, which may be also a result of axial movement. The optimum regime, in terms of number of spots, its small size and their brightness, is attained at 1 to 2 % of Xe admixture.

A significant rise in Ar concentration was realized in different experiments using the installation "KPF-1M". The vacuum chamber in these experiments was pre-filled with deuterium (3 – 5 torr) and Ar was supplied in pulses through the axial channel of the inner electrode, directly into PF formation zone. The concentration of impurities was varied by a time delay between the opening of the electromagnetic valve and the moment of discharge ignition. At increased concentration of Ar (compared with "pre-filled" mode) the sizes of some MPs turned out to be smaller than the spatial resolution of the tools used.

An "effective" photon energy in Xe "pre-filled" experiments was estimated by the filter method and appears to be approximately the same for all MPs, regardless of their brightness, and was in the range between 4 and 5 keV. Spectroscopic studies in this region were carried out using a Johann-type quartz crystal spectrograph, which have shown the presence of resonance lines of Ne-like ions Xe^{+44} and corresponding satellite transitions of Xe^{+45}. That allowed to estimate an electron temperature in MPs of 0.7 – 1 keV. An attempt to estimate an electron density has been made using two assumptions: full current flowing through MPs and Bennett equilibrium. For micropinches with a size of about 10 μm it was in the range of 6×10^{23} cm^{-3}.

In other series of experiments on installation "KPF-3" was pre-filled either with pure argon (1 torr) or mixture of argon (1 torr) and Xe (0.25 torr) [Antsiferov et al 1990]. The initial pressure has been chosen to synchronize the "run-down" phase with electrical circuit parameters. In the pure argon case pinhole imaging revealed the appearance of plasma columns with a diameter of about 0.5 mm and length up to 10 mm. Doping of argon with 25% of Xenon brought about micropinches with radial dimensions of about 50 μm.

For both regimes high-resolution spectral diagnostics was applied. Spectra registered in a region of Ly_α transition of H-like ion Ar XVIII and dielectronic satellites to this line give 0.37 – 0.38 nm. The effect of redistribution of intensities inside the group of dielectronic satellites was used. Only an upper limit of electron density ($n_e < 2\times10^{28}$ m^{-3}) was reported for pure argon discharges. Most probably this value is by far higher than the real electron density. Even assuming rather low electron temperature ($T_e \approx 300$ eV) and also that at least half of the full current flows through the pinch, the Bennett equilibrium yields $n_e < 3\times10^{27}$ m^{-3}.

For the Ar + Xe mixture the electron density in 50 μm micropinches was spectroscopically determined to be 6×10^{28} m^{-3}. These measurements enabled the authors to estimate the fraction of the full current flowing through the pinch to be only 25 to 40 %.

Düsseldorf University.

The appearance of micropinches in the focus region of the fast plasma focus SPEED2 was studied in an experimental scheme with an axial injection of heavy gases into deuterium. Detailed diagnostics of compression dynamics and micropinch plasma parameters has been applied. The SPEED2 installation is described elsewhere [Decker et al 1986].

The design of the installation SPEED2 does not allow using a premixed heavy gas (argon) -deuterium filling. Therefore, the argon is injected through the central hole in the anode with the aid of a fast valve. As a result of this injection, several MPs (usually about 10) were observed aligned along the discharge axis [Bayley et al 1991; Decker et al 1996]. First micropinches appear near the anode several nanoseconds after the “maximum compression” and subsequently at increasing distance from the anode, forming a straight chain of successive flashes within 30 ns. A typical cross section of micropinches was measured using time integrated pinhole camera imaging and was found to be about 40 μm in diameter for brightly radiating structures.

Registration of X-ray spectra showed that temperatures of the micropinch plasma are rather high – a resonance line of He-like ion Ar XVII was detected in the spectral region close to 0.4 nm together with an intercombination line and satellite transitions in Li-like Ar XVI. An X-ray KENTECH streak camera was applied for temporal resolution of He-like spectra and it was found that MPs last 250 ps only. This lifetime was significantly shorter than any previous estimates and was in good agreement with predictions of a radiative-collapse model for the development of m=0 instabilities [Vikhrev et al 1982, Koshelev & Pereira 1991].

Time resolved spectra registered with the help of a streak camera were unfortunately saturated and could not be used for the evaluation of plasma parameters (e.g. electron density and temperature). This was done later in a joint work of ISAN (Troitsk), Bochum University

and SPEED2 groups [Koshelev et al 1994]. Time integrated resonance spectra of H-, and He-like ions of argon have been recorded with high spectral resolution. Spectra were analyzed taking into account effects of optical thickness, plasma motion (compression or expansion) and ionization transitivity. Very subtle but reproducible and reliable differences in line profiles of the resonance line (with a high optical thickness) and a resonance line (optically thin) yield parameters as plasma density ($\approx 10^{23}$ cm^{-3}) and compression velocity ($\approx 10^5$ m/s). The value of plasma density was confirmed by analysis of satellite transition relative intensities. Electron temperatures were estimated as 1 – 1.5 keV.

Dynamics of the plasma compression was studied using time-framed pinhole imaging of the plasma column in VUV radiation [Decker et al 1996]. The four frame camera based on open microchannel plate (MCP) camera has a negligible quantum efficiency for radiation wavelengths longer than 200 nm and below 0.2 nm, thus neither visible nor UV radiation and hard X-rays are detected. (Principles of working of MCP camera and results of the camera calibration will be discussed in more detail in Chapter 4). The results can be briefly described as follows:

1) 10 ns prior to stagnation (t=0) unperturbed plasma columns are seen on MCP camera frames. Shortly after t=0 one can detect the development of m=0 instabilities, first near the anode and later at higher Z positions while the bottom structures already decay. The later structures seem to be weaker and vanish about 70 – 100 ns after stagnation.

2) A comparison of unfiltered with filtered images using different filters (1.5 μm makrofol, 6 μm makrofol and 10 μm of beryllium) shows that micropinches appear exactly where the plasma column is necked. It was concluded that necking is a necessary condition for the micropinches to be actuated, but not sufficient for them to occur.

Stuttgart University.

Spectroscopic methods have also been used for studying micropinch actuation in an installation DPF-78 – a Mather type plasma focus in Stuttgart University with a stored energy 28 kJ [Antsiferov et al 1995]. Pinhole images obtained with various gas admixtures were classified into three main types: a) a long cylindrical pinch, b) relatively small pinches immersed into large-structure clouds and c) micropinches. The observation was related to the existence of transition between column and micropinch modes of compression and also to the appearance of "microcolumns" – micropinches with anomalous high aspect ratio (ratio of length and diameter of radiating plasma) exceeding 10.

1.6.2 Observation of transition between column and micropinch mode.

The very first experiments showed that depending on atomic number of the impurity Z_N (different noble gases were taken: Ne, Ar, Kr, Xe or nitrogen) and its amount compression resulted either in columns or micropinches radiating in VUV and X-ray spectral regions. The general trend was: columns are typical for low atomic number Z_N of the impurity or/and its low concentration. Plasma columns were also reported for KPF-1 (Sukhumi) for low amounts of Ar.

Special investigations of the transition between column and micropinch were performed in a plasma focus RWTH & ILT (Aachen) group [Lebert R. et al 1995]. Results of the analysis can be summarized as follows:

The primary column in PF discharge is a result of the "run-down" phase and stagnation of the plasma on the discharge axis. The temperature of the primary column is a result of thermalization of kinetic ions. The necessary condition of the column mode is that at this temperature the plasma consists of He and H-like ions, which have rather low radiation power. This may happen when the plasma forms in a gas consisting of light elements, with a comparatively low temperature of full ionization up to K-ions or bare nuclei. Due to low radiation losses the discharge current is less than the critical current value, which is not favorable for the development of m=0 instabilities in the radiative collapse mode.

For heavier elements the electron temperature at stagnation on axis may correspond to lower stages of ionization (e.g. ions with open L or even M electron shell). This type of ions strongly radiates, which can trigger the actuation of micropinches.

The energy that ions gain during the "run-down" phase and the electron temperature of the primary column depend on the initial pressure of the filling gas. It allows to realize both regimes (micropinch and column) for the same current and filling gas by merely changing the initial pressure.

1.7 Stable column mode in SPEED2.

The column mode as a phase of pinch development have been detected at SPEED2 of doped plasma compression. Using multilayer mirrors reflecting in different wavelength region from 2.4 till 4.5 nm images were taken of the SPEED2 pinch plasma in different stages of compression [Bobashev et al 1996]. Experiments were done for deuterium-embedded argon pinch plasmas. For longer wavelengths (3.1 – 3.4 nm and 4.4 – 4.6 nm, corresponding

to comparatively low stages of ionization (Ar IX, Ar X and Ar XI) and low temperatures, images show a hollow cylinder with a sheath thickness of about 1-2 mm. On images taken in the spectral interval 2.5 – 2.7 nm, corresponding to radiation of Ar XII and Ar XVI, a plasma column of 1- 2 mm total diameter and some bright spots of about 0.5 mm in size are clearly seen. Registration of time-integrated pinhole X-ray images in similar discharges reveals "hot spots" with a size of tens of micrometers.

Later [Kies et al 1998] an experimental campaign was performed where regimes with injection of three gases (neon, tetramethylsilane (TMS) - SiC_4H_{12}, and argon) were compared. As it was expected, using light gases (neon) led to stable plasma columns. Plasma compression dynamics was observed using time gated pinhole imaging with MCP camera. Injection of TMS containing comparatively heavy element Si (Z_N=14) exhibits both modes, namely a stable column and a transition to micropinch-like structures. Argon demonstrates multiple pinch neckings from which micropinches can be actuated if the density in the neck is high enough and ions are not fully stripped so that intensive line radiation favors these local radiative collapses.

During the run-down phase and dynamic compression the temperature of the sheath T_S is proportional to the ratio of the magnetic pressure $\boldsymbol{B^2/2\mu_0}$ to the filling pressure $\boldsymbol{p}$, so that $\boldsymbol{T_S \sim I^2/(r^2 p)}$, where $\boldsymbol{I}$ is the sheath current and $\boldsymbol{r}$ the sheath radius. So high an ionization degree is favored by low filling pressures and especially by small anode radii for a given current [Deutsch et al 1986]. The temperature of the final pinch plasma depends on both, the number of particles per unit length ($N_i + N_e$) and the pinch current squared (Bennett relation). The column mode thus not only can be favored by light gases, but also by low sheath density $\boldsymbol{n}$, small accelerator dimensions and high pinch currents.

Different diagnostics have been used. They included measuring of electrotechnical characteristics, an extended X-ray diagnostic and monitoring of neutron pulses. X-ray diagnostics consisted of an X-ray streak camera with about 100 ps resolution, a compact spectrometer for the spectral range of 0.9 – 1.5 nm with a spectral resolution of 10^4, and a multilayer mirror (MLM) optics for the spectral range 0.5-1.5nm.

In contrast to other experiments SPEED2 exhibits a well defined stable plasma column (SCM) with extraordinary homogeneity and reproducibility at high plasma energy density.

1.8 Subject of the present work.

In this work further investigation of the stable column mode on SPEED2 plasma focus is described. Emphasis is put on experiments with a new electrode geometry. In previous

experiments observations of SCM were made using an anode with a diameter 108mm. It was found interesting to investigate whether this operation mode can be established at smaller pinch currents and smaller electrode dimensions, but the same energy density of the sheath and the pinch. Lower energy input was achieved by reducing the number of Marx modules. An anode with smaller diameter (78mm) was installed.

The pinch plasma was investigated using time-integrated and time-resolved diagnostics. Time-integrated pinhole imaging (Chapter 3) allowed detecting the final stage of the pinch development and narrow plasma columns intensively radiating in the X-ray region. Using different filtering and theoretical modeling of spectra an electron temperature of this plasma object was obtained.

Pinch compression dynamics was studied using time-resolved pinhole imaging simultaneously with time-resolved X-ray spectroscopy methods (Chapters 4 and 5). Synchronizing both diagnostics in time, evolution of pinch geometry and plasma parameters during the compression phase could be analyzed. Spectroscopic methods of determining plasma parameters using intensity ratios of resonance transitions of He- and H-like ions and dielectronic satellites (Chapter 2) were used to obtain reliable data of plasma temperature and density (Chapter 5).

2. Spectroscopic X-ray diagnostics

2.1 Introduction

Plasma spectroscopy plays a crucial role in characterizing the SPEED2 plasma focus. A short review of spectroscopic diagnostics is presented in this section. Plasma spectroscopy is a very wide field and therefore we have restricted ourselves to descriptions of methods, which have been used in this work. For example we do not discuss the whole family of diagnostic tools connected with the study of ion line profiles. Due to insufficient spectral resolution we have concentrated mainly on methods based on comparison of line intensities.

2.2 Models for describing the state populations in plasmas.

The emission rate of a spectral line from a plasma is proportional to the number of atoms in the upper state of the radiative transition per unit volume. Level populations are derived from population distributions, which are linked with the cross sections of elementary processes.

Interpretation of the radiation emitted by plasmas needs the knowledge of both the charge-state distribution and excited level populations of the different ions. In principle, this requires the solution of a complex system of rate equations, describing the population and de-population of levels by ionization, recombination, collisional excitation and de-excitation, radiative decay and absorption, and also stimulated emission. A given degree of ionization is connected with two neighboring ionization degrees by ionization and recombination processes. In general, one has to solve a time-dependent system of equations. It is, however, often sufficient to consider the steady-state problem. Evaluation of the charge-state distributions is obtained by means of the fractional abundances

$$f_Z(N_e, T_e) = N_Z \Big/ \sum_z N_z \qquad \textbf{Eq 2-1}$$

where N_Z is the abundance of ions of charge Z in the ground and all excited states.

Generally, one uses one of the following three approximations: the corona model (CM), the collisional-radiative model (CR), and the local-thermodynamic-equilibrium model (LTE). Which model must be used depends on several parameters, but mainly on the electron density. For low electron densities the CR model reduces to the CM, while for high electron densities it transforms into LTE.

In the general case, the level populations differ from those in LTE or in CM. However, the distribution of energies of free electrons is, as a rule, Maxwellian or almost Maxwellian. General features of the transition from LTE at high density to other distributions at intermediate and low densities can be demonstrated using the simplest 2-level model. Such elementary processes as collisional excitation $l \rightarrow u$ and de-excitation $u \rightarrow l$, the radiative decay of the upper level u to the lower level l, radiative decay of level u to other levels are considered.

The balance equation then has the form

$$N_l N_e < v\sigma_{lu} >= N_u N_e < v\sigma_{ul} > + N_u A_u \,, \qquad \textbf{Eq 2-2}$$

where A_u is a total probability of radiative decay from level u, and $<v\sigma_{ij}>$ the rates for collisional excitations (de-excitations). Finally we have

$$\frac{N_u}{N_l} = \frac{g_u}{g_l} \frac{\exp(-\frac{\Delta E_{ul}}{kT_e})}{1+R}; where: R = \frac{A_u}{N_e \cdot < v\sigma_{ul} >}. \qquad \textbf{Eq 2-3}$$

The factor R describes the deviation from the thermodynamical limit. R<<1 corresponds to LTE conditions and Boltzmann population distribution. At R ≥ 1 the population distribution is not longer Boltzmann-like and usually the population of excited levels is lower than at LTE. Nevertheless as de-excitation rates $<v\sigma_{ul}>$ do not strongly depend on T_e, the main temperature dependence of populations is still given by the Boltzmann exponential factor.

Similar considerations for cases when the level u is the ionization limit (ground level of the next ionization state) can be done for the ionization equilibrium. In this case, one has to consider three recombination processes: three-body, radiative and dielectronic:

$$\frac{N^{(z+1)}}{N^{(z)}} = \frac{g_{z+1}}{g_z} S \frac{\exp(-E_z / kT)}{1+R_z}, R_z = \frac{\kappa_v + \kappa_d}{N_e \kappa_r}, \qquad \textbf{Eq 2-4}$$

where κ_r, κ_v and κ_d are the rate coefficients of three-body, radiative and dielectronic recombination.

In the limit $N_e \rightarrow 0$ (for the low-density limit) we obtain the **coronal** distribution for population of excited atomic (ionic) levels, which is usually expressed using the population of the ground level:

$$N_j = N_{gr} \cdot N_e \cdot \frac{< v\sigma_{gr,j} >}{A_j}. \qquad \textbf{Eq 2-5}$$

The population densities are determined by a balance between the rate of collisional excitation from the ground level and the rate of spontaneous radiative decay.

The equation for ionisation equilibrium in the coronal limit is

$$\frac{N^{(z+1)}}{N^{(z)}} = \frac{< v\sigma_i >}{\kappa_v + \kappa_d}. \qquad \textbf{Eq 2-6}$$

In this approximation there is a balance between collisional ionization (and excitation) and recombination (and spontaneous decay).

This model requires low electron densities. The collisional depopulation rate of excited states should be much lower than that of the radiative depopulation:

$$N_e << \frac{\sum_{j<k} A_{kj}}{< v\sigma_{kj} >}. \qquad \textbf{Eq 2-7}$$

When considering converging Rydberg states with high principal quantum numbers **n** there is always a value of $\boldsymbol{n_{TH}}$, above which Eq 2-7 cannot be satisfied: with increasing principal quantum number, the probability of spontaneous radiative decay decreases, while that of collisional depopulation rate increases. So, a range of levels with larger than $\boldsymbol{n_{TH}}$ principal quantum numbers forms a so-called "thermal zone" which is in equilibrium with the next ionization stage. The thermal zone effectively increases the ionization rate of ions.

An estimate of an electron density below which the CM for ionization equilibrium is applicable is usually taken as $\boldsymbol{n_{TH}} = 6$ [McWhirter 1965]. Using an approximation for collisional rates for H-like (see below) one can show that CM requires

$$N_e < 5.9 \cdot 10^{10} Z^6 T_e^{1/2} \exp\left(\frac{0.1 \cdot Z^2}{T_e}\right), \qquad \textbf{Eq 2-8}$$

where N is given in cm^{-3}, and T_e in eV. The results of calculations of the charge-state distribution in the CM are usually presented as plots of the fractional abundances f_Z as a function of the electron temperature T_e. Sometimes the electron density dependence, when dielectronic recombination is accounted for, is also shown.

2.3 Opacity effects in plasmas

Radiation trapping is an important phenomenon affecting the level populations of gases or plasmas. Below we will discuss mainly resonance processes, i.e. bound-bound transitions. On reabsorption of a spontaneously-emitted photon, an ion (atom) initially in the lower quantum state of a transition is put into the upper state, thus reducing the apparent decay rate of this level.

A cross-section of the absorption at a given frequency inside the line profile is

$$\sigma_{\omega}^{ab} = \frac{1}{4}\lambda^2 \frac{g_{up}}{g_l} a_{\omega} , \qquad \textbf{Eq 2-9}$$

where a_{ω} is the spectral Einstein coefficient for spontaneous emission, λ the wavelength and g the statistic weights of upper and lower levels.

Taking stimulated emission into account an absorption coefficient can be presented in the form

$$k_{\omega} = \frac{1}{4}\lambda^2 \frac{g_{up}}{g_l} a_{\omega} N_l \left[1 - \frac{g_l N_{up}}{g_{up} N_l} \right], \qquad \textbf{Eq 2-10}$$

where N_{up} , N_l are populations of corresponding levels in the plasma.

The plasma is considered to be optically thin for a given transition when the optical density $\tau_0=(k_0 \cdot l)<1$.

High optical thickness may essentially change populations of atomic (ionic) levels. Generally equations of radiation transfer, coupled with a set of equations describing level population dynamics, have to be solved. The equation of radiation transfer is

$$dL_{\omega}(x) = [\varepsilon_{\omega}(x) - k_{\omega}(x) L_{\omega}(x)] dx , \qquad \textbf{Eq 2-11}$$

where $L_{\omega}(x)$ is the spectral radiance in $W/(m^2 \cdot Sr \cdot Hz)$, and $k_{\omega}(x)$ is the local absorption coefficient.

The solution for a line intensity profile in an optically dense homogenous plasma (when S_{ω} is uniform) can be written as:

$$L_{\omega} = S_{\omega} \times (1 - e^{-k_{\omega} l}) , \qquad \textbf{Eq 2-12}$$

where S_ω is a so called "source function", which is determined by the relative population of the two stages of the transition. When introducing an "excitation temperature" for the relative populations of upper and lower levels we have

$$kT_{EX} = h\upsilon \Big/ \ln(N_l g_{up} / N_{up} g_l), \qquad \textbf{Eq 2-13}$$

where $h \cdot \upsilon$ is the transition energy, a "source function" can be expressed as a Planckian intensity of a black body with a temperature equal to kT_{EX}.

Quite a number of rigorous and rather complicated methods are used to calculate the population densities within the plasma. A widely employed approximate approach was introduced by Holstein [Holstein 1947, 1951]. He described the effects of radiative transport by introducing an **escape factor Θ**, which enters the calculations such that it reduces effectively a spontaneous emission probability

$$A_{eff} \approx \Theta \times A_{ul}, \qquad \textbf{Eq 2-14}$$

where A_{ul} is the spontaneous emission rate from the upper to the lower level.

Most generally the escape factor was defined as the mean probability that a photon emitted anywhere in the source travels directly to the surface of the source in any direction and escapes [Walsh 1957], [Abramov & Kogan 1967]. The escape factor concept has been reviewed and analyzed thoroughly by Irons [Irons 1979, 1979a, 1979b].

Analytical expressions mostly for the asymptotic forms of the escape factor are known for comparatively simple source geometries (infinite cylinder or plane-parallel slab) and also only for some spectral line shapes (Gaussian, Lorentzian, Holtsmarkian). An elegant and simple way to derive an expression for the escape factor was given in [Fill 1988].

Radiative transfer can be strongly affected by relative motion of different parts of a source. One of the examples would be an expanding cloud of a laser produced plasma or compressing/expanding cylindrical plasma of a Z-pinch. Due to Doppler effect an absorption profile of expanding/compressing edge of the plasma will be shifted (red/blue) with respect to an emission profile for a not moving plasma cylinder. This effect may significantly decrease absorption effects and increase the escape factor value. Some analytical approximations are possible for the so-called Sobolev's limit when the Doppler shift on the free path length is bigger than the line profile width [Rybicki 1984, Irons 1990]. Monte-Carlo calculations for different line profiles and plasma edge expansion/compression velocities for infinitely thin plasma disc were performed by Schulz [Schulz 1992].

According to the Eq 2-12 the line shape in the optically thick plasma could be significantly distorted. On the other hand, the total line intensity is not necessarily always

affected by optical thickness effects. An influence of optical thickness on total line intensities can be described by a special introducing of a so-called ***"Yield factor"*** – ***Y*** [Schulz 1992]. In case of a simplified model of a "two level" ion in a plasma and provided that excitation of a corresponding spectral line is due to collisions with electrons, the factor Y for a given spectral line represents a ratio of the number of photons radiated by a real source (N_{real}) to a number of excitation of the upper level. For the optically thin plasma ($\boldsymbol{\Theta} = 1$) this ratio is given by

$$Y = \frac{A_{ul}}{A_{ul} + N_e < v\sigma_{ul} >} = \frac{1}{1+\gamma}, \qquad \textbf{Eq 2-15}$$

where $\boldsymbol{\gamma = 1/R = N_e<v\sigma>/A_{ul}}$ is a reverse value ***R*** from (Eq 2-3) and describes deviations from LTE. A value of $\gamma << 1$ corresponds to coronal conditions, where all excitations result in photon emission (Y=1).

As it was shown [Schulz 1992] that for the optically thick plasma ($\boldsymbol{\Theta} < 1$) a generalized form of Eq 2-15 is

$$Y = \frac{A_{ul} \cdot \Theta}{A_{ul} \cdot \Theta + N_e < v\sigma_{ul} >} = \frac{1}{1+\gamma/\Theta}. \qquad \textbf{Eq 2-16}$$

For essentially coronal plasmas ($\boldsymbol{\gamma << 1}$) the yield factor Y ≈ 1 even when the escape factor is far from unity. In many cases pinch plasmas are expected to be coronal. Eq 2-16 shows that many of intensity ratios calculated for optically thin plasmas could still be used for diagnostics of optically thick ones.

2.4 Plasma diagnostic methods of hot plasmas from the spectra of H- and He-like ions.

Several spectral diagnostic methods, implementing K-spectra of dense and hot plasmas are presently known. Methods for determining the plasma temperature from relative intensities of resonance transitions of ions of a different ionization stage are widely used. Plasma temperatures can also be determined from line intensities of 1s-np, $1s^2$-1snp ($n \geq 2$) series. Since the spectral coverage of the X-ray spectrograph and its resolution are complementary parameters, the required spectral range can be wider than available from experimental set-ups and required resolutions.

The method of electron temperature evaluation from the intensity ratio of the resonance line to its satellites is discussed by Gabriel [Gabriel 1972]. Satellites appear close to its

"parent" line, and therefore no difficulties with spectrograph coverage are expected. In the X-ray region satellites to the resonance lines of H- and He-like ions are often used for determining the electron temperature. Using some satellites to the resonance lines of He- and H-like ion also the electron density and ionization balance can be estimated.

2.6.1 Determination of electron temperatures. Plasma diagnostics with satellites to resonance line of He- and H-like ions.

The method of T_e determination from satellite spectra was proposed by Gabriel and Jordan [Gabriel et al 1972]. It is based on the fact that one of the satellite excitation channels (for some satellites the only one) is dielectronic recombination, the process reverse to autoionization. Dielectronic recombination can occur, when an atom captures an electron on one of the autoionizing levels, and so the atom ends with two or more excited electrons in its shell.

Relaxation can have two different channels: autoionization (electron is released from the autoionizing level), radiative decay (stabilization of the metastable ion by radiative transition). For satellites of He-like ions these processes are:

$$(1s^2)_{He} + e \xrightarrow{K_d} (1s2\,1'\mathrm{n}\,l)_{Li} \xrightarrow{A_s} (1s^2 nl)_{Li} + \hbar\omega_s$$

or

$$(1s^2)_{He} + e \xrightarrow{K_d} (1s2\,1'\mathrm{n}\,l)_{Li} \xrightarrow{\Gamma} (1sn'l')_{He} + e'.$$

The intensity of the satellite with frequency ω_s, excited by the dielectronic recombination is

$$I_s^d = N_{He} N_e K_d \frac{A_s}{\Gamma + \sum A_s}, \qquad \textbf{Eq 2-17}$$

where K_d is the rate of the dielectronic capture on the $1s2l'nl$ level of Li-like ion, A_s and ΣA_s are the probability of radiative decay by one channel and the total radiative decay probability of $1s2l'nl$. Γ is the probability of autoionization.

From the principle of detailed balance one can get a relationship between the rate of dielectronic capture and the probability of autoionization. Then the satellite intensity writes

$$I_s^d = N_{He} N_e 4\pi^{3/2} a_0^3 \frac{g_s}{g_0} \left(\frac{Ry}{kT}\right)^{3/2} \frac{\Gamma A_s}{\Gamma + \sum A_s} \exp\left(\frac{-E_s}{kT}\right), \qquad \textbf{Eq 2-18}$$

where g_s and g_0 are statistical weights of $1s2l'nl$ and $1s^2$ levels, E_s their energy difference, Ry=13.6eV, a_0 the classical atomic radius.

The resonance line ("W") is excited by electron collision with an ion through

$$\left(1s^2\right)_{He} + e \rightarrow (1s2p[^1P_1])_{He} + e'$$

Its intensity is thus given by the expression

$$I_W = N_{He} N_e < v\sigma >_{ex} \frac{A_W}{A_W + < v\sigma >_{de-ex}}, \qquad \textbf{Eq 2-19}$$

where $<v\sigma>_{ex}$, $<v\sigma>_{de\text{-}ex}$ are the rates of collisional excitation and deexcitation of the W state, A_W is the spontaneous radiative decay rate.

Resonance transition in laboratory plasmas has a high probability of radiative decay, so one can simply put the branching ratio equal to unity and write

$$I_W = N_{He} N_e < v\sigma >_{ex} .$$

Finally, the temperature dependence of satellite to resonance line ratio is

$$i_d = \frac{I_s^d}{I_W} = R \frac{g_s \Gamma A_s}{\Gamma + \sum A_s} \frac{1}{T} \exp\left(-\frac{\Delta E}{kT}\right), \qquad \textbf{Eq 2-20}$$

where R is a constant and $\Delta E = E_W - E_s$, E_W – resonance level energy.

From Eq 2-20 we can conclude that

a) the i_d ratio is a function of the temperature only, and can be used for its determination,
b) the ratio is not dependent on the population density, and therefore it can be used also in non-stationary plasmas.

Satellite transitions can be also collisionally excited from the $1s^22l$ of Li-like ions

$$(1s^2 2l)_{Li} + e \rightarrow (1s2l2l')_{Li} + e'$$

It was theoretically shown, that for some satellites collisional excitation is the main channel. The intensity of such a satellite line is

$$I_s^c = N_{Li} N_{Ne} C_c , \qquad \textbf{Eq 2-21}$$

where C_c is the collisional excitation rate for the upper level of satellite transition. The relative intensity ratio to the resonance line is thus

$$i_c = \frac{I_s^c}{I_W} = \frac{N_{Li}}{N_{He}} \frac{C_c}{C_W} . \qquad \textbf{Eq 2-22}$$

The ratio i_c for collisionally excited satellites depends on the relative population of the He- and Li-like ionization stages. It can therefore be used for determination of the ionization balance in a plasma. In steady state i_c is also a function of the plasma temperature. After Gabriel [Gabriel 1972], the temperature estimated from Eq 2-22 is usually cited as T_Z. In stationary equilibrium plasmas $T_Z = T_e$, but in general it is not the case. $T_e > T_Z$ means that the

plasma radiates during the process of ionization, with $T_e<T_Z$ it radiates during recombination [Bhalla 1975].

2.6.2 Methods of electron density determination.

Among methods utilizing comparisons of line intensities there is one, which is most widely used. It is based on a comparison of intensities of two lines with essentially different Einstein coefficients of spontaneous decay - allowed and forbidden transitions. This method was described in early work of Gabriel [Gabriel 1972] and later applied to different combinations of ion transitions.

Generally, a density dependence of intensity ratios of such pairs of lines can be expected from rather simple considerations. Considering two lines originated from two excited levels (possibly having close energies) with statistic weights g_R and g_M and radiating decay rates A_R and A_M ($A_R>>A_M$) – we will call them "resonance" and "metastable" levels. At high electron density populations of levels described by the Boltzman formula (see Eq 2-7 at R<<1) and neglecting the energy difference $N_R/g_R \approx N_M/g_M$. The ratio of intensities in this case is

$$R_{LTE} = \frac{N_R \cdot A_R}{N_M \cdot A_M} \approx \frac{A_R \cdot g_R}{A_M \cdot g_M} >> 1. \qquad \textbf{Eq 2-23}$$

For coronal plasmas, where one can neglect collisional depopulation of excited levels, every excitation either to the resonance or to the metastable levels results in photon emission. The ratio of intensities in coronal conditions is proportional to rates of excitation of these two levels by electron collisions from the ground level. Rates for excitation of metastable levels can be comparable with rates for resonance levels and as a result, resonance and forbidden lines may have almost equal intensities

$$R_{COR} = \frac{N_R \cdot A_R}{N_M \cdot A_M} = \frac{< v\sigma_{0R} >}{< v\sigma_{0M} >} \approx 1. \qquad \textbf{Eq 2-24}$$

Note that in coronal plasmas metastable levels are strongly overpopulated compared with resonance levels (Eq 2-3, Eq 2-5).

For both limits (LTE and corona) intensity ratios do not depend on plasma density but there must exist a transition zone with relatively strong density dependence. Physical processes involved into the transition may differ for different levels involved. Generally they are connected with the fact that radiative decay times for metastable levels are longer and at

increasing density a metastable state has increasing chances to be depopulated by increasing number of collisions. Similar collisional depopulation of resonance levels happens at much higher densities as collisions start to compete with the very efficient radiative decay.

The most widely used combination of allowed and forbidden transition is a combination of a resonance transition $1s2p\,^1P_1 \rightarrow 1s^2\,^1S_0$ ("W" line) and intercombination transition $1s2p\,^3P_1 \rightarrow 1s^2\,^1S_0$ ("Y" line). In this work a ratio of "W" and "Y" lines in He-like ion Ne IX was used for determination of electron densities and will be described in Chapter 4 together with a more detailed picture of all physical processes involved and calculated values.

3 Time-integrated pinhole x-ray diagnostics

3.1 Introduction

Experiments on characterization of the stable column mode (SCM) at the SPEED2 plasma focus were carried out so far with two different anode geometries. We call the "big anode geometry" the set-up with anode diameter 108mm (stored energy 57-67kJ). In the "small" anode set-up, the anode diameter 78mm and the stored energy 37kJ. In both experiments the capacitor bank was charged to 180kV.

The reason for the "small" anode experiments was to find out whether the SCM can be established in small experiments less powerful than SPEED2. Mainly the results of this work are connected with the "small" geometry. As it is often useful to compare data of plasma parameters obtained in both experiments, in the following sections the results will be presented concerning both geometries. Data obtained by other scientists of the plasma focus group will be also used for comparison and properly cited.

3.2 Experimental setup

The experimental set-up for recording of the time-integrated filtered pinhole images was similar for both geometries and is presented in Figure 3-1. Plasma images were recorded on the KODAK x-ray film using different filtering.

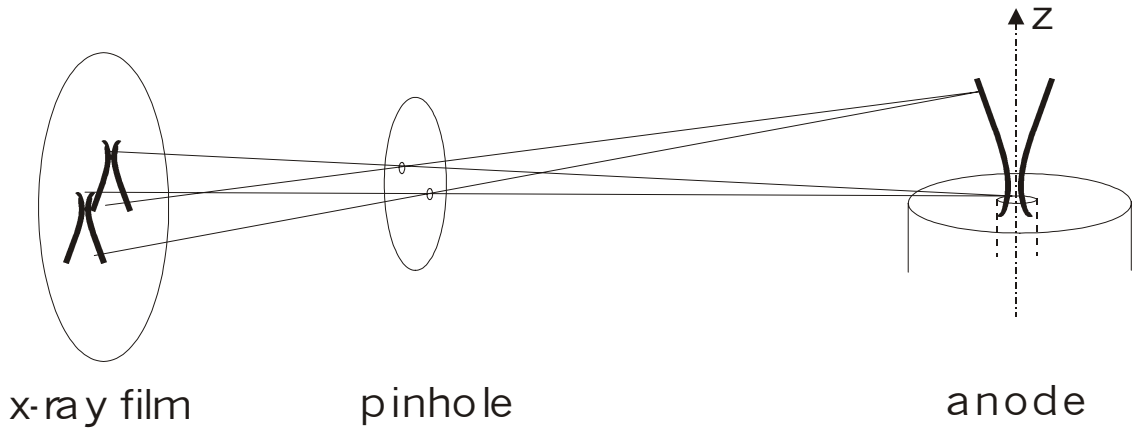

Figure 3-1. Experimental setup of time integrated pinhole diagnostics.

For the “big anode” case results of plasma imaging with neon injection were reported in [Kies et al 2000]. Images produced by radiation with wavelengths shorter than 1nm have shown that a bright plasma column with diameters ≤ 1mm and visible lengths of about 10mm are usually formed.

For neon injection a series of images was obtained in a “small anode” geometry using a double-pinhole installation. Primarily one pinhole was covered with 10µm Be foil, the other with 12µm Al. Transmissions of each filter are presented in Figure 3-2. Pinholes were made with a sharpened needle in a 1mm Cu foil. The diameter of the pinholes measured with a microscope was about 100µm.

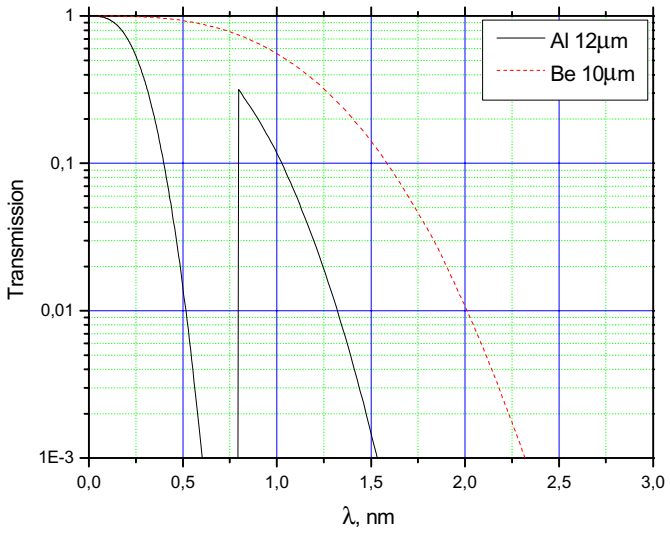

Figure 3-2. Transmission of the 10µm Be and 12µm Al filters.

There are two changeable parameters determining the composition of the plasma and thus compression regime: the time delay τ between the gas valve opening and initiation of the discharge and the primary pressure p before the fast valve. Both parameters can influence the number of particles of the injected gas above the anode (in the discharge chamber). The pressure p has a lower limit of about 3bar due to technical parameters of the fast valve. The upper pressure limit is about 6bar.

3.3 Images of the plasma column.

It was found that at delay times of neon injection τ <5ms no pinch image is produced on the x-ray film, but only a weak image of the anode surface. At such short delay times a very small amount or even nothing of the injected gas has reached the anode end (determined

by the length of gas transport pipes). This results in pure deuterium pinches producing intensive neutron pulses, but weak or no SXR. At delay times $\tau \geq 5$ms images of the plasma are clearly seen. The anode surface is quite well distinguishable in most cases. The gas valve pressure was first set to p=3.0 bar. Produced images were weak, so any quantitative analysis would be difficult. The pressure was therefore increased to p=3.5bar and the time delay to τ=6ms, which gave brighter images, but no change in geometry and structure of plasma images was noticed.

The experimental set-up allows for obtaining plasma images above the anode. In fact a part of the pinch can be hidden. This can be understood from Figure 3-3, where the anode construction is shown.

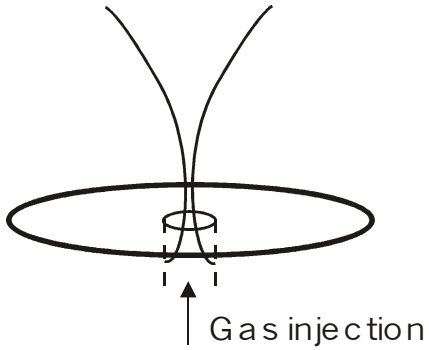

Figure 3-3 Actual view of the pinhole camera into the pinch region.

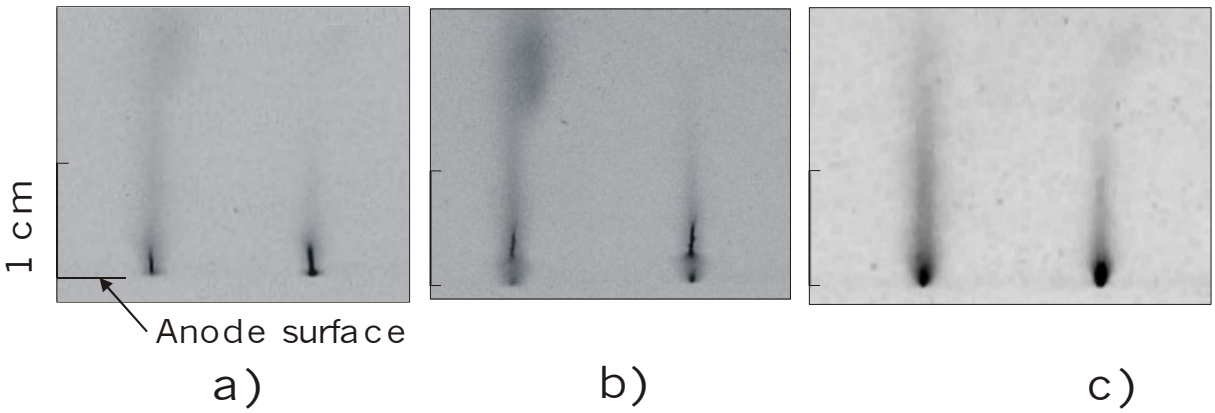

Figure 3-4. Time-integrated images of plasma columns produced in the SPEED2 PF. The left image in the frame is filtered with 12μm Al, the right one with 10μm Be.

Images of the pinch plasma are seen as column-like objects above the anode surface (Figure 3-4). Plasma columns consist of an axially symmetrical diffuse column of typically 1.4-1.8mm (FWHM) in diameter near the anode. The visible length of the diffuse column depends on filtering and injection parameters. For both filters (10μm Be; 12μm Al) the length is in the range of 1-2cm with the optical density of the image decreasing with increasing

distance from the anode. The diffuse column length behind 10µm Be filter is somewhat smaller than behind 12µm Al filter.

In many shots a thin bright narrow plasma column 2-4mm in length and about 0.3-0.5mm in diameter is seen embedded into the diffuse column (Figure 3-4a,b), which corresponds also to observations made for the "big anode" geometry. Normally, the axis of symmetry is the same for both plasma columns. But in some cases bright filaments are radially displaced or/and slanted to the side with respect to the discharge axis. The diameter of the bright column behind 12µm Al is smaller than behind 10µm Be.

Longer filaments (Figure 3-4b) are positioned a few mm away from the anode in z-direction. At the filament end, which is close to the anode an opening cone is seen on most images, which probably indicates the existence of particle beams from the compressed region.

A few shots exist where only diffuse columns are seen with a bright point on the anode surface (Figure 3-4c).

An example of scans of images of a diffuse column and of a bright narrow column are given in Figure 3-12.

Comparing the optical density of differently filtered images gives estimates of the effective wavelength of the image-producing radiation. For this estimate we assume that the radiation is monochromatic and that film optical densities are proportional to intensities of the radiation, which have passed two different filters (linear film response).

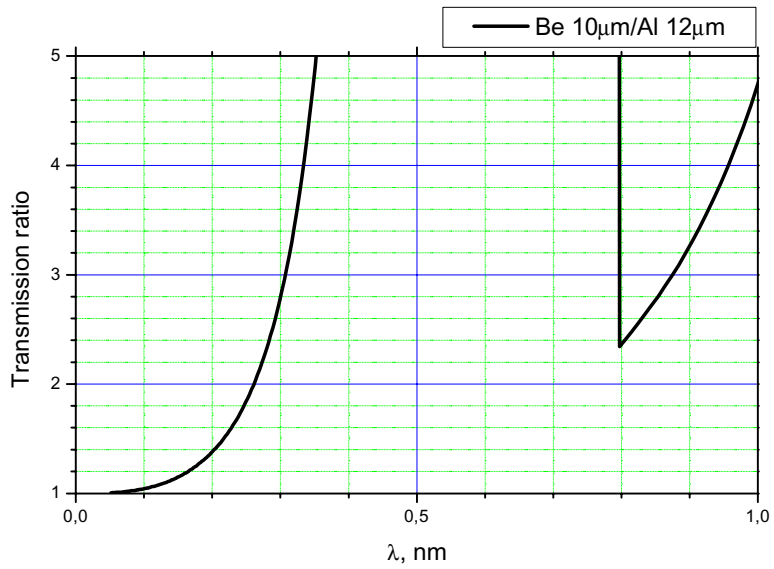

Figure 3-5. Be 10µm to Al 12µm transmission ratio.

It was found that an optical density in the center of the bright column is approximately 1.3 times higher for the 10μm Be filtered image than for the 12μm Al filtered image. A ratio of transmission of Be 10μm and Al 12μm filter foils used in the experiment is presented in Figure 3-5. A value of 1.3 corresponds to the effective radiation wavelength $\lambda_{Eff} \approx 0.2$nm.

3.4 Estimation of the plasma temperature

Rather short effective wavelengths of the radiation, which forms plasma pinhole images (ë 0.2 nm) allow us to suppose that the plasma radiates mostly due to free-free and free-bound transitions. (Shortest line radiation of H- and He-like ions is below 0.9 nm.) In this case the spectral radiation intensity may have a comparatively simple dependence on the plasma electron temperature. Further we have made an attempt to estimate the plasma temperature of the columns based on comparing of image optical densities produced by the plasma radiation behind different filters.

An information, which is needed for this estimate, concerns

i) a relevant model of plasma spectra for different electron temperatures,
ii) the transmission of the filters used in the experiment,
iii) the spectral sensitivity of the film used.

The following sources have been used for obtaining information concerning these three points (details will be given later):

i) Modeling of neon plasma spectra were made using two computer codes – "FLY", developed by R.Lee in LLNL (USA) and "NOMAD", the code developed by Yu.Ralchenko in Weizmann Institute (Israel).
ii) Transmissions of different filters for a wide spectral range are well known and can be found in different sources, for example at www-cxro.lbl.gov.
iii) Characteristics of the x-ray film used (KODAK DEF5) were systematically studied and reported [Henke et al 1986] (We assume that DEF5 film is a replica of the KODAK DEF1 film, characterized by Henke et al.) For the DEF1 film, results were reported in an energy range of 1keV-10keV. We have found that for temperature evaluation the DEF response for photon energies below 1keV is also needed. Therefore, we have applied a DEF film model, proposed by Henke, to obtain the film response in the energy range 0.5-1keV as required by our experiment.

3.5 Characterization of KODAK DEF5 X-ray film

In this section we present a simplified phenomenological model describing the film response, which have been used for calculation of DPF5 x-ray film spectral sensitivity.

A double-emulsion film has a gelatin-like protective coat of thickness t_0 (supercoat), photosensitive emulsion of thickness T, polyester base t_b, then again the emulsion and a supercoat with the same geometrical properties on the other side of the film as depicted in Figure 3-6. (Note that the supercoat is transparent to the VIS radiation. Special precautions in experiments should prevent it from reaching the film). Each layer can be characterized by its linear absorption coefficient spectral dependence.

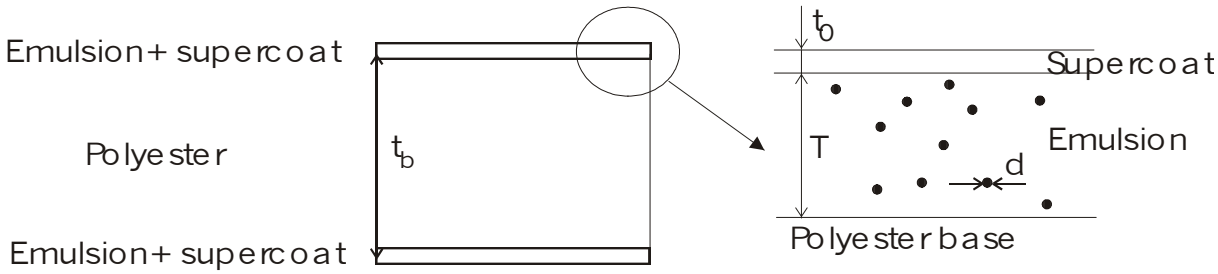

Figure 3-6. Geometrical properties of the KODAK DEF film

The radiation intensity penetrated through the supercoat is

$$I_1(\nu) = I_0(\nu)\exp(-\mu_0 t_0), \qquad \textbf{Eq 3-1}$$

where $\mu_0(\nu)$ is the linear absorption coefficient of the supercoat. Figure 3-7 shows the dependence of the supercoat linear absorption coefficient $\mu_0(\nu)$ on the photon energy.

As can be seen, the absorption in the supercoat with thickness 1μm is essential for photon energies below 1.5keV. As a result, the film sensitivity is small for low energy photons and is increasing for higher energy photons.

Part of the radiation $I_1(\nu)$, which is absorbed in the next photographic layer consisting of AgBr grains and gelatin, is

$$I_{12}(\nu) = I_1(\nu)(1-\exp(-\mu' T)), \qquad \textbf{Eq 3-2}$$

where $\mu'(\nu)$ is the linear absorption coefficient of "AgBr+gelatin" emulsion. Only the part of

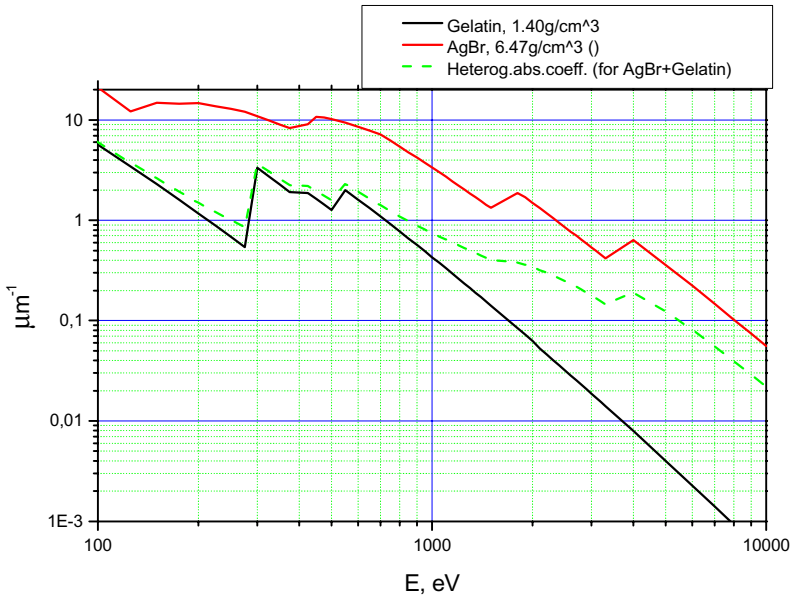

Figure 3-7 Linear absorption coefficients used in the DEF film model.

the I_{12} that is absorbed by AgBr grains(but not in the gelatin) will contribute to the film optical density. It can be described by introducing of a coefficient ç(í,I) ≤ 1 as

$$I_{12}^{'}(\nu) = I_0(\nu)\exp(-\mu_0 t_0)(1-\exp(-\mu^{/}T))\cdot\eta(\nu). \qquad \textbf{Eq 3-3}$$

With an increase of the photon energy the first photographic layer becomes more and more transparent to radiation. As a result, a sensitivity of the first photographic layer decreases, as the energy absorbed in it decreases.

Similar considerations are applicable to the second emulsion. At significantly high energies, photons not absorbed in the first three layers (supercoat, the first emulsion and polyester base), reach the second emulsion and generate an additional optical density.

$$I_{34}^{'}(\nu) = I_0(\nu)\exp(-\mu_0 t_0 - \mu^{/}T - \mu_b t_b)(1-\exp(-\mu^{/}T)\cdot\eta(\nu). \qquad \textbf{Eq 3-4}$$

Thus, the second emulsion extends the film sensitivity to higher photon energies. An increase in photon energies will make the second emulsion also transparent to the incident radiation. From this point, with the increase of photon energies the double-emulsion KODAK DEF film becomes less and less sensitive to the incident radiation.

For low intensity an optical density of the film is proportional to the energy absorbed in the photosensitive emulsion layer by AgBr grains

$$D_{12} = kI'_{12} \,. \qquad \textbf{Eq 3-5}$$

The spectral sensitivity of the film can be expressed as a number of photons needed to generate a certain constant optical density. We will designate this value as "reverse sensitivity" (RS). Finally, RS for both emulsions can be written as

$$RS^{\nu}_{12} = A \cdot \frac{1}{h\nu} \frac{\exp(\mu_0 t_0)}{(1-\exp(-\mu' T))\eta(\nu, I)},$$
$$RS^{\nu}_{34} = A \cdot \frac{1}{h\nu} \frac{\exp(\mu_0 t_0 + \mu' T + \mu_b t_b)}{(1-\exp(-\mu' T))\eta(\nu, I)}, \qquad \textbf{Eq 3-6}$$

where ***η (ν,I)*** is the factor describing which part of the absorbed radiation contributes to the optical density, ***A*** is a scale factor.

Calculation of η (ν,I) factor.

To calculate a coefficient ç a next approach can be explored. Generally an emulsion is a heterogeneous system of AgBr grains embedded in gelatin with a volume fraction of AgBr equal to V. For a highly dispersed mixture, when the AgBr-grain size is small compared with the reciprocal linear absorption coefficient of AgBr, the system can be considered homogeneous. The homogeneous absorption coefficient is given by

$$\mu' = (1-V)\mu_0 + V\mu_1 \,. \qquad \textbf{Eq 3-7}$$

The general case was studied by Henke et al [Henke et al 1984a]. The heterogeneous system is modeled as a system of ***s*** layers of thickness ***d*** equal to the effective grain size, with the grains absorbing as equivalent, aligned cubes. It is assumed that the total optical transmission of the emulsion may be given by the product of the monolayer-section transmissions. A full model for calculation of ***η (ν,I)*** factor is given in the appendix. The heterogeneous absorption coefficient may be expressed as

$$\mu' = \mu_0 - \frac{1}{d}\ln(1 - V(1-\exp(-(\mu_1 - \mu_0)d))) \,. \qquad \textbf{Eq 3-8}$$

As it was said before, we intend to extend the Henke model to low photon energies. For calculations we have used absorption coefficients μ_0 and μ_1 that were taken from the

compilation of Henke et al.[Henke et al 1984b]. The coefficient μ' was calculated with Eq 3-8 and is shown in Figure 3-7 together with absorption coefficients of emulsion materials.

Polyester transmission was obtained from the CXRO web page [CXRO]. In the spectral region of interest it was fitted by a formula $\tau = exp(-d\cdot(P1/h\nu)^{3.02})$.

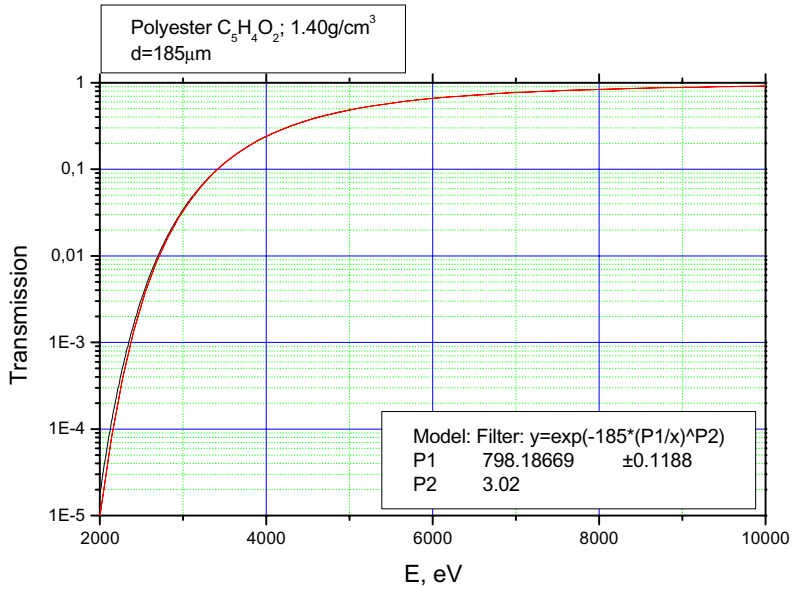

Figure 3-8 Polyester transmission.

Geometrical properties of the DEF were reported by [Henke et.al 1986]:

t_0=1.0µm (determined by a model equation fitting the low energy x-ray exposure data),

T=13µm,

d=1.6µm (from electron microscope film cross-section photos),

t_b=185µm and V=0.40

For the optical-density response of the one-emulsion coated with gelatin-like supercoat with respect to incident radiation an equation was obtained

$$\alpha D_1 = a \ln\left(\frac{1 + b\beta I}{1 + b\beta I \exp(-\mu' T / \sin\theta)}\right), \qquad \textbf{Eq 3-9}$$

where D is the optical density generated within the film, I the number of incident photons per square micrometer and $\alpha=\mu'/\sin\theta$. Fitting parameters a=0.680µm^{-1} and b=1.69µm^2.

For the second emulsion response the formula is slightly modified:

$$\alpha D_2 = a \ln\left(\frac{1 + b\beta I \exp(-(\mu_b t_b - \mu' T) / \sin\theta)}{1 + b\beta I \exp(-(\mu_b t_b - 2\mu' T) / \sin\theta)}\right), \qquad \textbf{Eq 3-10}$$

where μ_b is the linear absorption coefficient of the polyester base ($C_5H_4O_2$, ρ=1.40 g/cm^3). Finally for the double-emulsion response without saturation, we assume that

$$D(I(\nu),\nu) = (D_1 + D_2)\,. \qquad \textbf{Eq 3-11}$$

Solving this equation for I with D=const=D_0 yields a film spectral sensitivity I(ν,D_0). For some applications it is useful to have information about a contribution of each emulsion layer to the formation of optical density. By solving equations separately for the first and the second emulsions, the reverse sensitivity (RS) of each emulsion vs. photon energy was obtained. RS has the meaning of the number of photons over 1 μm^2 required to generate a density of D_0.

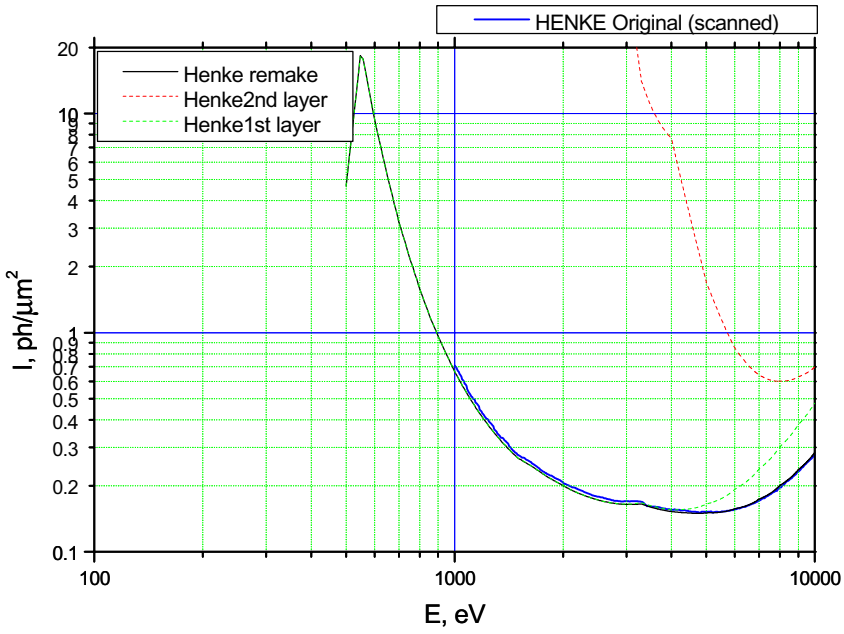

Figure 3-9 Intensity I that is required to generate a specular density $D_{0.1}$=0.5, versus photon energy E

A composite curve can also be calculated from reverse sensitivities (RSs) of each emulsion with the assumption that optical density D is proportional to number of photons as

$$\frac{1}{RS} = \frac{1}{RS_{12}} + \frac{1}{RS_{34}}, \qquad \textbf{Eq 3-12}$$

I_1, I_2 are DEF sensitivities of the 1st and the 2nd emulsion respectively.

3.6 Modeling of the plasma radiation spectrum.

Modeling of the plasma radiation spectrum has been used in this work for two purposes: evaluation of an electron temperature from filtered time integrated pinhole images and evaluation of plasma parameters from time resolved spectral measurements (see Chapter 5). Two numerical codes applicable for these purposes are known: programs "FLY" [Lee 1995] and "NOMAD" [Ralchenko et al 2001]. Using both these codes has its advantages and drawbacks. The code "FLY" is commercially available and easy to use, but restricted mainly to spectra of K-ions and has a fixed set of atomic levels included in calculations. It hardly allows to analyze a possible role of electron or ion beams in spectra excitations. The code "NOMAD" covers a wider range of ions, including ions with filling L and even M-electronic shell. The last feature predetermined a choice of the code "NOMAD" for calculation of the recombination continuum of neon plasmas. Line radiation was calculated both using the code "FLY" and a simple atomic model based on data of collisional rates given in [Sobelman et al 1981]. Results of line radiation calculations were close to each other, but for some temperature range did not show regular temperature dependence. The Bremsstrahlung was calculated using Eq.C1 (Appendix).

It is known that in a plasma focus directed electron and ion beams may be produced, which in some cases can be a reason for strong radiation. Nevertheless for estimation of plasma temperature we assume, that the electron energy distribution is Maxwellian and can be described by the temperature.

3.7 Choice of a filter set.

The absorption cross section of the absorber has an edge structure at energies corresponding to the ionization energies of various atomic shells. Beyond the edges, the absorption coefficient is a monotonically decreasing function of the incident photon energy

$$\sigma(\hbar\omega) = \sigma_0 \left(\frac{\hbar\omega_0}{\hbar\omega} \right)^{\alpha}, \qquad \textbf{Eq 3-13}$$

where the α coefficient is close to 3 for all materials, σ_0 depends on the material used.

The radiation intensity thus incident on the detector is an integral of radiation density behind the filter over all frequencies and plasma lifetime

$$I_C(T_e, t_{life}, d...) = \int_0^{t_{life}} \int_{\hbar\omega=0}^{\infty} P(\hbar\omega, T_e, t, ...) \exp(-\rho\sigma(\hbar\omega)d) d(\hbar\omega) dt \,, \quad \textbf{Eq 3-14}$$

where all processes with emission of the photon contribute to P.

We consider the radiation intensity due to recombination and Bremsstrahlung passing through the filter. Intensities of Bremsstrahlung and recombination radiation between recombination edges have the same exponential dependence

$$I_{f-f}, I_{b-f} \propto e^{-\frac{\hbar\omega}{kT_e}} \,. \quad \textbf{Eq 3-15}$$

On the other hand the transmission of filters is

$$T_\omega \propto e^{-Cons\tan t \cdot \left(\frac{1}{\hbar\omega}\right)^\alpha}, \alpha \approx 3 \,. \quad \textbf{Eq 3-16}$$

Since 10ì m Be filters (Figure 3-2) have a high transmission for K-ions line radiation, they were not used in the analysis. A set of images was produced with 90μm and 200μm beryllium filters. Images were recorded with a double-pinhole (∅40μm) set-up on the KODAK x-ray film.

Nevertheless, transmission of the 90μm Be filter in the wavelength region of H-like neon line emission (resonance transitions 2p-1s) is still relatively high. It is therefore necessary to take the line emission of this ion into account when modeling the spectrum. For simplicity reasons, all line radiation of H-like neon calculated with NOMAD for the given temperatures was assigned to 1s-2p and 1s-3p transitions.

Radiation spectra were calculated numerically for a set of plasma temperatures from 300eV to 5keV. An example of emitting spectra for temperatures 300 and 1000 eV is shown in Figure 3-10. The model spectrum corresponding to the electron temperature 300eV and 1000eV after different filters is presented in Figure 3-10.

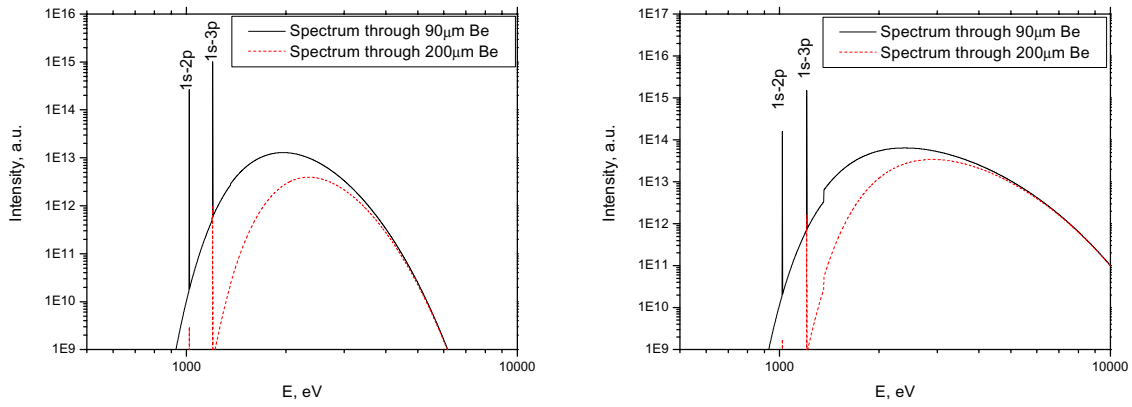

Figure 3-10. Model spectrum. Left) Te=300eV. Right) Te=1keV

It can be seen that for the filter of 200ìm Be the relative input of line emission into the total intensity is insignificant. When considering images of a neon plasma filtered with 200ìm Be it is possible to neglect line radiation.

If $F_0(\omega)$ is the number of photons necessary to produce the optical density $D_0=0.5$ on the KODAK x-ray film, then optical density produced on the time-integrated images is

$$D(T_e) = \int \frac{0.5 \cdot I_\omega(T_e) \cdot T_\omega}{\hbar\omega \cdot F_0(\omega)} d\omega, \qquad \textbf{Eq 3-17}$$

where T_ω is the filter transmission.

Eq 3-17 was numerically integrated for each filter and given temperatures using the results of the previous sections. The calculated ratio of optical densities vs. electron temperature for the taken pair of filters is given in Figure 3-11.

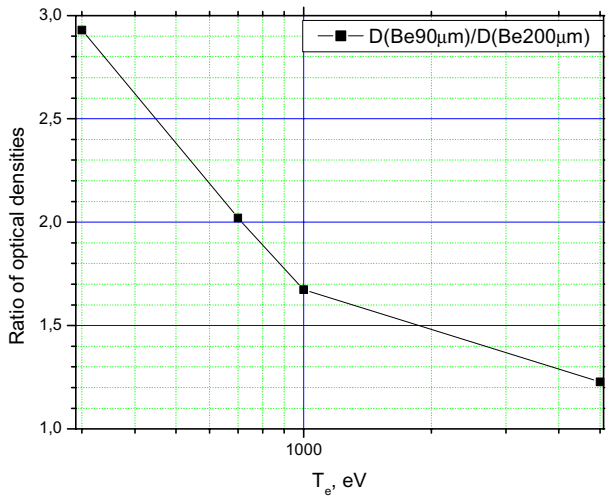

Figure 3-11 Ratio of produced image optical densities vs. the plasma electron temperature.

3.8 Data evaluation and results (Te)

Calculated ratios of optical densities of images of plasmas with different electron temperatures were compared with experimental data. An example of scans of a "bright narrow" column images with 90 and 200 ìm of Be is shown in Figure 3-12 (upper scan). The lower frame of the same picture represents results for a "diffuse column" image in the same shot. For different shots the ratio of optical densities for the "bright narrow" image type was measured to be between 1.5 – 1.7. Plasma temperature of the bright plasma column (upper plot) was found to exceed 1keV.

For the “diffuse” plasma column the measured ratio was somewhat higher, close to 2, with a corresponding electron temperature around 700-800 eV.

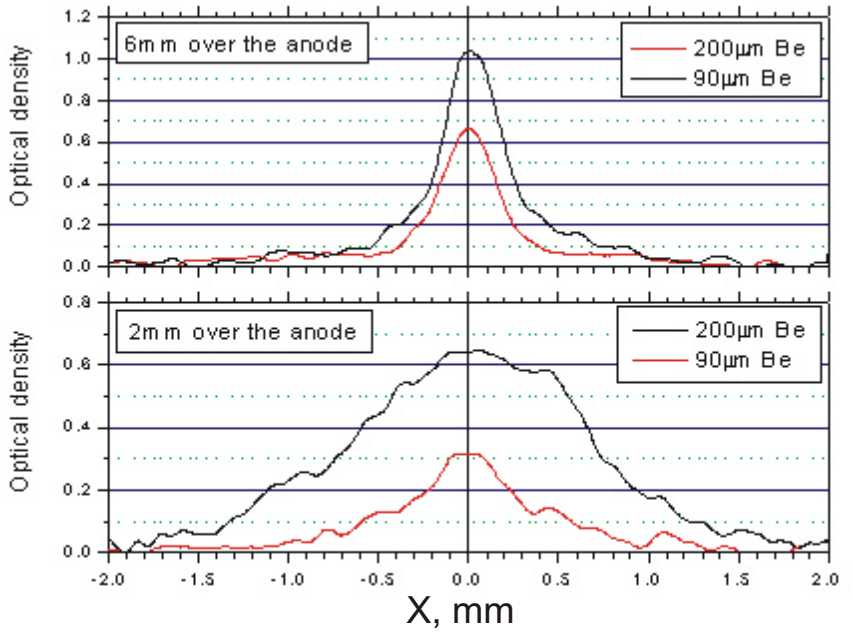

Figure 3-12. Pinhole time-integrated image scan.

4 Time-resolved filtered pinhole imaging of pinch compression.

Time-integrated diagnostics discussed in the previous chapter was used as a method for obtaining preliminary rough information about the plasma. In fact, only the time-averaged properties of the plasma column could be measured. The hot and bright plasma filaments embedded into the diffuse column as seen in time-integrated images has drawn much attention. The history of the pinch phase can help for better understanding of the plasma column formation and probably can give a hint of how the bright plasma filaments are formed.

To study dynamics and parameters of the plasma during the process of compression we applied time-resolved filtered pinhole imaging and x-ray spectroscopy of He- and H-like ions. Time resolution became possible due to the usage of time gated microchannel plates (MCP) as detectors of radiation forming either images or spectra. Basic principles of MCP, its characteristics and description of the cameras used in our experiments will be given later (Chapter 5) together with our results of the MCP camera calibrations.

Timing and experimental set-up.

In the experiment pinhole imaging was synchronized with obtaining spectroscopic data from the plasma. Time gated microchannel plate detectors (MCP) allowed for recording the x-ray images and spectra with time-resolution on the conventional photographic film.

To provide independent time gating, each MCP sector (quadrant) in pinhole imaging and an MCP strip in spectroscopic experiments were gated by a high-voltage pulse generator. The pulse generator has four outputs with pulse voltages adjustable from 4kV to 6kV. The duration of the pulse can be adjusted by changing the length of an impulse forming cable in the trigger box and was chosen 10 ns for all our experiments. Using the Stanford delay generator (DG535) for initiation of MCP trigger pulse we could trigger the detection system at any specified moment of the discharge.

Time correlation of all diagnostics is essential for a proper analysis of recorded data. Therefore, much attention was paid to careful timing of the diagnostics.

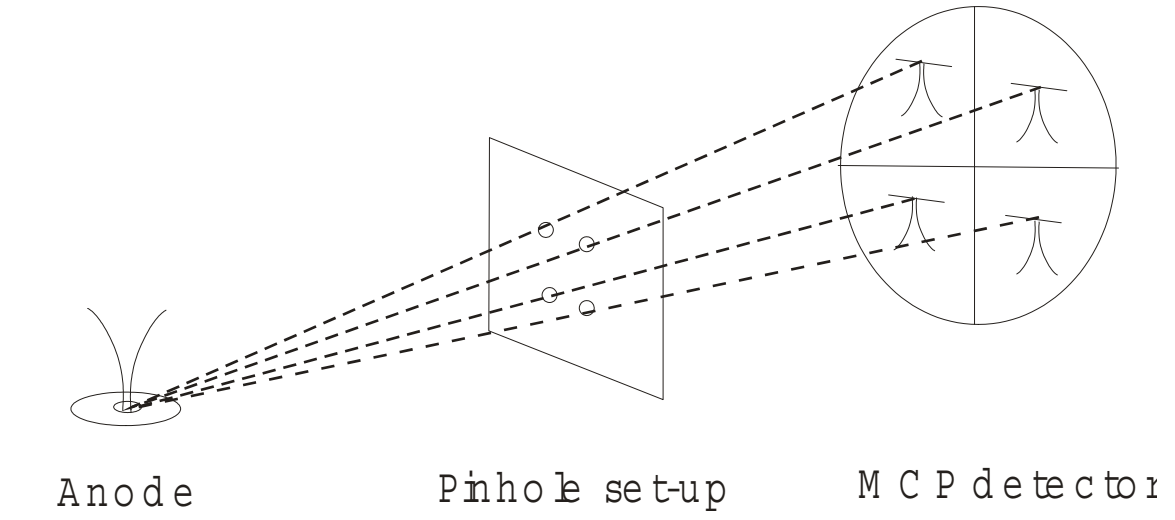

Figure 4-1. Time-resolved pinhole imaging set-up.

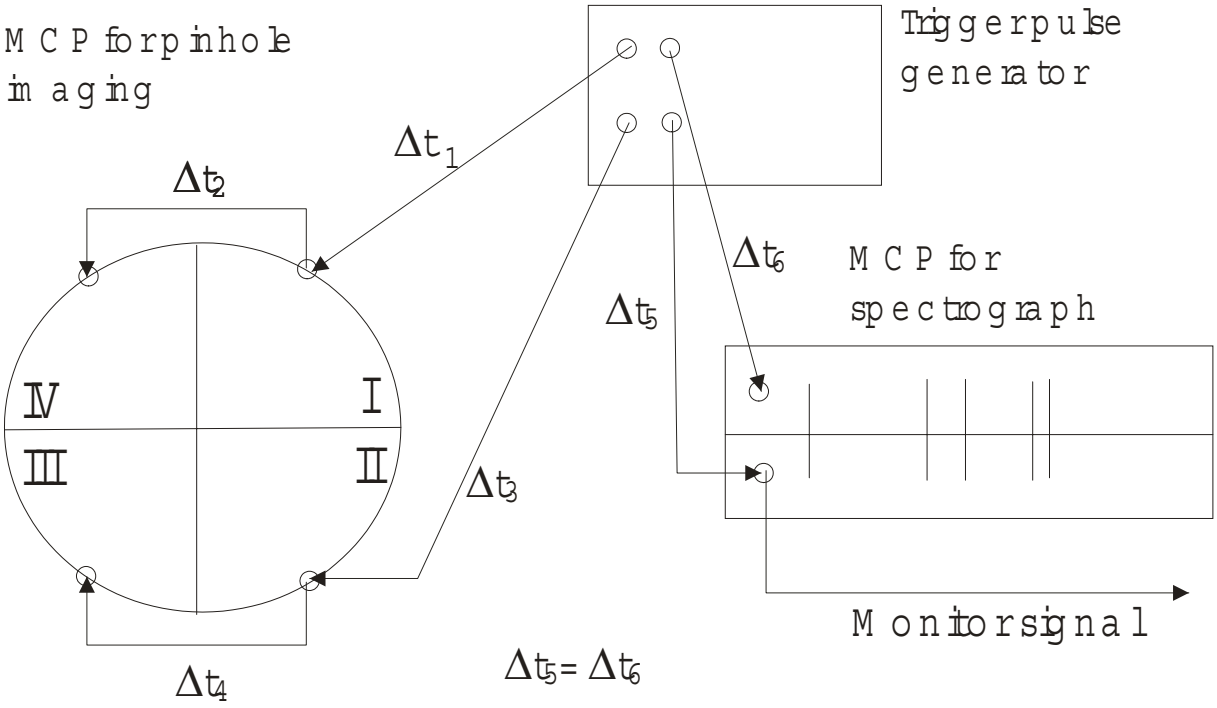

Figure 4-2. Timing of the 4-frame MCP detector.

A pinhole imaging set-up with a four-frame MCP detector is shown in Figure 4-1. A scheme showing the timing of opening of different quadrants of 4-frame MCP camera and of a strip on an MCP camera in a spectroscopic channel is explained in Figure 4-2. All 4 outputs of the pulse generator produce simultaneous HV pulses. Two frames of the MCP (shown as I and III) were fed directly from the trigger generator with a delay Δt_I and Δt_{III} respectively. Two others (II and IV) were connected in series to one of directly triggered frames with an additional delay Δt_{II} and Δt_{IV}. At the end of each pair a 50Ω terminator was installed. The time delay of individual MCP frames is determined by the length of cables between the pulse

generator and the MCP frame (one meter corresponds approximately to the time delay of 5ns). The other trigger box outputs supplied an opening pulse for the MCP, installed in spectroscopic diagnostics. It was arranged that one of the MCP frames in the pinhole imaging system always coincided in time with recording of an x-ray spectrum.

One of the trigger pulses after the MCP detector was recorded as a monitor signal on the oscilloscope together with dI/dt and voltage traces. With the help of the monitor signal an exact timing of diagnostics could be determined. All time delays of diagnostics were measured relative to the moment of "pinch stagnation", determined from dI/dt signal as shown in Figure 4-3:

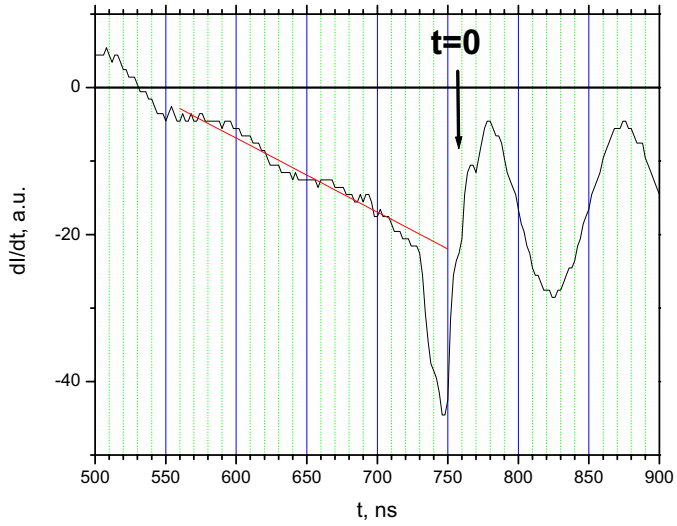

Figure 4-3.Timing of the diagnostics.

Practically, all time delays were initially measured relative to the first minimum of dI/dt spike. We know that stagnation (t=0) occurs about 10ns after the spike [Kies 1982].

Time resolved filtered pinhole imaging.

The experimental setup is outlined in Figure 4-1. The pinhole installation had four industry manufactured inserts, each with a pinhole of 40μm in diameter. The pinholes were arranged symmetrically with respect to the optical axis, so they produced four equally spaced images of the source in the detector plane. Each pinhole was covered with 10μm Be + 12μm Al filter (Figure 4-4). The geometry of the registration set-up allowed for recording images of the whole pinch, each image on its own MCP frame.

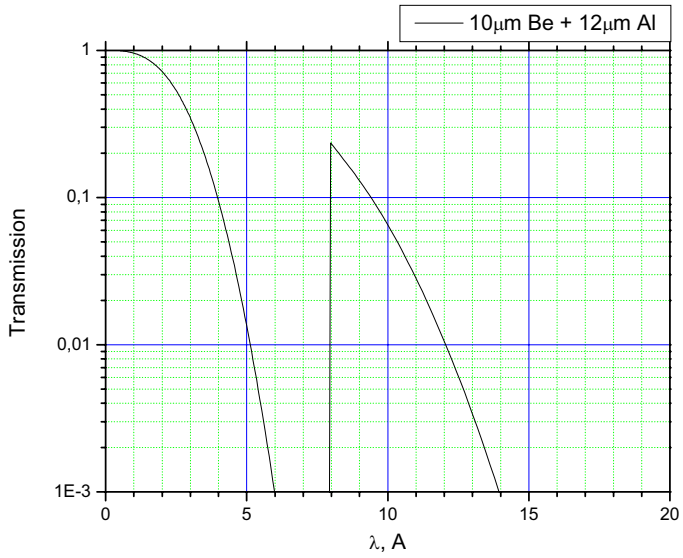

Figure 4-4. Transmission of 10μm Be+12μm Al filter.

Pinch dynamics.

The dynamics of the discharge in the compression phase can be seen in a sequence of MCP images. The diagnostic system was set to produce 4 frames per shot, each time-gated with a pulse of 10ns duration (FWHM). The duration of the discharge is longer than the time-span available. Therefore, the series of images we present is constructed from images produced in many shots. Moreover, due to time jittering in the discharge dynamics and in the diagnostic system many shots were required to arrange a good sequence of images.

Below we present data concentrating on the final phase when the discharge column shows an unstable behaviour. Images were always placed in a time sequence.

The dynamics of the plasma column is shown below for gas injection parameters p=3.5bar, τ=5-6ms.

The plasma column starts to be seen 10-20 ns before the stagnation point (Figure 4-5). It appears as a relatively short (16mm visible length) cone-like column with r≈2.5mm near the anode and r≈4.5mm at the other end. In the next 15ns the height of the column increases up to ≈25-30mm, with the diameter of the column remaining almost constant r≈2-3mm. An extra image c* shown for t=+5ns is from the same shot as the corresponding upper image. The image was recorded at slightly lower voltage applied to the MCP, that is with a lower MCP gain (pictures taken at the lower MCP gain will be marked throughout with an asterisk). It shows, that the plasma column is not homogeneous along the axis, and the radius can have a minimum in the middle of the column.

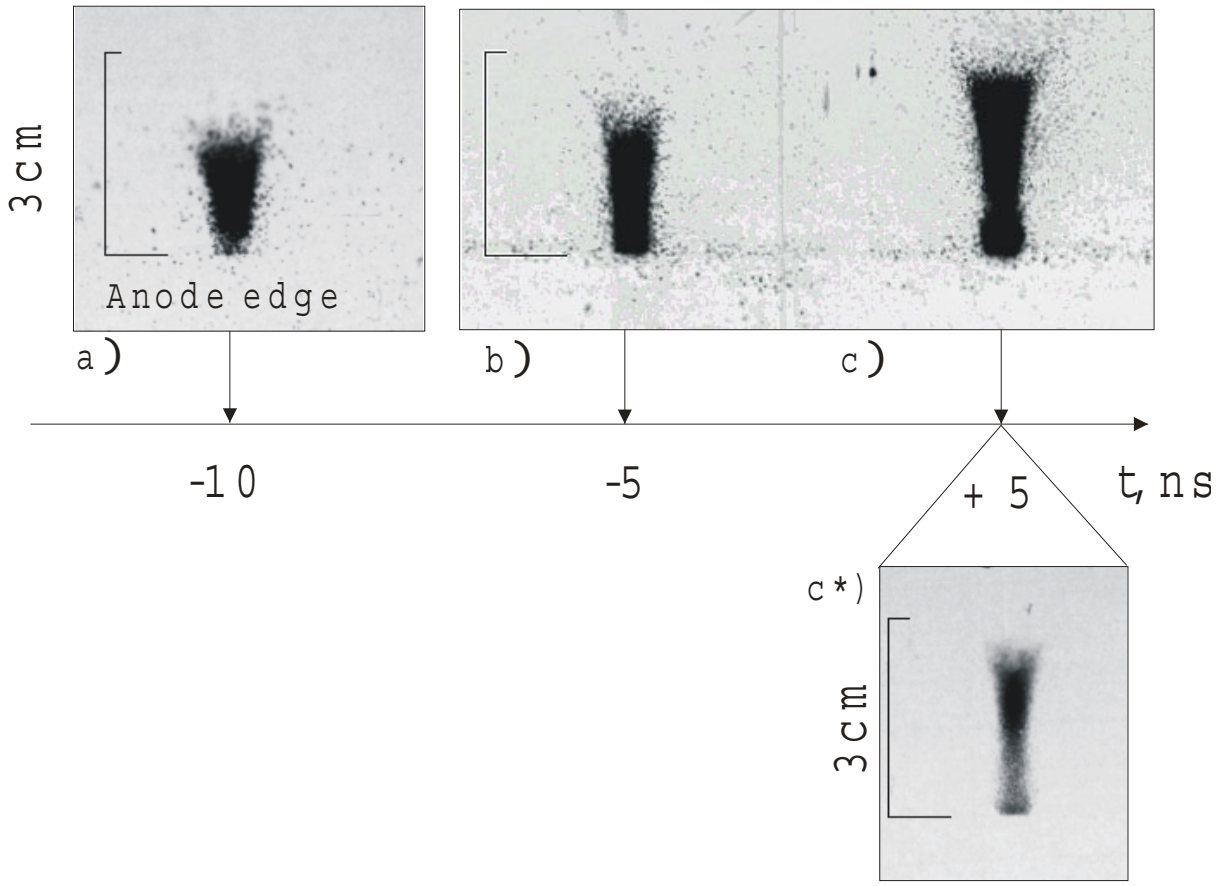

Figure 4-5. Start of the pinch phase

After stagnation (t=0), further pinch compression may result in different plasma configurations. One possible outcome is the development of a neck-instability, which is clearly seen in the sequence of images presented (Figure 4-6, Figure 4-7) below starting from t≈+10ns

Type I instability development.

After stagnation the image of the column near the anode becomes less dark and a few ns later an instability starts to develop near the anode. The instability appears with dimensions r_{min}≈2mm, h_{max}≈9mm (Figure 4-6d, d*). In the next 10-20ns it develops into a thin column r≤0.5mm, h≈4-5mm (Figure 4-7b, c). Further development is not longer seen by the MCP camera Figure 4-7d. In some frames (Figure 4-7c) one can still detect the lower and the upper ends of this column and thus estimate its size. From the successive images taken in the same shot the velocity of an instability development can be estimated to $7\cdot10^6$cm·s^{-1}-$1.5\cdot10^7$cm·s^{-1}.

Here it should be noted, that though the compression velocity is large, no smearing of the image boundaries due to plasma motion can be observed, which could be expected

provided MCP opens for 10ns. Since MCP gain nonlinearly depends on the voltage applied, effective gating time of the MCP is less than the duration of the trigger pulse, presumably ≤3ns.

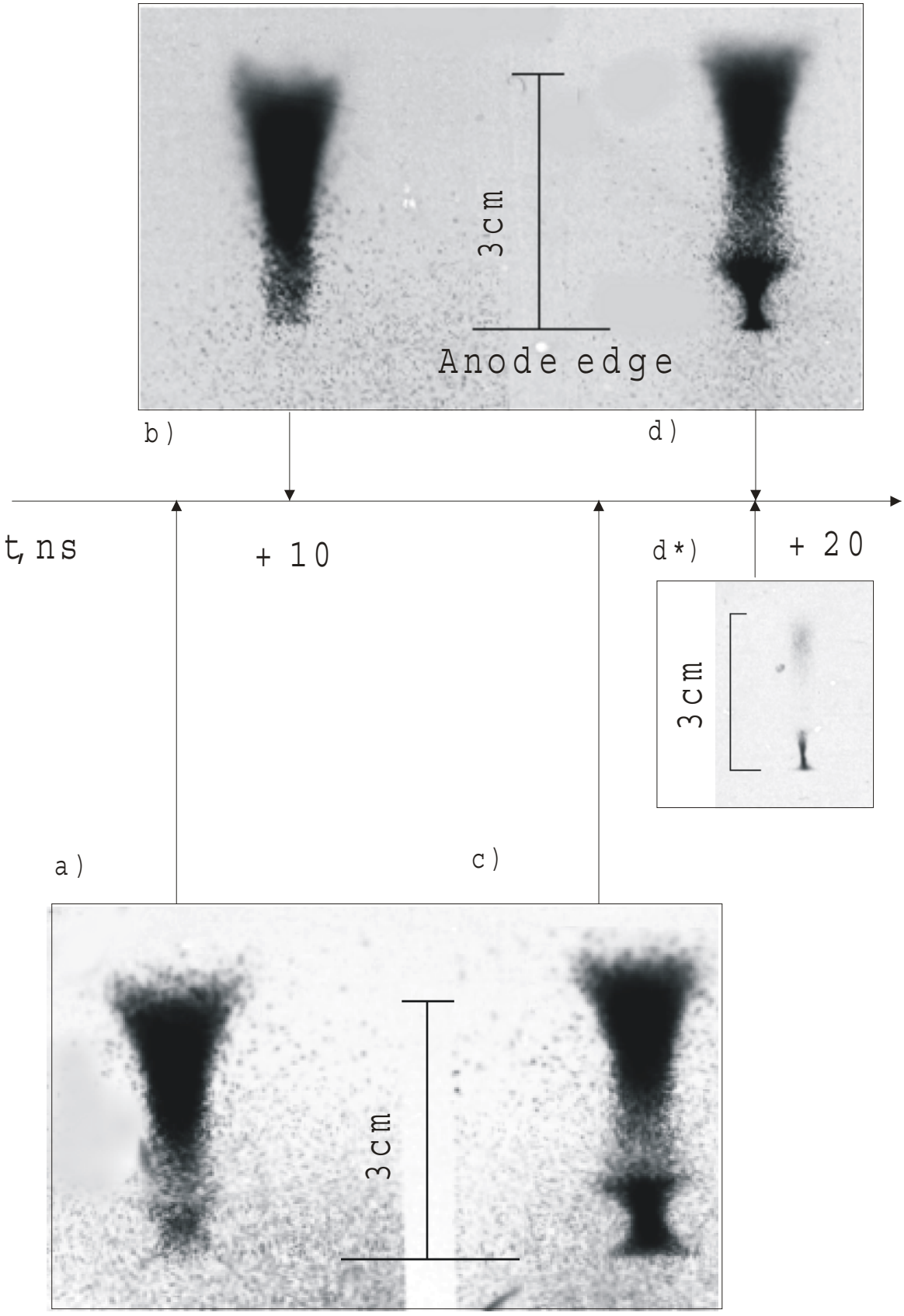

Figure 4-6. Instability development.

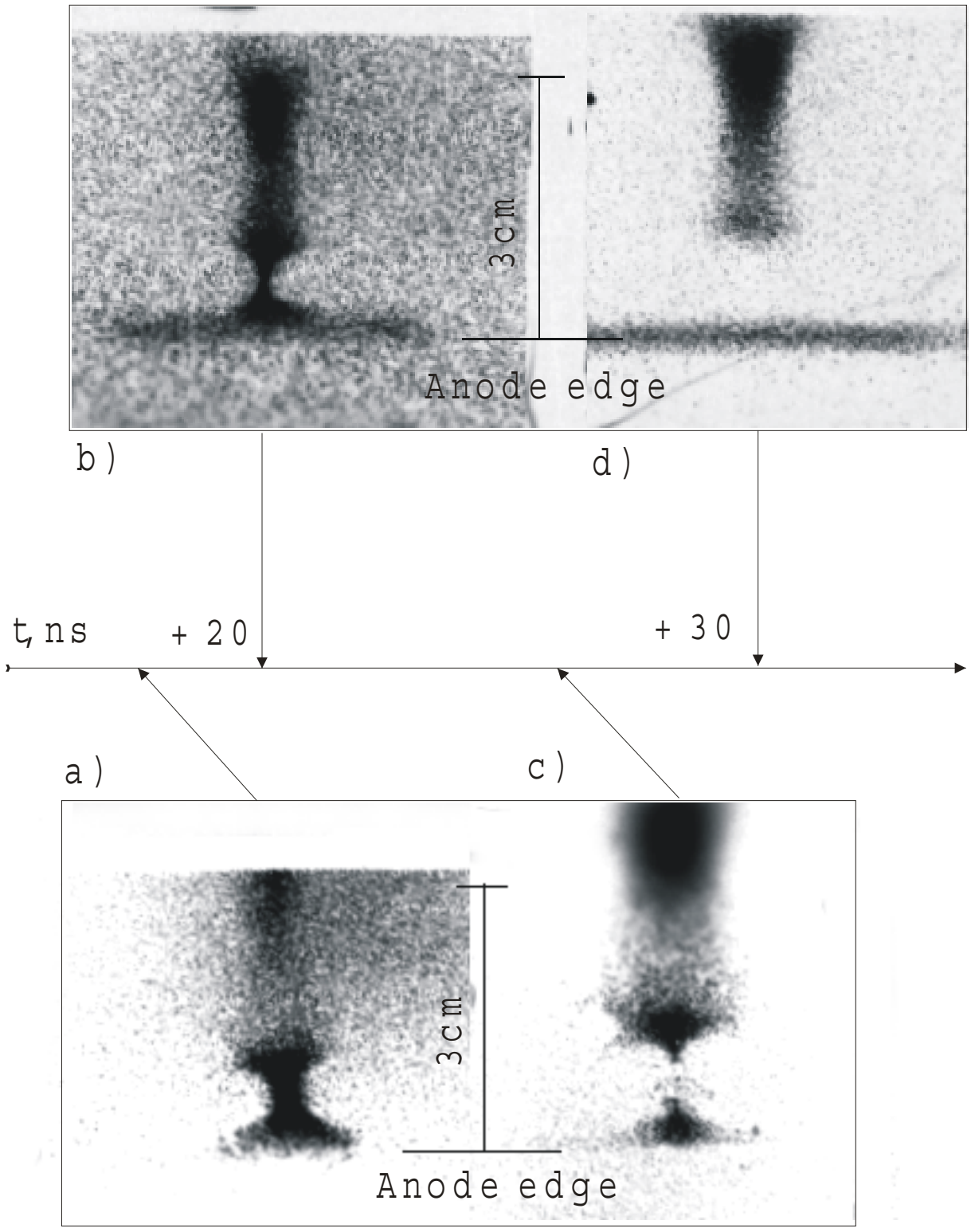

Figure 4-7. Instability development.

This Type I instability sometimes develops inclined to the side from the discharge axis, as shown in Figure 4-8.

Sometimes a development of multiple instabilities in the plasma column was seen. Two examples are shown in Figure 4-9 and Figure 4-10.

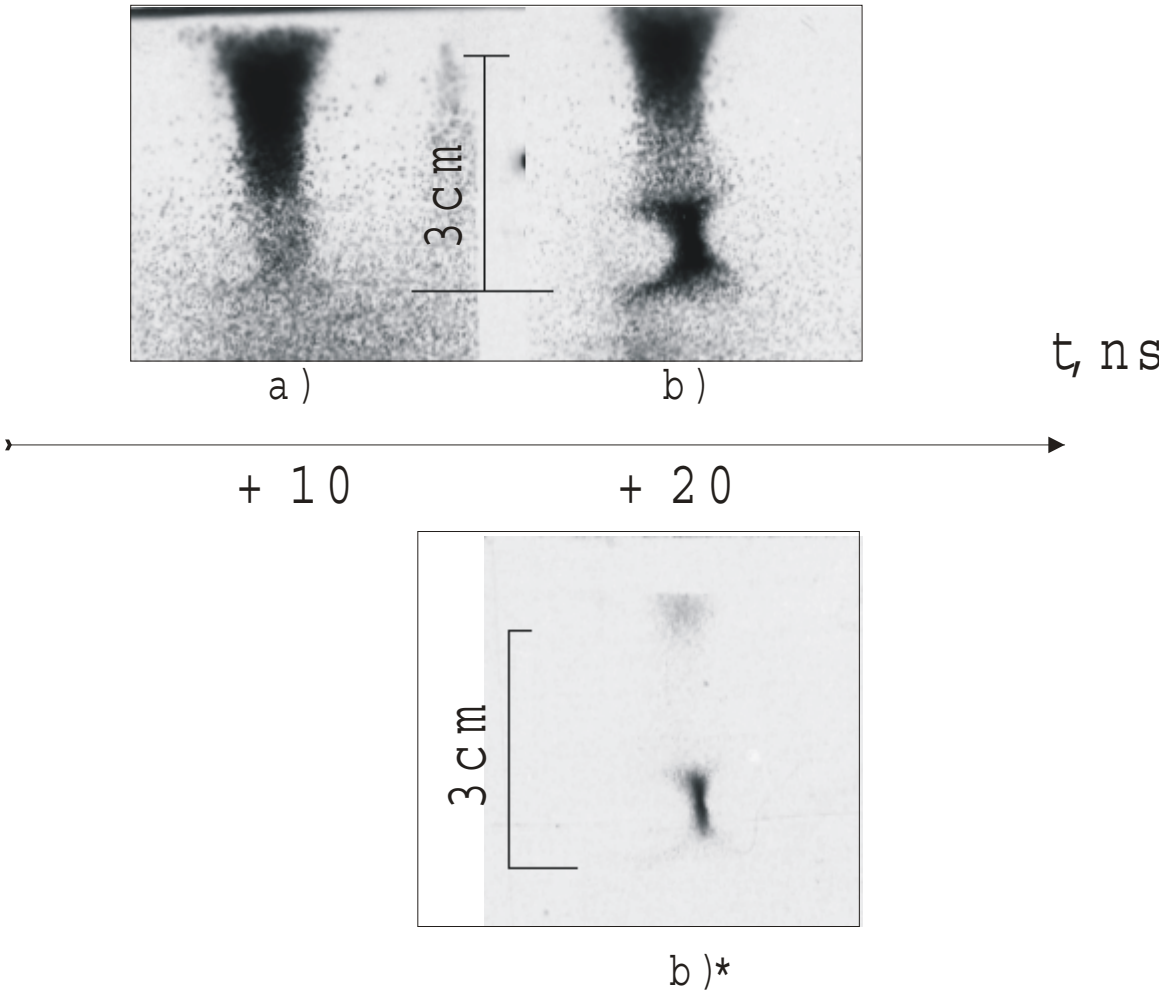

Figure 4-8 Pinch asymmetrical to the discharge axis.

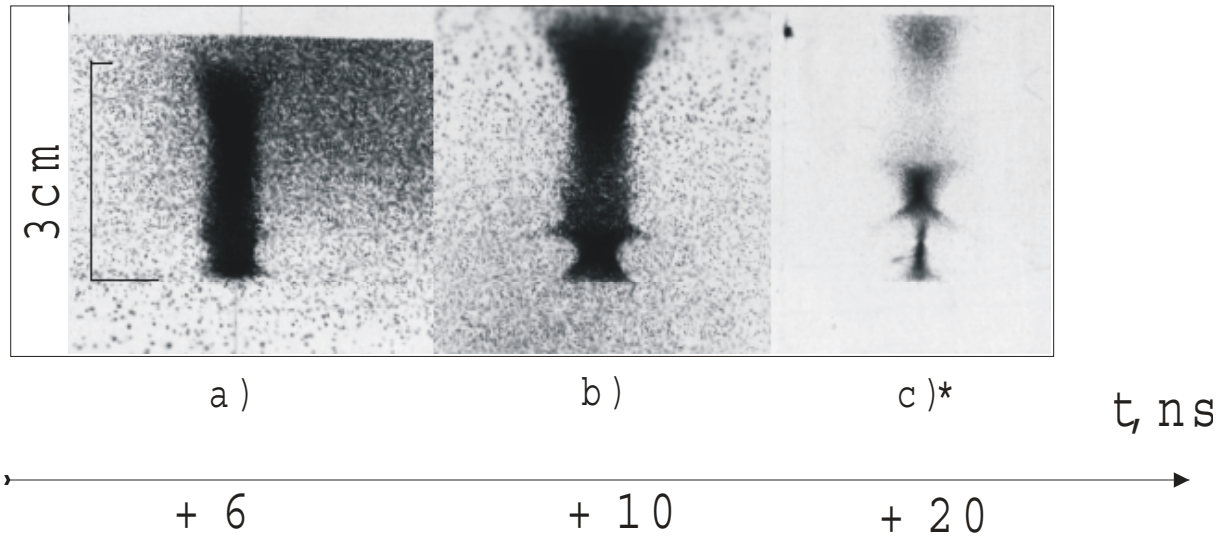

Figure 4-9. Double instability development. Injection delay 5ms.

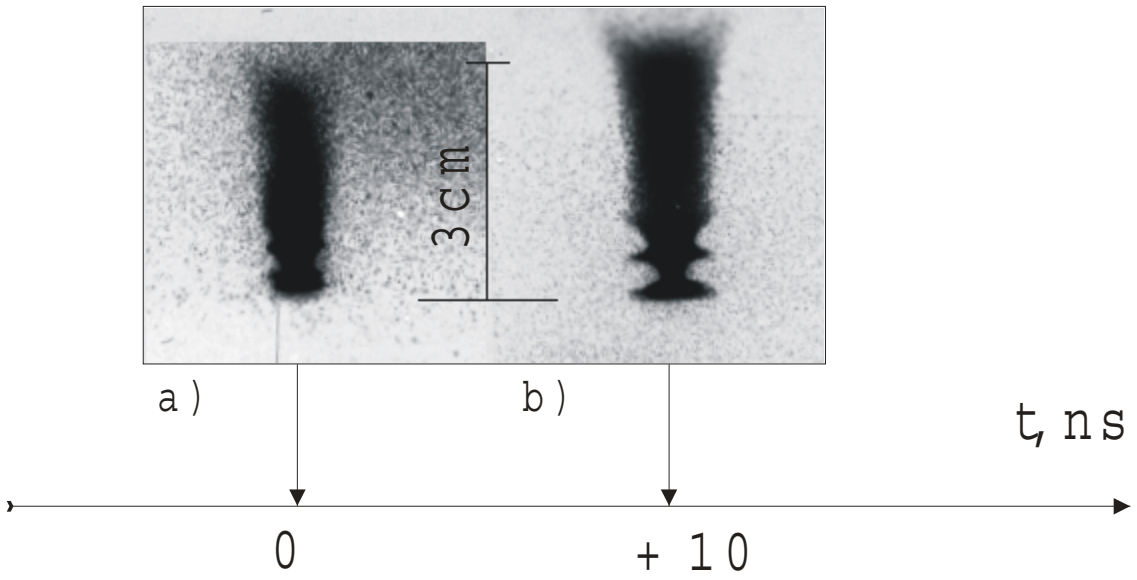

Figure 4-10. Double instability. Injection delay 7ms.

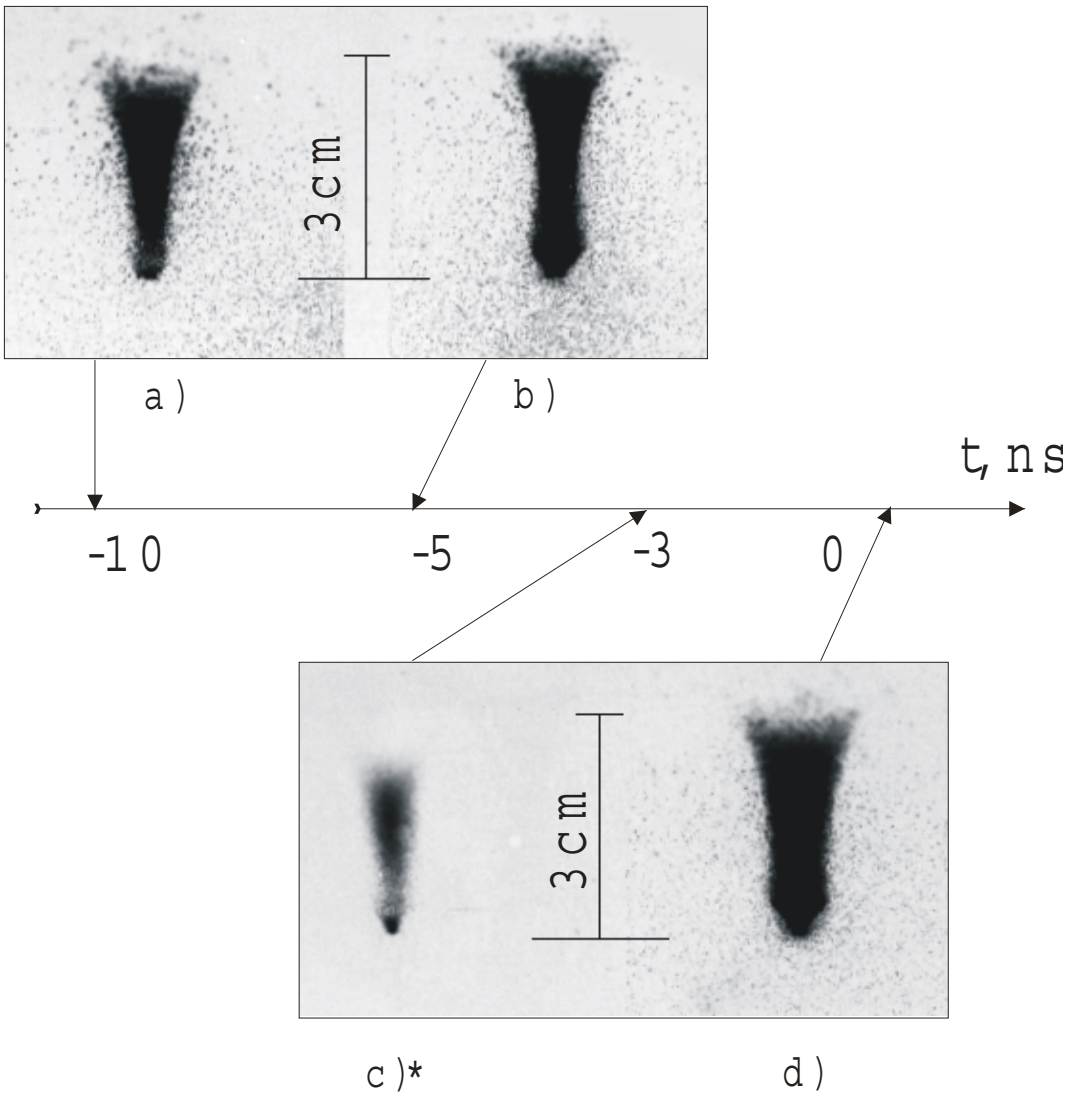

Figure 4-11. Type II instability development.

Type II instability development.

In some shots, after the column stagnation, instead of a big-scale instability of Type I, a short pinch appears near the anode (Figure 4-11). The image Figure 4-11c* is obtained on the MCP frame with lower gain.

This point-like pinch has typical dimensions r≈h≈1mm.

5 Time-resolved X-ray spectroscopy

5.1 Introduction

In this chapter results of time-resolved spectroscopic studies of the plasma column formation phase are presented.

In experiments with the big anode time-resolved x-ray spectroscopy of neon was successfully applied to determine the electron temperature of the plasma column [Kies et al 2000]. Measuring the slope of recombination continuum to H-like neon, the electron temperature 20ns before the "stagnation point" was determined to be 250-300eV. Considering the overlapping of line profiles of the high members of the Rydberg series in H-like neon at the same moment, the electron density was estimated to be equal or lower to $2.5*10^{20}$ cm^{-3}. Using time-integrated pinhole images small plasma columns radiating hard x-rays were detected. Their temperature was evidently higher than 300eV.

In the small anode geometry measurements of electron temperature from time-integrated images show that during compression the plasma column can be heated up to 1-2 keV. So, the time-resolved spectroscopy of K-ions (as discussed in Chapter 2) of neon was used to determine plasma parameters during the process of compression. Spectra were obtained spatially resolved over the plasma column length (z-resolved). Time-resolution was achieved by using the 10ns-gated MCP-detector.

Since, typically the time-resolved spectroscopy was used simultaneously with the time-resolved pinhole imaging, we were able to compare the spectrum and the image of the spectrum producing plasma column. By comparing spectra and corresponding pinhole images, we were able to determine the distribution of plasma parameters over the plasma column length.

5.2 Experimental set-up.

The scheme of the experimental set-up is presented in Figure 5-1. A slit with width 0.3mm placed before the spectrograph allowed for obtaining z-resolved spectra with a resolution $\Delta z \approx 0.8$mm at the source plane.

To separate the MCP detector, which has strict vacuum requirements, from the discharge chamber the z-resolving slit was covered with 7μm Al foil which is transparent to radiation of K-ions of neon.

The spectrum was recorded on a photographic film placed after the MCP detector.

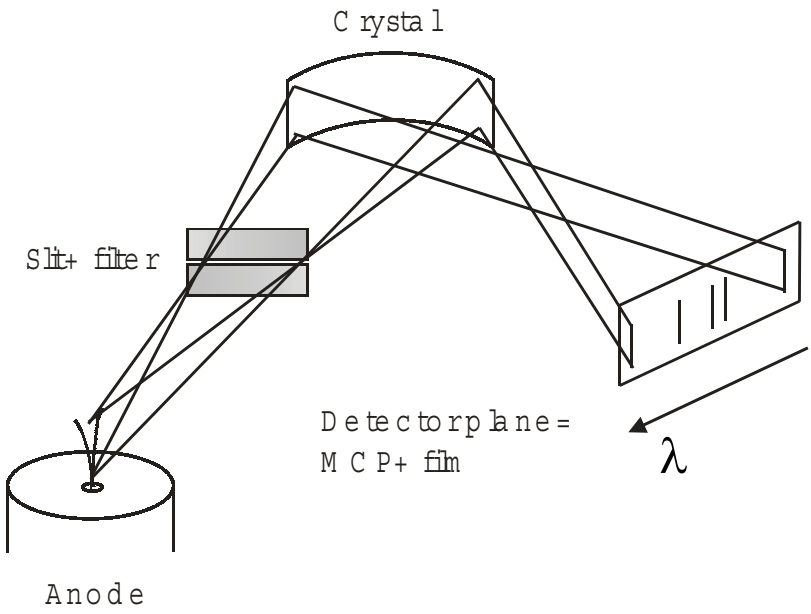

Figure 5-1. X-ray time-resolved spectroscopy set-up.

5.2.1 Microchannelplate detector (general principles, spectral region, time gating)

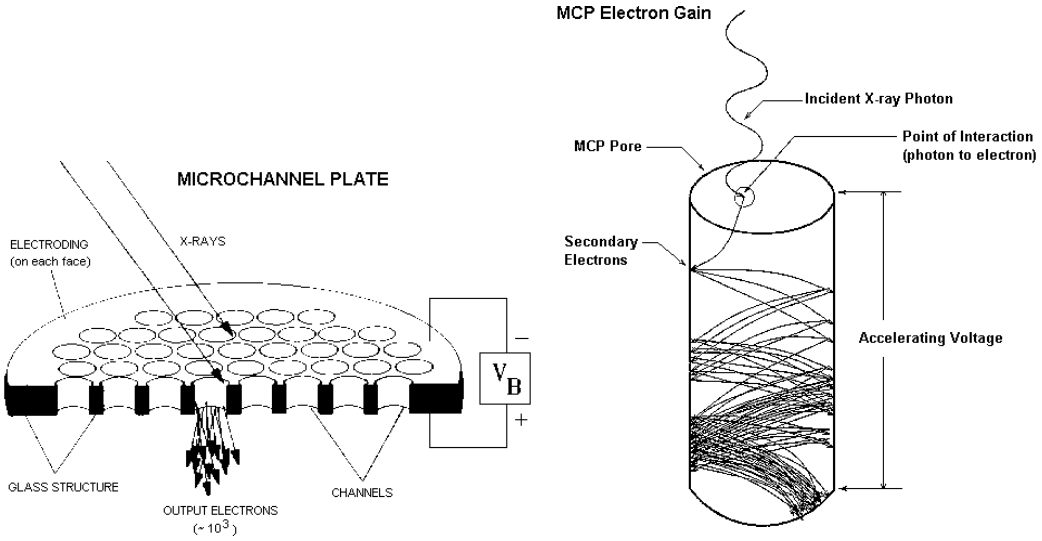

Figure 5-2. Microchannel plate (left), amplification principle of the channel (right)

Microchannel plates originally developed as amplification elements for image devices, have found numerous applications in different fields due to a number of remarkable properties. MCPs can detect charged and neutral particles and soft x-rays. MCP detectors have high temporal (<1ns) and spatial (~20μm) resolution, high internal gain and magnetic field immunity. One of the most important characteristics of MCPs is their detection efficiency. The efficiency for charged particles varies in the range of 20%-90% depending on

type and energy of the particle [Shikhaliev 1997]. Soft x-ray detection efficiency is 5%-14% in the energy range 0.02-10keV [Wiza 1979]. However when the x-ray energy increases, MCP detection efficiency decreases and becomes ~1% for energies ≥50keV [Bateman 1977].

The hard x-ray detection mechanism principally differs from the charged particle and soft x-ray detection mechanism. Incident charged particles or soft x-rays interact with the input surface of an MCP, while hard x-ray penetrates into MCP and the detection process is determined by the hard x-ray quanta interaction with the MCP material [Shikhaliev 1997]. Hard x-rays detection efficiency thus depends on several parameters such as MCP thickness, channel diameter, channel wall thickness, lead content in MCP material and energy of detected x-rays [Batemann 1977]. A number of models characterizing MCP was developed and can be found for example in [Shikhaliev 1997, Giudicotti 1994, Eberhardt 1979].

5.2.2 Calibrating "MCP + Film" detector

As it was described in previous sections, the spectral diagnostics set-up consisted of an x-ray focusing spectrograph on KAP crystal (d=26.6A), microchannel plate detector and a film Ilford HP5 ISO400. The MCP detector itself is made of a microchannel plate (MCP), phosphor screen and a light guide plate. Photographic film was placed after the light guide plate for recording of the visible image on the rear side of the MCP detector.

A high-voltage triggered pulse generator produces pulses of 10ns duration and amplitudes up to 6kV. This impulse voltage applied to MCP detector is divided between MCP and a gap between the microchannel plate and a phosphor screen in a ratio ≈1:5. Electrons emerging from MCP channels are accelerated in this gap. Fast electrons then excite visible radiation in a phosphor layer.

The optical registration system contains two non-linear elements: MCP and film. Quantitative diagnostics requires calibration of both elements in a working spectral region. The spectrograph is considered a linear element with respect to incident on crystal radiation intensity.

Absolute intensity calibration could not be performed, due to the lack of a calibrated x-ray source. Nevertheless, since spectral diagnostics methods are often based on intensity ratios, relative calibration of the "MCP detector + film" could be enough for quantitative analysis of spectra in many cases. Diagnostics were planned in a narrow spectral region between 1s-2p ($\lambda \approx 12.2$Å) and $1s^2$-1s2p ($\lambda \approx 13$Å) transitions of neon ions.

Experimental set-up

We obtained a set of spectra of the Ly α and its satellites of the H-like neon for calibration purposes.

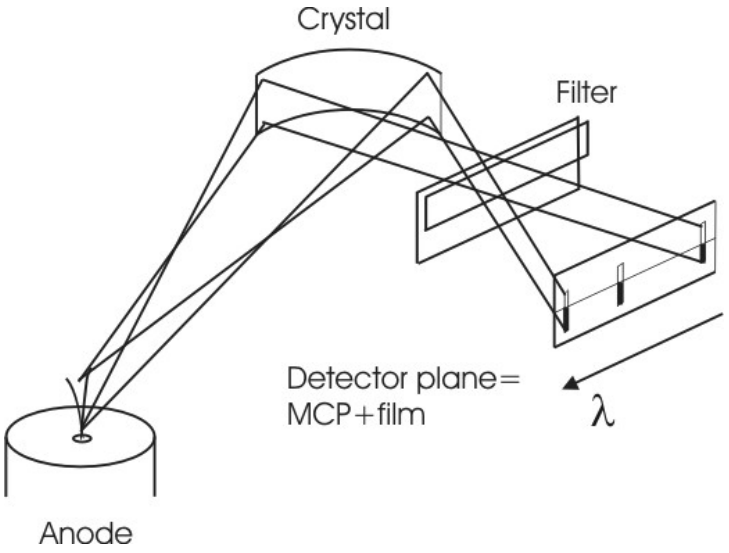

Figure 5-3. Calibration of "MCP+film" set-up

Before the crystal, a diaphragm D=1,5cm covered with aluminized mylar was installed. It is not shown on the schematic, because it does not play role in the calibration itself. Its purpose was to block VIS light from the detector. Although, the MCP detector is not sensitive to the VIS radiation, the light may pass through MCP channels and produce artifacts on the film. The diaphragm also provided for necessary vacuum requirements of MCP. It separated the MCP volume from the plasma focus chamber. MCPs require a pressure lower than 10Pa for proper operation. The plasma focus chamber is usually filled with several hPa of D_2. The diaphragm diameter was chosen to keep the pressure difference and not to blend the spectrograph crystal in the spectral region studied.

Homochromatic relative calibration of "MCP+film"

We obtained a few spectra of Lyα and satellites at different discharge moments. Calibration experiments were performed so that the unfiltered spectra had no intensity gradients along spectral lines.

On the outer flange of the spectrograph, a step filter was attached. It was assembled of three partially overlapping 7μm Al foil strips (see Figure 5-3), so the total thickness of the filter changed step-like along the height of the spectrum.

Incident intensity is attenuated in the foil filter, dependent on the number of subsequent foils passed:

$$I_k = I_0 \exp(-\sigma \cdot d_k),$$

where σ is the linear absorption coefficient of Al, d_k=k·7μm the thickness of the Al filter foil, k the number of foils.

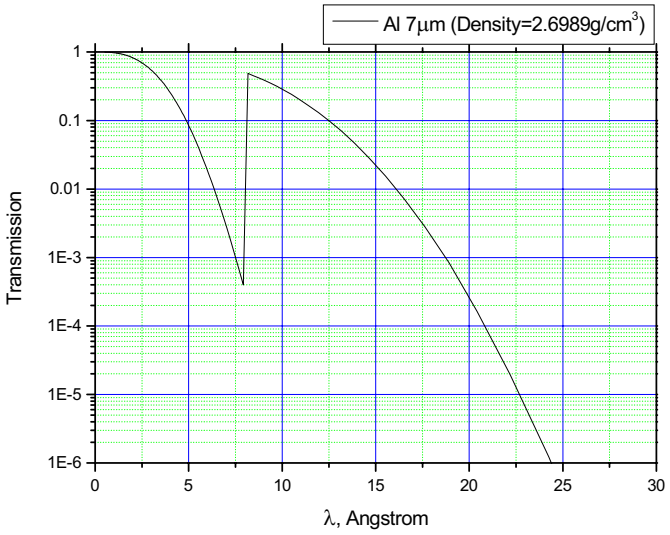

Figure 5-4. Al Transmission of 7μm Al.

The registration system was calibrated for a set of parameters, determining the response of the detection system. Two Ilford films with different sensitivity ISO125 and ISO400 were used as well as different MCP detector voltages (4.9kV-5.5kV). At output voltages lower than 4.9kV a noticeable time jittering between trigger and output impulses of pulse generator starts, so the lower limit is about 5kV.

The generator output voltage is divided between the microchannel plate and the gap where electrons are accelerated. The voltage applied to MCP plate is proportional to the voltage applied to the detector unit. We therefore take as a parameter the voltage applied to the whole detector. Films were developed at 22C for 6 minutes, in AGFA Refinal developer, then fixed and dried at room temperature.

In Figure 5-5 a typical calibration spectrum is presented.

We scanned each spectrum at positions, corresponding to a different number of filter foils k. For this purpose a standard analogous densitometer was used. In Figure 5-6 a typical result is shown.

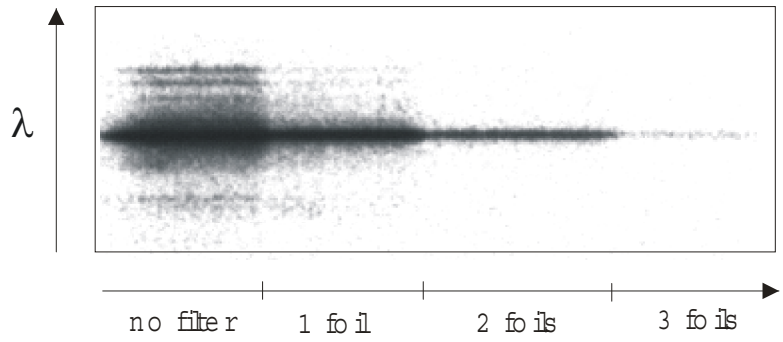

Figure 5-5. A typical calibration spectrum of Ly-α and its dielectronic satellites.

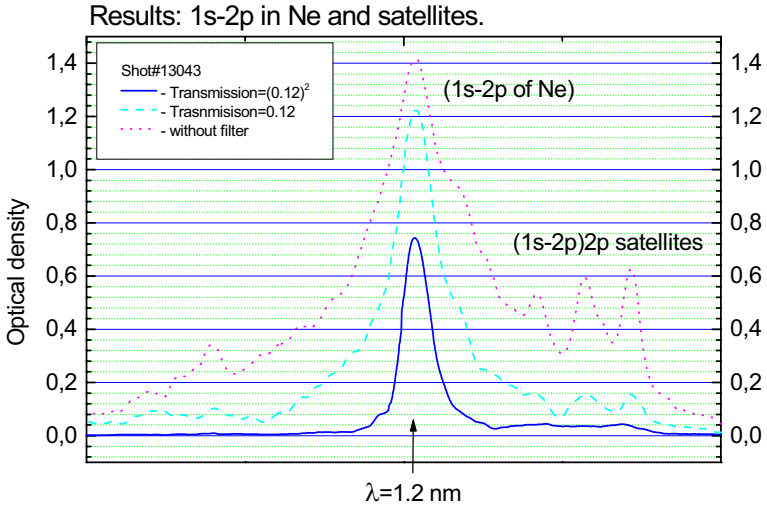

Figure 5-6. Densitometered calibration spectrum.

At every spectral position the calibration spectrum yields directly up to 3 points with a known relative shift on a *Log(I)* scale. Assuming the response is identical for all wavelengths in the selected narrow spectral range, every spectrum gives us actually a full set of data, necessary for building the calibration curve. Starting points were taken for the wavelength corresponding to the maximum of the Ly*α* line. Points taken from the line profile require precise positioning of the spectra obtained after different filters on the wavelength axis. These points can introduce a larger error than points from the line maxima.

A function $f(x) = \frac{A_1 - A_2}{1 + e^{(x - x_0)/dx}} + A_2$, where $x=Log(I)$ was taken to fit experimental data. The function parameter A_1 represents the lower asymptote level. It was manually set to 0, because the response should come to zero for low radiation intensities. At high intensities this function shows density saturation.

Starting points were fitted by *f(x)* and were taken as the 0th approximation. Then another pair of optical densities with a known ratio of intensities was added and manually shifted on a *Log(I)* axis to fit the model curve best. This procedure was repeated a few times, until the model curve and experimental points were in a rather good agreement.

The result is represented by a set of response curves for different trigger voltages and different film speeds.

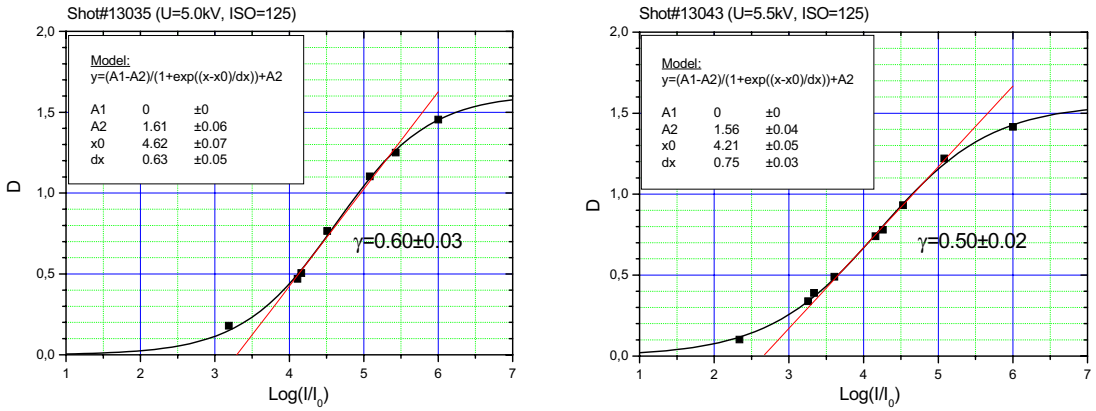

Figure 5-7. Characteristic curves for "MCP+ISO125"

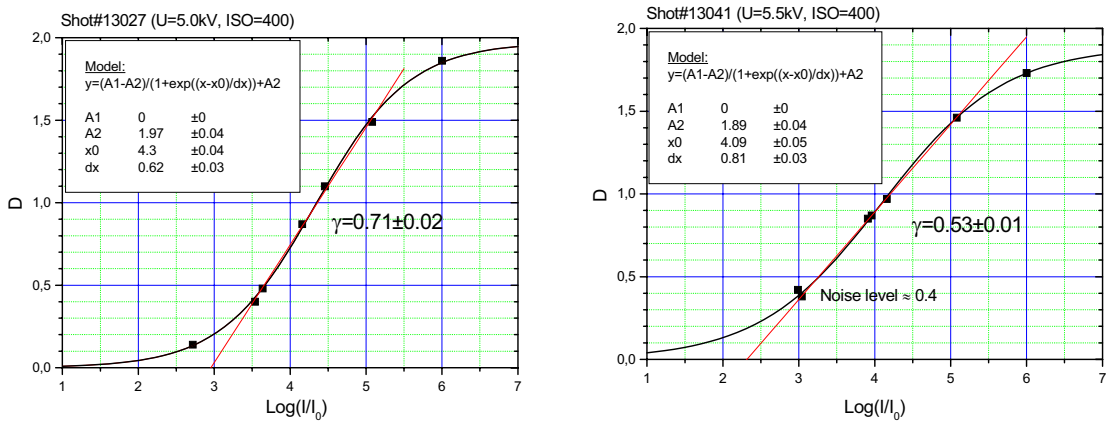

Figure 5-8. Characteristic curves for "MCP+ISO400".

If we assume that all shots in the calibration experiment were alike with respect to the radiation intensity, we can correlate all response curves to each other.

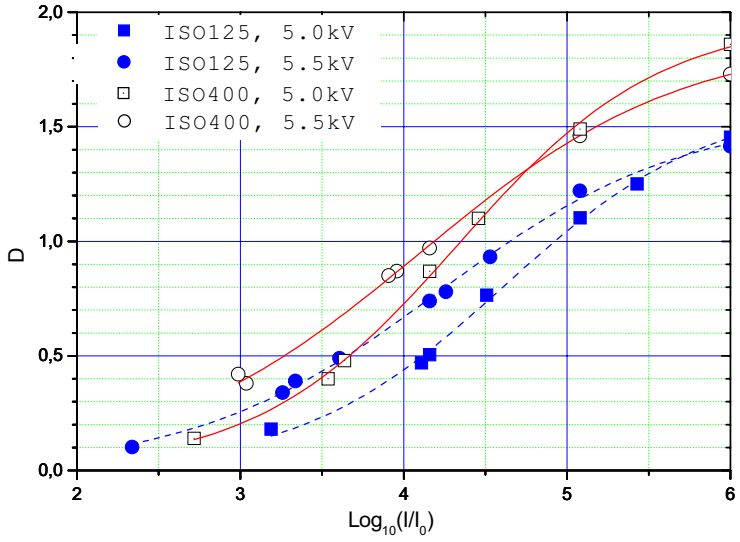

Figure 5-9. Comparison of characteristic curves.

The characteristic curves of the MCP detector + photo film can be discussed in terms of quantities usually applied for description of a photographic film response. Results are presented in Table 5-1. Values for sensitivities E_0 are obtained from the relative Log(I) scale and therefore given for the purpose of comparison only.

ISO, voltage	γ	E_0, arb.units	D_S	D_∞
ISO125, 5.0kV	0.60±0.03	3.3	1.3	1.61±0.06
ISO125, 5.5kV	0.50±0.02	2.6	1.3	1.56±0.04
ISO400, 5.0kV	0.71±0.02	3	1.6	1.97±0.04
ISO400, 5.5kV	0.53±0.01	2.4	1.6	1.89±0.04

Table 5-1. Parameters of characteristic curves of "MCP+film".

The gradient γ is a slope of the linear part of the characteristic curve. The exposure E_0 which is obtained if the straight part of the characteristic curve is extended to the line $D=D_0$ is a measure of the sensitivity (or speed) of the photo emulsion ($\sim 1/I_0$). D_0 is defined as the density of the unexposed parts of the developed film. The density D_s defines a shoulder of the characteristic curve, where γ begins to decrease. D_∞ is the saturation density.

The registration system becomes more sensitive with increasing voltages applied to the MCP detector. Results also suggest, that saturation of the systems may occur earlier if the

applied voltage increases. The experiment is not evident enough to prove the last statement. Still it is of certain interest to discuss possible sources of this effect.

In specifications to black-white films the company Ilford reports a characteristic curve, which has a $D_S \approx 2.2$ for ISO400 (HP5Plus) [Ilford] and $D_S \approx 1.8$ for ISO125 (FP4Plus) [Ilford]. From our experiment for the whole detection system we obtain smaller values for D_S, which could mean that the saturation seen is due to the MCP detector rather than to saturation of the photo-emulsion.

Since the properties of the emulsion strongly depend on development conditions, we have made an attempt to measure the saturation level of both films.

A film piece was exposed by an artificial light source (lamp) through a wedge filter for 10s and developed for 6 minutes in AGFA Refinal developer under standard conditions. With the transparency gradient of the wedge filter known, the film characteristic curve was determined. Characteristic curves are presented in Figure 5-10 (here D=0 corresponds to a fog level of each film. The fog level was subtracted in each case).

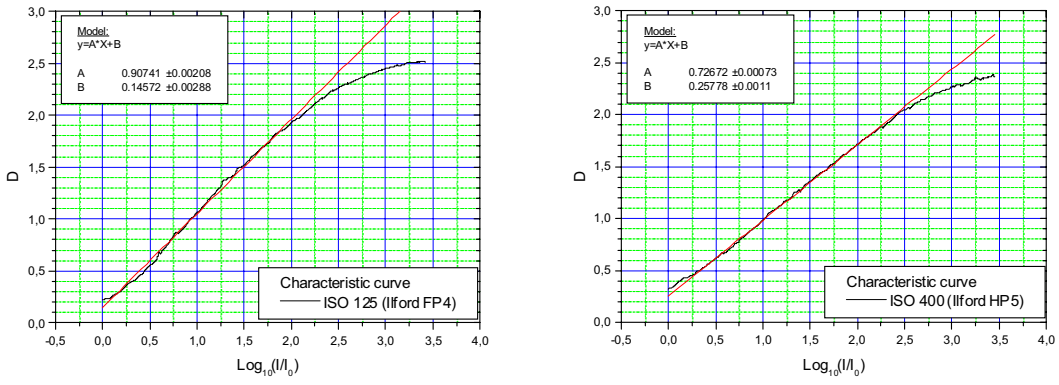

Figure 5-10. Characteristic curves of Ilford photographic films.

From characteristic curves we determined the film saturation density (when all grains are developed) and the optical density, when the film response starts to deviate from the linear behaviour. These parameters do not depend on exposure or developing conditions.

It can be seen, that Ilford FP4 ISO125 is linear up to densities D=1.8, Ilford HP5 ISO400 – up to D=2.0-2.2. The response of "MCP+film" exhibits non-linearity at essentially lower optical densities. Therefore we can conclude that overall non-linearity of the registration system is not due to the film, but to the MCP.

5.3 Determination of the electron temperature using satellites to the Ly_α transition of H-like ions NeX.

5.3.1 Satellites to the Ly_α line of NeX.

As it was described in Chapter 2, intensity ratios of some dielectronic satellites to resonance lines can be used for determination of the electron plasma temperature. From previous studies we could expect that the plasma under consideration consists mostly of so-called K-ions – He- and H-like ions of neon. Therefore, we had a choice between two types of satellites:

i) Transitions from doubly excited states in Li-like ions (1s2lnl'), which are satellites to the resonance line of He-like ions "W" or

ii) dielectronic transitions from doubly excited levels of He-like ions (***2lnl'***), which are in turn satellites to the resonance line of H-like ions – Ly_α.

In the example given in 2.6.1 one could see that generally speaking there are two channels of excitation of autoionizing states of Li-like ions – dielectronic capture (Eq 2.22) or/and collisional excitation of an inner shell electron (2.28) from the ground state of Li-like ions. This duality inserts a strong ambiguity in the procedure of the electron temperature determination, as the input from the channel (Eq 2.28) depends not only on the electron temperature but also on ionization equilibrium in a plasma. As it was indicated before, for non-stationary plasmas ionization balance may strongly deviate from equilibrium.

From this point of view the second choice – satellites to Ly_α line seems to be more preferable. Satellites to the Ly_α have only one channel of excitation, dielectronic capture from the ground state of H-like ion

$$\sigma_\omega^{lu} = \frac{1}{4}\lambda^2 \frac{g_{up}}{g_l} a_\omega, where - a_\omega \approx \frac{A_{ij}}{\Delta\omega_{ij}}. \qquad \textbf{Eq 5-1}$$

The schematic level diagram is shown in Figure 5-11. Levels with n=2 (***2l,2l'***) provide the strongest input to the satellite intensity. These are three configurations $\boldsymbol{2s^2}$***;*** $\boldsymbol{2s2p}$ and $\boldsymbol{2p^2}$ with a total number of levels equal to 10. These doubly excited levels of He-like ions can decay radiatively to the group of excited levels of He-like ions ***1s2s*** and ***1s2p*** originating satellites to the resonance $\boldsymbol{Ly_\alpha}$ doublet of H-like ion $\boldsymbol{2p^2P_{1/2,3/2} \rightarrow 1s^2S_{1/2}}$. A table of possible transitions is given below. As it can be seen from the level diagram a direct excitation of autoionizing levels ***2l2l'*** from the ground level of He-like ions assumes simultaneously two electron excitations. This process has a very low excitation rate and can be neglected when calculating intensities of satellites. One electron excitation is possible from the resonance levels

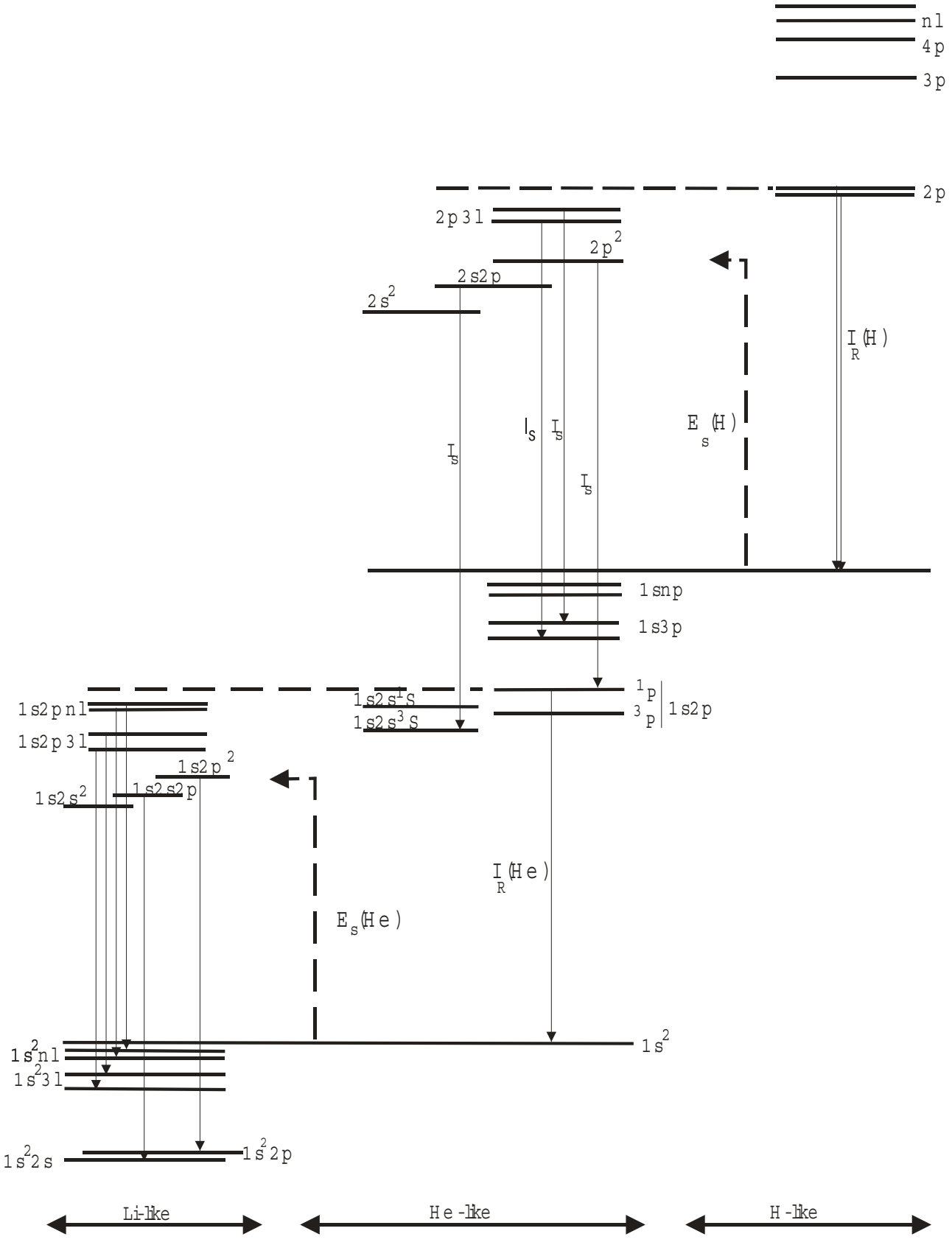

Figure 5-11. Diagram to determination of electron temperature.

of He-like ions (***1s2l***)

$$(1s2l)_{He} + e \rightarrow (2l,2l')_{He} + e' \qquad \textbf{Eq 5-2}$$

but these levels have generally quite low populations. As a result autoionizing levels populated mostly due to dielectronic capture (Eq 2.22) and line intensity is described by (Eq 2.24) and can be used for the electron temperature determination. Relative intensities of ***j→k*** line inside the satellites group are proportional to the factor ***q***

$$q(j \to k) = \frac{g_j}{g_0} \cdot \frac{\Gamma_j \cdot A(j \to k)}{\Gamma_j + \sum_k A(j \to k)}, \qquad \textbf{Eq 5-3}$$

where g_0 =2 is a statistic weight of H-like ion ground state. The q values as well as calculated in [Vainstein et al 1978] wavelengths of these transitions are given in Table 5-2.

Table 5-2. Satellites to the 1s-2p transition of neon.

Spectroscopic Notation Upper level - Lower level	Notation after [Vainstein et al 1978]	**λ, Å**	**$q \cdot 10^{13}$ c^{-1} intensity factor**
$2p(^2P_{3/2}) \rightarrow 1s(^2S_{1/2})$	R234-Y212	12.132	0
$2p(^2P_{1/2}) \rightarrow 1s(^2S_{1/2})$	R232-Y212	12.137	0
$2p^2(^1S_0) \rightarrow 1s2p(^3P_1)$	F111-B333	12.089	1.07e-5
$2p^2(^1S_0) \rightarrow 1s2p(^1P_1)$	F111-B133	12.173	5.82e-1
$2p^2(^1D_2) \rightarrow 1s2p(^3P_1)$	F155-B333	12.269	2.45e-5
$2p^2(^1D_2) \rightarrow 1s2p(^3P_2)$	F155-B335	12.272	8.74e-3
$2p^2(^3P_2) \rightarrow 1s2p(^3P_1)$	F335-B333	12.323	8.95e-2
$2p^2(^3P_1) \rightarrow 1s2p(^3P_0)$	F333-B331	12.326	0
$2p^2(^3P_1) \rightarrow 1s2p(^3P_1)$	F333-B333	12.326	0
$2p^2(^3P_2) \rightarrow 1s2p(^3P_2)$	F333-B335	12.329	0
$2p^2(^3P_0) \rightarrow 1s2p(^3P_1)$	F331-B333	12.328	5.35-e3
$2p^2(^1D_2) \rightarrow 1s2p(^1P_1)$	F155-B133	12.356	5.66
$2p^2(^3P_2) \rightarrow 1s2p(^1P_1)$	F335-B133	12.410	3.84e-4
$2p^2(^3P_1) \rightarrow 1s2p(^1P_1)$	F333-B133	12.413	0
$2p^2(^3P_0) \rightarrow 1s2p(^1P_1)$	F331-B133	12.415	1.53e-6
$2s2p(^1P_1) - 1s2s\ (^3S_1)$	C133-A313	12.139	3.58e-4
$2s2p(^1P_1) - 1s2s\ (^1S_0)$	C133-A111	12.262	1.75
$2s2p(^3P_2) - 1s2s\ (^3S_1)$	C335-A313	12.307	2.03
$2s2p(^3P_1) - 1s2s\ (^3S_1)$	C333-A313	12.310	1.22
$2s2p(^3P_0) - 1s2s\ (^3S_1)$	C331-A313	12.312	4.06e-1
$2s2p(^3P_1) - 1s2s\ (^1S_0)$	C333-A111	12.437	4.46e-4

$2s^2(^1S_0) - 1s2p(^3P_1)$	E111-B333	12.465	8.67e-4
$2s^2(^1S_0) - 1s2p(^1P_1)$	E111-B133	12.554	2.43e-1

Numerical code "FLY" and results of calculations. For the determination of the electron temperature the most strong satellite transition ***"J"*** $2p^{21}D_2 \rightarrow 1s2p^1P_1$ was chosen. Calculation of a diagnostic ratio ***"J"/Ly$_\alpha$*** was done with the help of a numerical code "FLY". A data set which is used in "FLY" for description of ***2l2l'*** dielectronic levels includes data for 6 possible combinations of total spin and orbital moment, known in spectroscopy as "LS-terms". No subdivision on levels with different total moment ***J*** is done. Nevertheless as the satellite ***"J"*** connects two singlet terms there was no need for additional level splitting. Energy levels, rates for autoionization and spontaneous radiative decay are taken from [Vainstein et al 1978].

For excitation of intensity of Ly$_\alpha$ line of NeX the code FLY employs a multilevel model describing level populations. Excitation rates were calculated using the Van Regemorter [Van Regemorter 1962] formula:

$$Rate_{ij} = N_e \cdot 2.50 \times 10^{-5} \cdot f_{ij} \cdot \frac{1}{E_{ij}\sqrt{T_e}} e^{-E_{ij}/T} . \qquad \textbf{Eq 5-4}$$

The effect of population redistribution between dielectronic levels due to electron collisions is not taken into account in the code "FLY". Nevertheless, this process does not influence the intensity of the *"J"* satellite but may produce some enhancement of lines originated from the $2p^2\,^3P$ term. As one can see from Table 5-2 these lines are well separated from both diagnostics lines (***"J"*** and ***Ly$_\alpha$***).

Results of calculations are shown in Figure 5-12.

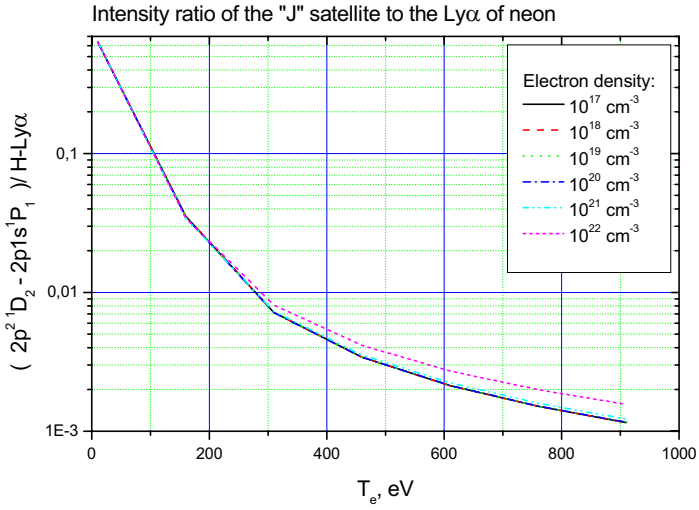

Figure 5-12. Intensity ratio of J-sat to Lya

5.3.2 Determination of electron density using W/Y intensity ratio.

The diagnostic method of determining the electron density of a plasma using intensity ratios of resonance and optically forbidden lines was described in Chapter 2. The intensity ratio between the resonance line of He–like ion – "***W***" line ***(1s2p $^1P_1 \rightarrow 1s^2\ ^1S_0$)*** and intercombination line – ***"Y" (1s2p $^3P_1 \rightarrow 1s^2\ ^1S_0$)*** is probably most widely used for these purposes:

$$\alpha = \frac{I(\text{"W"})}{I(\text{"Y"})} \qquad \textbf{Eq 5-5}$$

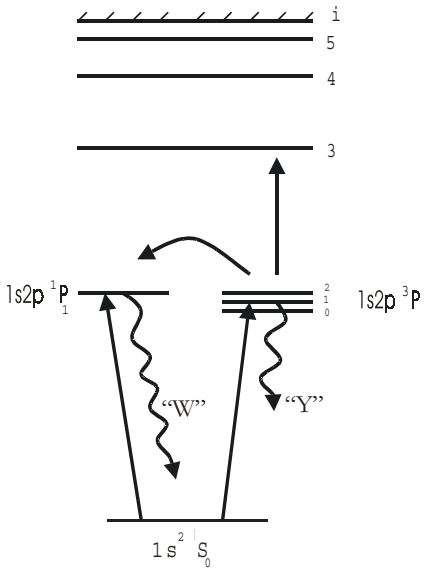

Figure 5-13 Simplified energy diagram of He-like ions

A simplified energy structure of He-like ions is shown in Figure 5-13.

Griffen and Peacock [1966] were the first who introduced the concept using this diagnostic ratio for determining the electron density. Kunze et al [1968] used this ratio in He-like ions of carbon in Θ -pinch experiments. Extended analysis of all physical processes involved was given in a theoretical work of Vinogradov et al [1975] and Skobelev et al [1978].

For very low electron densities all excited states are populated from the ground state by electron collisions and then decay directly or by cascade through emission of radiation. The relative intensities of spectral lines do not depend on electron density according to the coronal model. With an increase of the electron density the strongest metastable levels like $1s2s^3S_1$, $1s2p^3P_0$ and $1s2p^3P_2$ become additionally depleted by collisions to the nearby states. Radiative decay rates successively become lower than probabilities of collisional transitions between triplet states. For low Z elements collisional transitions between singlets and triplets are much less probable than collisional transition inside the triplet or singlet groups. In this

density range, deexcitation of all triplet states happens via "Y"line - ($1s2p\ ^3P_1 \rightarrow 1s^2\ ^1S_0$) and the ratio Eq 5-5 goes down.

At further increase of the electron density for some density range the ratio ***α*** is determined by the ratio of excitation rates of the singlet and triplet groups and again independent of density.

Finally, at higher densities the triplet states ***1s2s^{3}S*** and ***1s2p^{3}P*** suffer collisional losses to both singlet terms with principal quantum numbers n≥3 and step-wise ionization. Similar depopulation processes are of no importance for the resonance state ***1s2p^{1}P$_1$*** due to much higher radiative decay rates. As a result the relative intensity of intercombination line decreases and the ratio α increases almost proportionally to the electron density. In a very dense plasma the population of levels is Boltzmann-like (Eq 2-7) and equal for two close levels with equal statistic weights. Intensity ratios are proportional at high density to the ratio of Einstein coefficients for spontaneous decay.

The probabilities of the radiative decays of a singlet ***1s2p^{1}P$_1$*** and triplet level ***1s2p^{3}P$_1$*** and their ratio drastically change along He-like isoelectronic sequences. For He-like ions of neon Ne IX $A(1s2p^3P_1) \approx 8.9\cdot10^{12}$ s^{-1} and $A(1s2p^1P_1) \approx 5.6\cdot10^{9}$s^{-1} with the ratio ≈ $1.6\cdot10^{3}$. For the heavier ion Ar XVII rates are $1.09\cdot10^{14}$s^{-1} and $1.74\cdot10^{12}$s^{-1} with the ratio of ≈63 only. Correspondingly, the ratio ***α*** is diagnostically sensitive in different ranges against the electron densities – measurable densities are lower for lower charge of the ion used.

The ratio ***α*** calculated with the FLY code for a set of electron temperatures vs. electron density is presented in Figure 5-14:

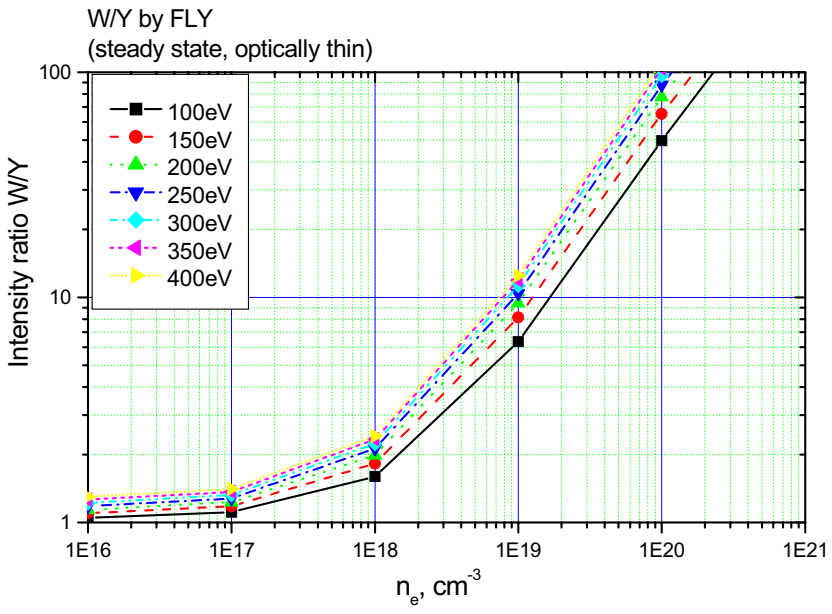

Figure 5-14 Theoretical ratio W/Y.

5.4 Time-resolved experimental spectra of He- and H-like ions of neon.

Below we present time-resolved pinhole images of the plasma column together with the spectrum in the vicinity of the resonance (W) and intercombination (Y) lines of He-like neon taken at the same time and in the same shot. In some positions satellites to the resonance transition are also seen. Time-gated pinhole images were obtained behind 10μm Be+12μm Al filter, as explained in Chapter 4.

From the ratio W/Y the electron density can be determined, as discussed in section 5.3. By comparing the image with the spectrum, one can qualitatively understand how the density of the plasma column behaves along the z-axis and how the density distribution correlates with the radius of the plasma column.

W and Y lines appear first near the anode surface, and then on higher z-positions. The length of the spectrum, as can be seen, is about the same as the visible length of the plasma column. As the plasma column becomes longer, the length of W-Y lines also increases.

During the period t=–5→+5ns the intensity ratio W/Y remains approximately constant along the z-axis. Spectra corresponding to two different z-positions are shown in Figure 5-16. The W/Y ratio weakly changes along the column length from 5.5 to 5.8, which corresponds to the electron density $(3\text{-}4)\cdot 10^{18}$ cm^{-3}. For a pinch diameter ≈ 0.5-0.6 cm this gives the total number of charged particles in a cross-section $(1\text{-}1.5)\cdot 10^{18}$ cm^{-1}.

As we know from time-resolved pinhole imaging 10-15 ns later neck-type instabilities start to develop in the region close to the anode. Pinhole images at this moment together with z-resolved spectra for two different shots are shown in Figure 5-17, Figure 5-19. Spectra are essentially inhomogeneous along the z-axis, demonstrating strong enhancement of the W-line at positions corresponding to the observed necks. At these positions the ratio W/Y increases thus indicating an increase of the electron density. In some shots the intensity of the Y-line in the neck region is lower than the detection limit and the line is hardly registered. Enhancement of the W line is accompanied by its broadening. Opposite to that, the intercombination line does not change in linewidth.

In necks the W/Y ratio reaches values of 18-20, which corresponds to an electron density of $(1.5\text{-}2)\cdot 10^{19} cm^{-3}$. With an estimated neck diameter 2-3mm the total number of particles in the neck cross-section is about $10^{18} cm^{-1}$. Lowering the total number of particles in the cross-sections indicates that compression from the diameter 5-6mm to the neck diameter 2-3mm is accompanied by plasma outflow. Assuming the constant current value the Bennett relation suggests higher electron temperatures in necked regions. This conclusion is supported by decrease of intensity of dielectronic satellites to the W line.

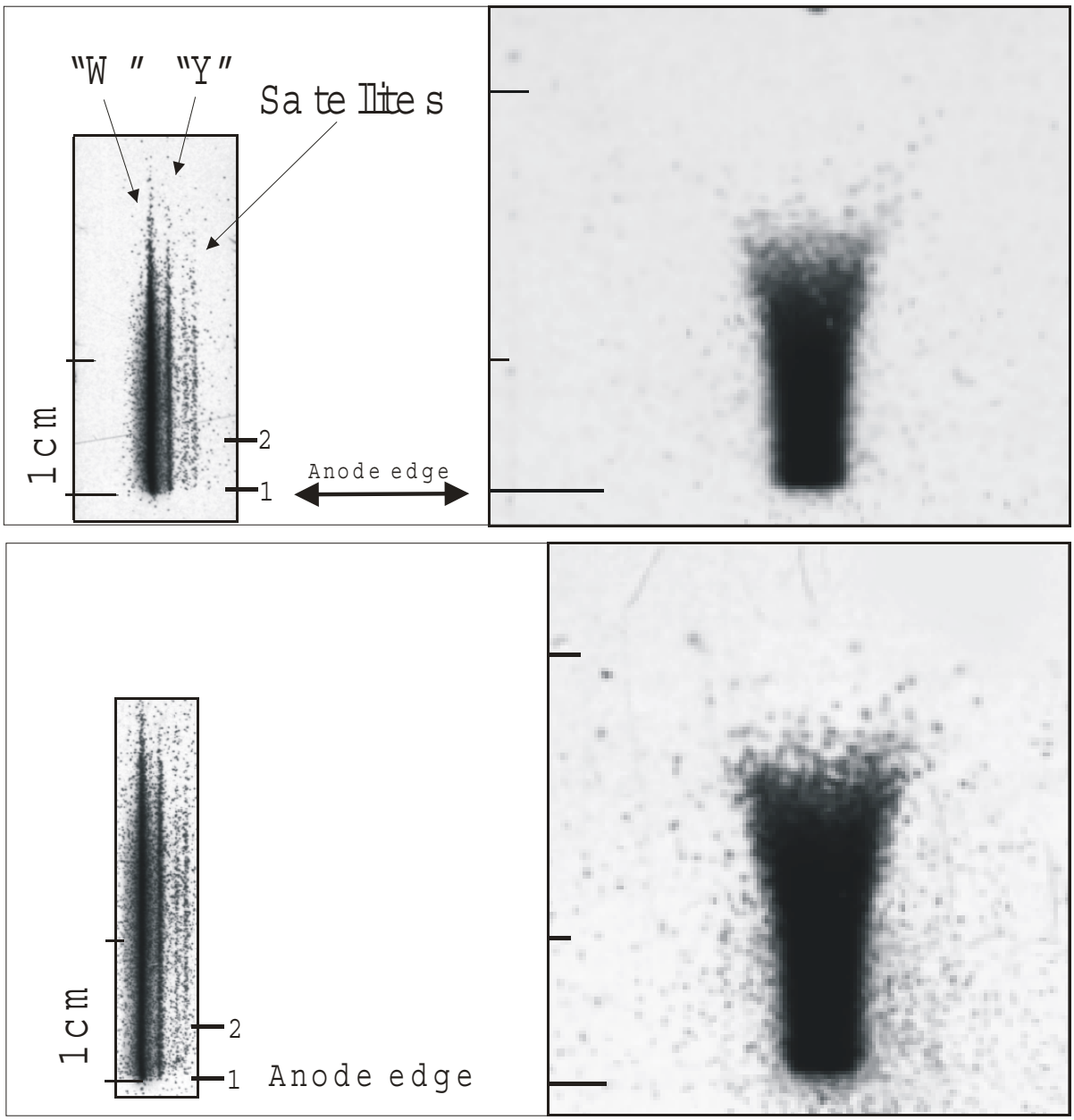

Figure 5-15.First stage of compression, t=-5ns (upper), +-5ns (lower) image.

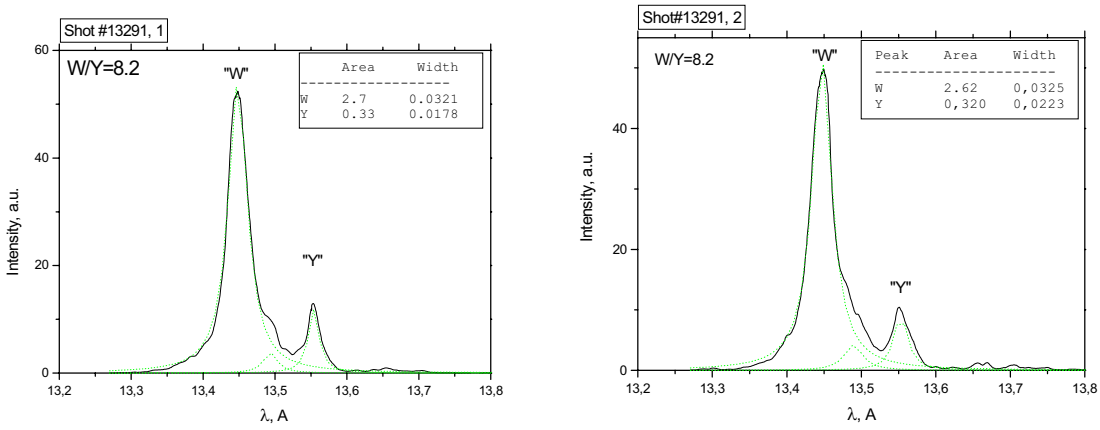

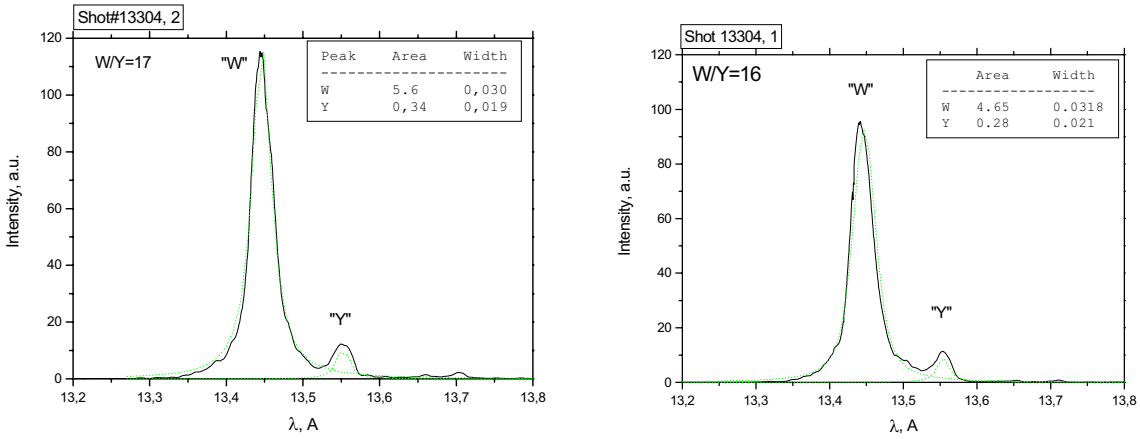

Figure 5-16. Spectra of Fig 5-15, upper- t=-5ns, lower – t=+5ns

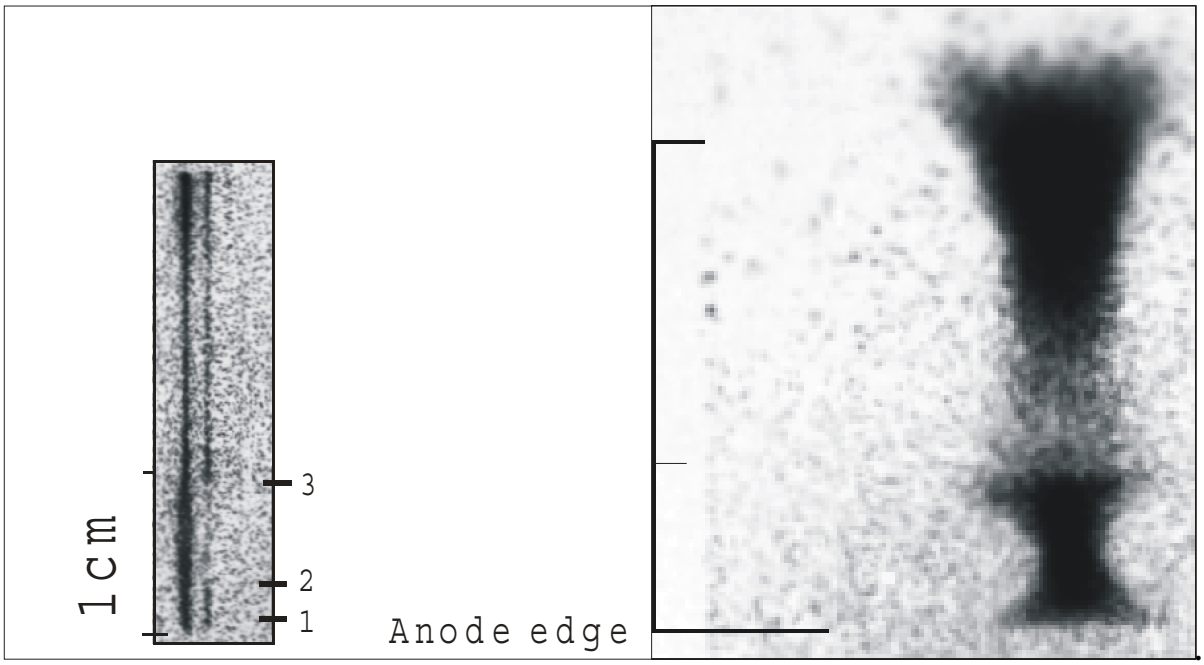

Figure 5-17. Compression 1, t=10-20ns

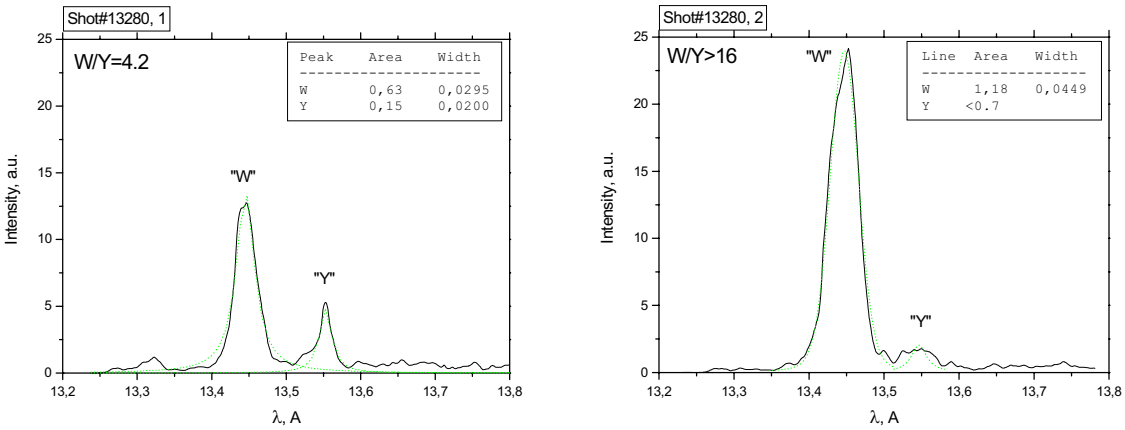

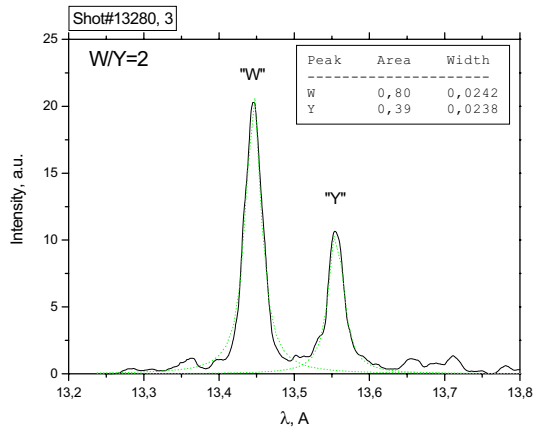

Figure 5-18. Spectra densitograms of Figure 5-17.

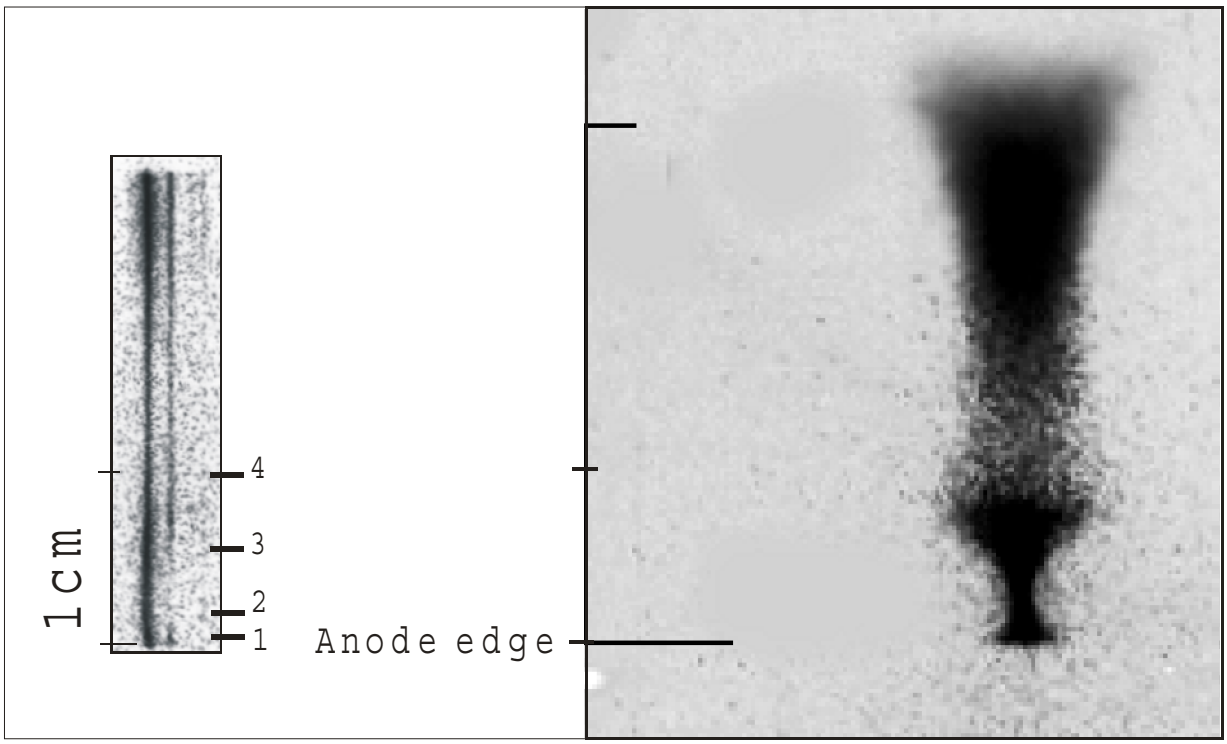

Figure 5-19. Compression 2, t=20ns

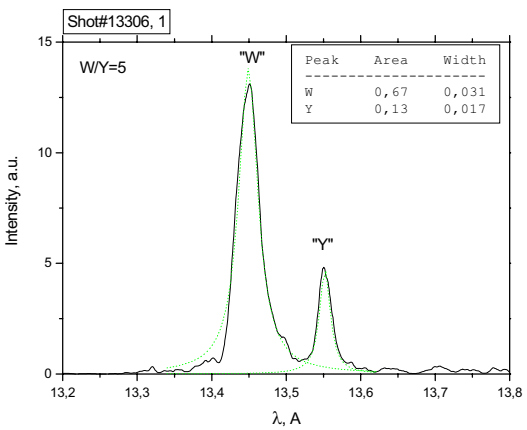

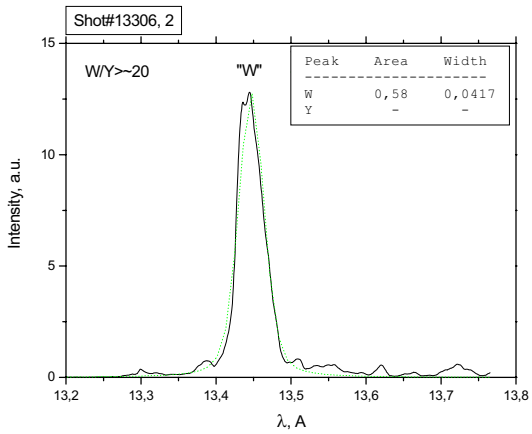

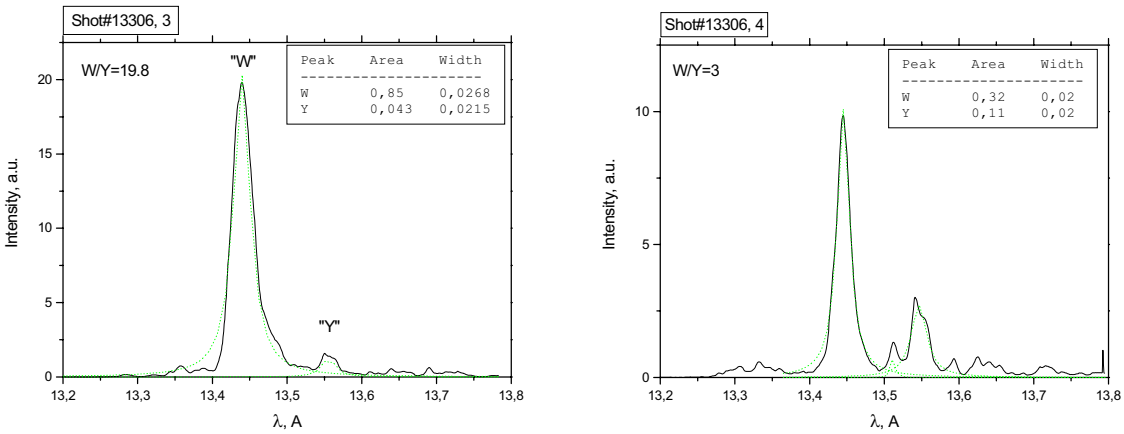

Figure 5-20. Spectra densitograms of Figure 5-19.

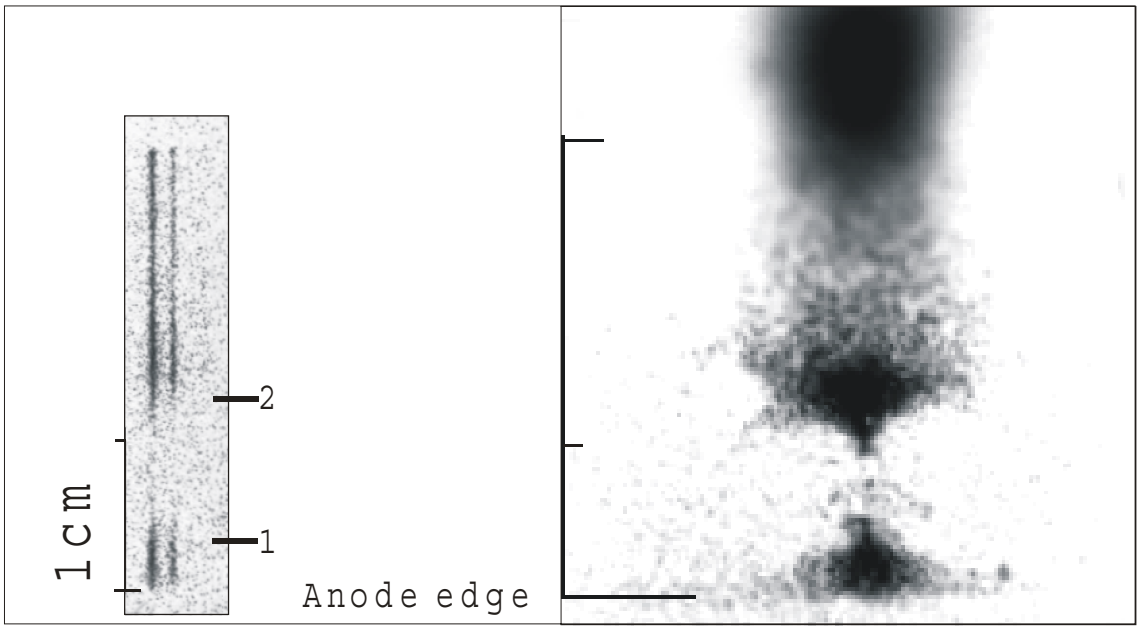

Figure 5-21. Compression 3, t=20-30ns

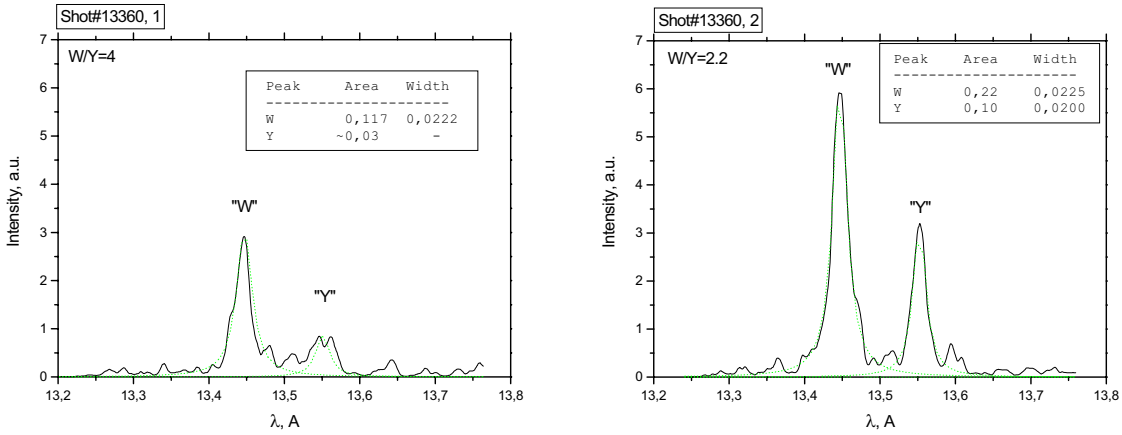

Figure 5-22. Spectra densitograms of Figure 5-21.

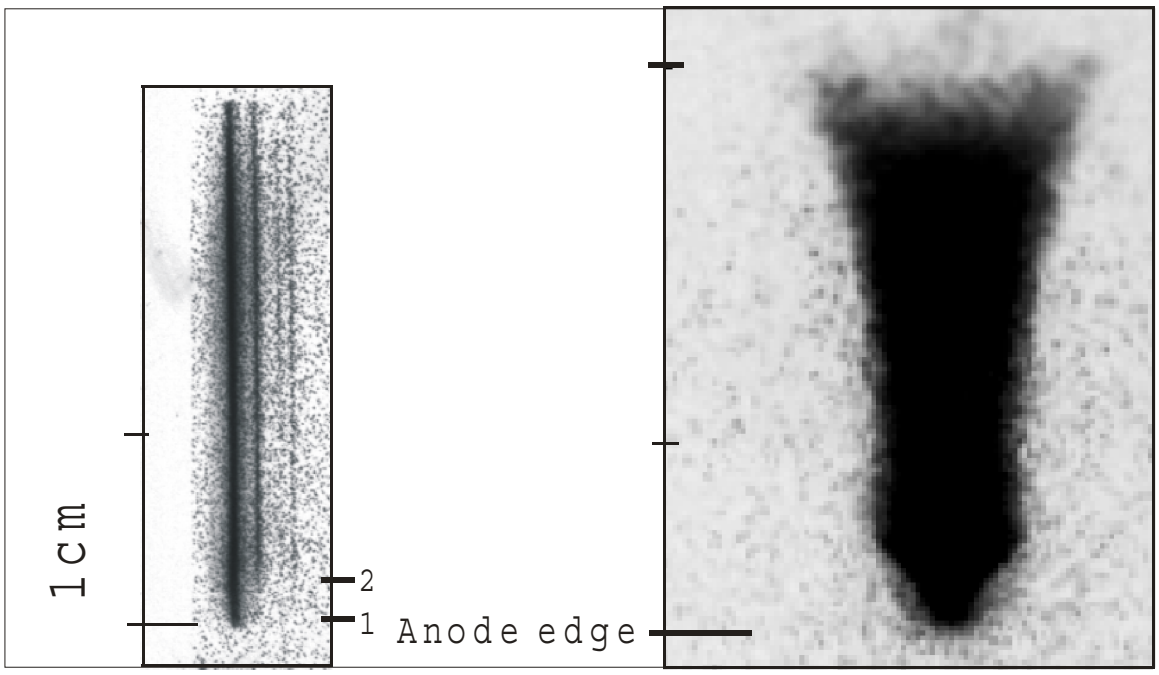

Figure 5-23. Instability II, t=+10ns

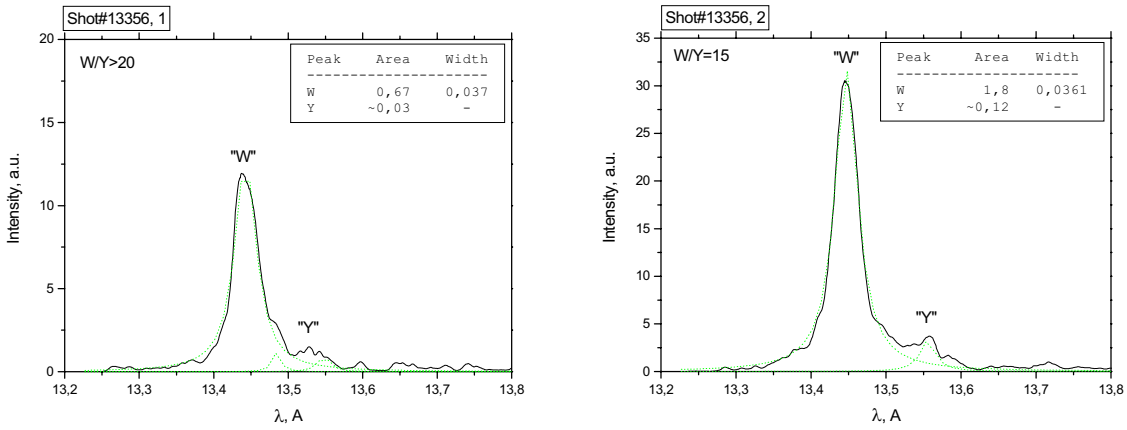

Figure 5-24. Spectra densitograms of Figure 5-23.

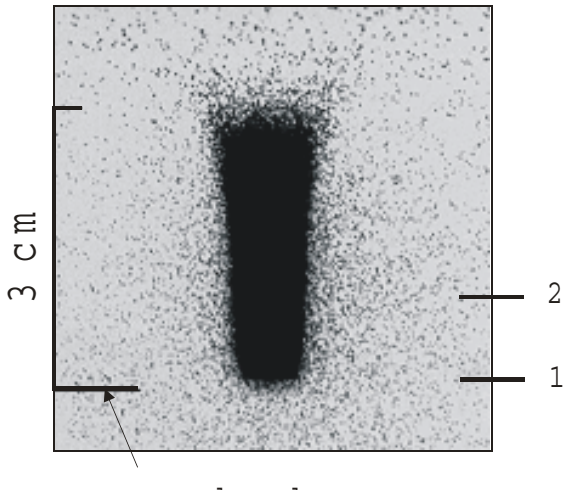

Figure 5-25. Plasma column.

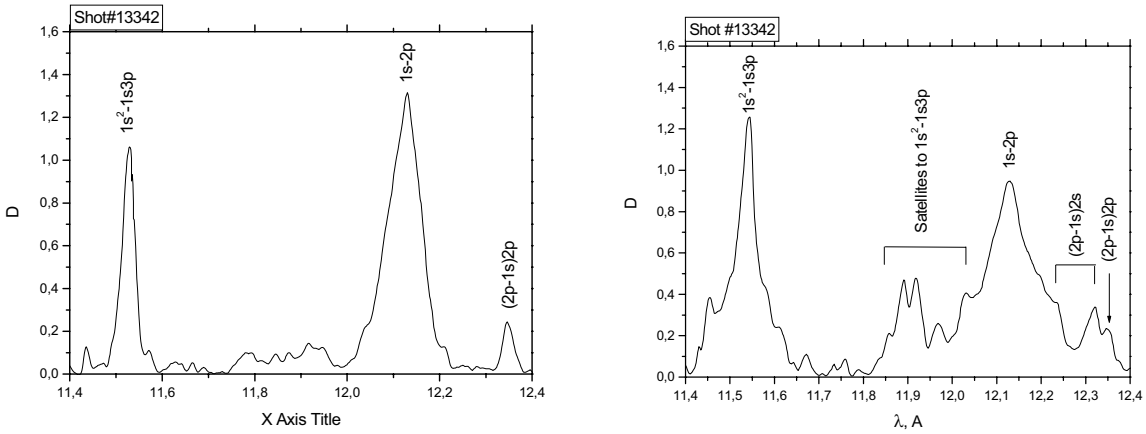

Figure 5-26. Spectra of Figure 5-25, the left spectrum corresponds to pos.1, the right – to the pos.2.

5-10ns after neck appearance (t≈+20ns on the absolute time scale) the neck is compressed to 1mm in diameter. On z-positions where the Y-line vanishes from the spectra, the method of electron density determination based on W/Y ratio can give only a lower limit $n_e \geq 5 \cdot 10^{19}$ cm^{-3}.

At the moment of pinch development t=+(25-30) ns the image of the narrow plasma column disappears on pinhole pictures (Figure 5-21). At the same z-position on spectra W and Y lines also disappear, most probably indicating that pinch development is accompanied by a strong increase of electron temperature, leading to a shift of ionization balance to H-like ions or bare nuclei.

The further development of the pinch leads to a situation described in chapter 4, when the thin plasma column, developed from the instability, cannot longer be seen on the MCP. In Figure 5-21 the pinhole image showing this situation is presented together with the corresponding spectrum, taken in the same shot at the same time.

At z-positions corresponding to empty regions on pinhole images, no resonance line and no intercombination line can be seen in the spectrum.

The instability of type II and the corresponding spectrum of W and Y lines are shown in Figure 5-23. It can be observed that near the anode, where the plasma column exhibits a neck on the pinhole image, no Y line is seen in the spectrum, which corresponds to $n_e \geq 5 \cdot 10^{19}$cm^{-3}.

In Figure 5-25 and Figure 5-26 a plasma column with spectra, corresponding to different z-positions are shown. The spectra were recorded in a wavelength region (11.4-12.5Å) (Figure 5-26) and contain transitions 1s3p-1s^2 of He-like neon and 1s-2p of H-like neon. The spectrum presented in Figure 5-26 (right) shows also satellites to the 1s-2p transitions as well as to the 1s3p-1s^2. Electron temperature can be estimated from the ratio of

$2p^2(^1D_2)$-$1s2p(^1P_1)$ satellite to the resonance line of H-like ion, and was found to be approximately 350-400eV.

The appearance of the satellites to the $1s3p$-$1s^2$ transition possibly indicates that on the corresponding z-position the temperature is lower than near the anode. The anomalous intensity of $2p^2(^3P)$-$1s2p(^3P)$ satellite group at 12.32Å indicates a high electron density [Bayanov 1976]. For low electron densities the intensity ratio of two satellites is proportional to ratio of their q-factors (Section 5.3). The q-factor for $2p^2(^3P)$-$1s2p(^3P)$ (Table 5-2) is equal to zero and in low-density plasmas this satellite group is not seen. These satellites originate from levels, which in LS coupling approximation cannot be populated by dielectronic capture. For the real atomic structure of Ne IX with slight deviations from LS-coupling scheme, rates of dielectronic capture and consequently q-factors of the multiplet lines are low (see Table 5-2). Another possible mechanism of population for these levels would be double electron excitation from the ground level of He-like ion ($1s^2$) + e → ($2p^2$), but it has a very low probability. When the electron density in a plasma increases the $2p^2(^3P)$ level starts to be collisionally populated from the $2s2p(^3P)$ state, and the satellite group appears in the spectrum. For low-Z ions the wavelengths of the $2p^2(^3P)$-$1s2p(^3P)$ satellite transition are well separated from the wavelengths of the $2s2p(^3P)$-$1s2s(^3S)$ transition and therefore determination of the electron density is possible.

In [Seely 1981] a characteristic electron density is defined as a density when this population redistribution effect starts to be important

$$N_e^* = \frac{A}{C} = (5.79 \times 10^{14}\, cm^{-3})(Z-0.7)^2 \times (Z-1)^{0.22} Z^{4.1} T_e^{0.28}, \qquad \textbf{Eq 5-6}$$

where A is the radiative decay rate of the $2p^2(^3P)$ level and C the $2s2p(^3P)$- $2p^2(^3P)$ electron excitation rate.

The $2p^2(^3P)$-$1s2p(^3P)$ line is density dependent for electron densities of the order of N_e^* [Seely 1981]. For Z=10 and T_e=400eV $N_e^* = 5 \cdot 10^{21}\, cm^{-3}$.

5.5 Possible influence of optical thickness effects.

As seen in the spectra the plasma under study is optically thick for the resonance line of He-like ions. We cannot exclude that ***Ly$_\alpha$*** transition of H-like Ne X may have substantial optical thickness. Therefore we are going to estimate a possible influence of the optical thickness on results of the determination of plasma parameters.

It is understandable that one can use an optical thin approximation when the yield factor "Y" from Eq 2-12 is close to 1

$$Y = \frac{1}{1 + \gamma / \Theta}. \qquad \textbf{Eq 5-7}$$

At the moment of the deepest compression when line radiation could be detected the plasma column diameter was about 0.1 cm (Chapter 4). The electron density measured by using ***"W"*** and ***"Y"*** was estimated as $N_e \approx (2\text{-}3)\cdot 10^{19}$ cm^{-3}, and the electron temperature close to $T_e \approx 400$ eV. The absorption coefficient for a spectral line is given by Eq 2-13, where we can neglect the influence of stimulated emission due to very low populations of excited levels

$$\sigma_\omega^{lu} = \frac{1}{4}\lambda^2 \frac{g_{up}}{g_l} a_\omega, where - a_\omega \approx \frac{A_{ij}}{\Delta\omega_{ij}} \quad , \qquad \textbf{Eq 5-8}$$

where $\Delta\omega_{ij}$ is an effective line width. Absorption is strongly reduced in compressing or expanding plasmas due to Doppler shift between spectral profiles of radiation and absorption for parts of the plasma moving in different directions or with different velocities.

This problem has been discussed by Schulz et al. [1994] and it was shown that an adequate description can be achieved by introduction of effective $\Delta\omega_{ij}$ accounting for plasma motion. For differentially expanding (compressing) cylindrical plasmas where the radial velocity at the coordinate r is

$$v(r) = \frac{r}{R} \cdot V_R \qquad \textbf{Eq 5-9}$$

and the plasma edge velocity V_R is the ionic-sound velocity

$$V_R \approx V_{IS} = \sqrt{\frac{(Z+1)\cdot kT_e}{M}} \qquad \textbf{Eq 5-10}$$

an equivalent line width is

$$\Delta\omega \approx \omega \cdot \frac{1.5 \cdot V_{IS}}{c} \quad , \qquad \textbf{Eq 5-11}$$

where c is the speed of light. For resonance transitions in K-ions of neon with a quantum energy about 1000 eV in a plasma with and $T_e \approx 400$ eV, $\Delta\omega_{ij} \approx 10^{15}$s^{-1} and the absorption cross section $\sigma \approx 2\cdot 10^{-17}$cm^2. In a plasma with a characteristic size 0.1 cm and electron density $N_e \approx 2 \cdot 10^{19}$cm^{-3} it corresponds to the upper limit of the optical thickness $\tau \leq 6$. The escape factor Θ can be estimated from approximation formulas given in [Irons 1979] and [Fill 1988] and also from Monte-Carlo calculations [Schulz 1992] and varies from 0.1 to 0.2. The

coronal coefficient γ can also be estimated assuming that for resonance levels (n=2) of He- and H-like ions the strongest collisional depopulation channel will be excitation to the level with a principal quantum number n=3. Using the Van-Regemorter formula (Eq 5-4) one can finally get $\gamma \approx 10^{-2}$. That in turn gives a value of the yield factor Y in the range between 0.9 and 0.95, thus justifying the usage of the optical thin approximation for resonance lines of He- and H- like ions.

No absorption is expected for the intercombination line of He-like ion due to a very low radiative decay rate and also for dielectronic satellites to the resonance line of H-like ions due to negligible population of lower levels (1s 2l) of these transitions.

6 Discussion

Pinch modes produced in the SPEED2 plasma focus are usually divided into two types: the micropinch mode (MPM) and the stable column mode (SCM) with a transition regime where both modes can be observed. The transition regime can be shifted to either the MPM or the SCM by changing the energy density of the sheath and the pinch.

Recently two dissertations on characterizing the MPM [Röwekamp 1996] and the SCM [Berntien 2000] were performed. In these works it has been found that comparatively dense and cold sheaths and plasmas result in necking and micropinches, while fast and hot sheaths tend to forming the SCM.

The development of micropinches is well described by the radiative collapse theory as a compression of necked plasma regions in presence of strong energy losses from the plasma due to line radiation. For hydrogen plasmas the current value, at which radiative losses due to Bremsstrahlung are balanced by ohmic heating is known as the Pease-Braginskii current. For heavier gases, the Pease-Braginskii current can be considerably reduced, because line radiation strongly affects the energy balance of pinches.

As is seen from Eq.1-1 the Pease-Braginskii current depends on the effective charge of ions in the pinch plasma and on the plasma temperature. Micropinches are actuated from plasma instabilities, when the current through the plasma is above the Pease-Braginskii current. So the plasma should be relatively cold, for L ions (which have strong line radiation) to be still abundant. If the pinch plasma consists of K-ions and bare nuclei then instabilities do not develop into micropinches (Chapter 1).

Tendencies for development of the SCM and the MPM can also be discussed in terms of energy input per plasma particle (energy density). Low energy density results in ionization stages with strong line emission, and can therefore lead to formation of micropinches. High energy density results in high ionization stages of the pinch constituents and actuation of micropinches by radiative collapse is hindered.

When operating SPEED2 in the SCM regime, requirements for actuation of the radiative collapse in plasma necks are not met and MPs are not formed. The stability of the plasma column, which should be subject to numerous instabilities cannot be explained in this way. A few stabilization mechanisms, which explain why instabilities are suppressed in the column mode of the plasma focus operation, were proposed elsewhere. One of them is the

GRAM, which is being developed in the Institut für Experimentalphysik, Universität Düsseldorf.

In the present work a further investigation of the SCM at the SPEED2 plasma focus with injection of neon is presented. Different from the previous work on SCM, extensive diagnostics have been applied to obtain detailed information about plasma parameters during the pinch phase. Time-resolved x-ray pinhole imaging was used simultaneously with spatially resolved x-ray spectroscopy of K-ions of neon. For the first time it was possible to observe the local development of spectral features of the plasma column together with dynamics of its density and eventually temperature.

Since the SCM is favored by high energy density, it should be possible to obtain the SCM in low energy machines, provided the energy density can be kept constant. The task of determining the energy delivered from the power supply to a plasma is rather complicated, so the SCM or MPM regime can be accurately determined post factum.

The diameter of the anode in the present experiment was smaller and the energy of the SPEED2 current driver was lowered in order to keep the energy density about constant.

Time-integrated pinhole imaging was used to obtain first general information about plasma produced in the discharge. On images produced by radiation with wavelength shorter than 2nm, the plasma is seen mostly as a thin (<0.5mm in diameter), short (<4mm) bright plasma filament embedded on-axis into a diffuse column of diameter 1.4-1.8mm and 1-2cm in lengths. Interesting to note, that the aspect ratio remains about the same for the diffuse column and the bright filament. Analyzing the optical density of pinhole images produced behind different filters the effective wavelength of radiation originating from the pinch plasma was found to be around 0.3nm. This allowed concluding that the pinhole image is formed mostly by continuum radiation. From more detailed analysis of filtered pinhole images, and assumption that the plasma is thermal, an electron temperature of the bright plasma filament was determined to be approximately 1-2keV, and that of the diffuse column about 700eV.

The dynamics of the pinch was investigated using simultaneously time-resolved pinhole imaging and spectroscopy of K-ions. The results have shown that after the plasma column (about 2cm in length) with temperature around 400eV, electron density $6 \cdot 10^{18} cm^{-3}$ is formed on axis, large scale neck type instabilities start to develop near the anode surface with a ionic-sound velocity of 10^7 cm/s. In the neckings the plasma is compressed to a radius <0.3mm and to electron densities higher than $5 \cdot 10^{19}$ cm^{-3}. Further development of instabilities shows that the He-like neon, used in spectroscopic diagnostics, vanishes completely from the necked regions. The spectra of the resonance and intercombination lines of neon as well as

corresponding pinhole images have a fading region on the position where the instability starts. This could be explained by strong heating of the pinch in the compressed region, due to particle outflow [Vikhrev 1978].

We compared time-integrated images with corresponding time-gated images (if available). The instability is recorded on the time-integrated images as a thin bright plasma filament, while the pinch itself contributes to the image of the diffuse column.

Possibly, a second compression noticed in the previous work on characterizing the SCM [Berntien 2000], was the instability development as recorded in the present work.

In terms of modes produced in the SPEED2 plasma focus, we operated in the transition regime between MPM and SCM. Apparently, the energy density of the discharges with reduced dimensions and bank energy was lower than before. The energy per gas particle can be further increased by decreasing the amount of injected gas. Unfortunately, there is a minimum of gas injection for the SPEED2 system below which the radiation from the pinch plasma is poor. Therefore, further efforts are necessary to establish the SCM reproducibly in small-scale experiments.

References

[Abramov & Kogan 1966] Abramov V A, Kogan V I, Sov. Phys. Doklady **10**, 1966

[Alexandropoulos 1974] Alexandropoulos N.G. and Cohen G.G., Appl.Spectroscopy, **28**(2), 1974:155

[Antsiferov et al 1990] Antsiferov P S, Koshelev K N, Krauz V I, Sidelnikov Yu V, Khautiev E Yu, and Yartseva O N, Fizika Plasmi **16**(11), 1990:1319

[Antsiferov et al 1991] Antsiferov P S, Koshelev K N, Krauz V I, Sidelnikov Yu V, Khautiev E Yu, Optika&Spectroscopy **70** , 1991:747

[Antsiferov et al 1995] Antsiferov P S, Rosmej F B, Rosmej O N, Schmidt H, Schulz D, and Schulz A, J.Appl.Phys.**77**(10), 1995:4973

[Bateman 1977] Bateman J.E., Nucl. Instrum. Methods 144, 1977:537

[Bayley et al 1991] Bayley J M, Decker G, Kies W, Malzig M, Rowekamp P, Westheide J, and Sidelnikov Yu, J.Appl.Phys. **69**(2), 1991:613

[Bennett 1934] Bennett W.H., Phys. Rev., **45**, 1934 :890

[Bhalla 1975] Bhalla C.P.; Gabriel A.H.; Presnyakov L.P., Mon.Not.Roy.Astronom.Soc, **172**, 1975:359

[Bobashev et al 1996] Bobashev S V, Simanovskii D M, Platonov Yu Ya, Rowekamp P, Decker G, Kies W, Plasma Sources Sci. Technol. **5**, 1996:578

[Braginskii 1961] Braginskii, S.I., Plasma Physics and the Problem of Controlled Thermonuclear Reactions, v.**I**, 1961

[Cohen 1968] Cohen L, Feldman U, Swartz M, and Underwood J H, J.Opt. Soc.Am. **58**, 1968:843

[CXRO] www-cxro.lbl.gov

[Decker et al 1980] Decker G. and Herold H., Phys. Blätter, **36**(11), 1980:328

[Decker et al 1983] Decker G., Kies W., Pross G., Phys. Fluids, **26**(2), 1983 :571

[Decker at al 1986] Decker G, Kies W, Malzig M, van Calker C, and Zieten G, Nucl.Instrum.Methods Phys.Res., Sect.A **249**, 1986:477

[Decker at al 1996] Decker G, Kies W, Nadolny R, Rowekamp P, Schmitz F, Zieten G, Koshelev K N, Sidelnikov Yu V, and Sopkin Yu V, Plasma Sources Sci. Technol. **5**, 1996:112

[Deutsch et al 1986] Deutsch R, Kies W, and Decker G., Plasma Phys. Control. Fusion **28**, 1823

[Eberhardt 1979] Edward E. Eberhardt, Gain model for microchannel plates, Applied Optics 18(9), 1979:1418

[Filippov 1983] Filippov N.V., Fiz.Plasmy **9**, 1983:259

[Fill 1988]: Fill E E, JQSRT **39**, 1988:489

[Gabriel 1972]: Gabriel A, MNRAS **160**, 1972:99

[Gabriel et al 1972] Gabriel, A. and Jordan, C. Case studies in atomic collision physics, v.**2**, 1972

[Giudicotti 1994] L. Giudicotti, M. Bassan, R. Pasqualotto, and A. Sardella, Rev. Sci. Instrum. 65(1), 1994:247

[Griffen and Peacock 1966] Griffen W, Peacock N.J., Bull. Inst. Phys. Soc., **17**, 1966:229

[Henke et al 1984a] Henke B.L.; Kwok S.L.; Uejio J.Y.; T.Yamada H.; Young G.C., J.Opt.Soc.Am. B, **1**(6), 1984 :818

[Henke et al 1984b] Henke B.L.; Fujiwara F.G.; Tester M.A.; Dittmore C.H.; Palmer M.A., J.Opt.Soc.Am. B, **1**(6), 1984 :828

[Henke et al 1986] Henke B.L.; Uejio J.Y.; Stone G.F.; Dittmore C.H.; Fujiwara F.G., J.Opt.Soc.Am. B, **3**(11), 1986 :1540

[Henke et al 1993] Henke B.L.; Gullikson E.M.; Davis J.C., At. Data Nucl. Data Tables, **54**(2), 1993

[Holstein 1947] Holstein T, Phys. Rev. **72**, 1947:1212

[Holstein 1951] Holstein T, Phys. Rev. **83**, 1951:1159

[Ilford] www.ilford.com

[Irons 1979]: Irons F E, JQSRT **22**, 1979:1

[Irons 1979a]: Irons F E, JQSRT **22**, 1979:21

[Irons 1979b]: Irons F E, JQSRT **22**, 1979:37

[Irons 1990]: Irons F E, JQSRT **44**, 1990:361

[Khautiev et al 1988] Khautiev E Yu, Krauz V I, Reshetniak N G et al, Proc.12 International Conference on Plasma Physics and Controlled Fusion, Nice, **2**,1988:579

[Kies 1982] Kies W, Doktorarbeit, Universität Düsseldorf 1982

[Kies et al 1998] Kies W, Lucas B, Rowekamp P, Schmitz F, Ziethen G, and Decker G. , Plasma Sources Sci Technol. **7**, 1998:21

[Kies et al 2000] Kies W, Decker G, Berntien U, Sidelnikov Yu V, Glushkov D A, Koshelev K N, Simanovskii D M, Bobashev S V, Pinch modes produced in the SPEED2 plasma focus, Plasma Sources Sci. Technol. 9, 2000:279

[Korop et al 1979] Korop E D, Meierovitch B E, Sidelnikov Yu V, and Suhorukov S T, Usp.Fiz.Nauk **129**, 1979:87 (Sov.Phys.Usp.**22**, 727)

[Koshelev et al 1988] Koshelev K N, Krauz V I, Reshetniak N G , Salukvadze R G, Sidelnikov Yu V, and Khautiev E Yu, J.Phys.D:Appl.Phys. **21**, 1988:1827

[Koshelev et al 1991] Koshelev K N, Pereira N R, J.Appl.Phys. **69**(10) 1991:R21-44

[Koshelv et al 1994] K. N. Koshelev, Yu. V. Sidelnikov, G. Decker, V. Kies, M. Malzig, P. Rowekamp, F. Rozmej, A. Schulz, H.-I. Kunze, Optics and Spectroscopy **76(**2), 1994:202

[Kunze et al 1968] Kunze, H.-J., Gabriel A., Griem H.R., Phys. Rev., **165**, 1968:267

[Lebert et al 1995] Lebert R, Engel A, and Neff W, J.Appl.Phys. **78**(11) 1995:6414

[Lee 1995] Lee R W, manual for FLY, 1995

[McWhirter 1965] McWhirter, R.W.P. Plasma diagnostic techniques, 1965

[Peacock et al 1969] Peacock N J, Speer R J, and Hobby M G, J.Phys.B **2,** 1969:798

[Pease 1957] Pease R., Proc. Phys. Soc. London, **B70**, 1957 :11

[Ralchenko 2001] Yu.V.Ralchenko and Y.Maron, JQSRT, 2001 (to be published)

[Rapp 1973] Rapp H., Experimentelle Untersuchung der Betriebscharakteristik eines Plasmafocus, Doktorarbeit, Universität Stuttgart,1973

[Rybicki 1984]: Rybicki G B, “Methods in Radiative Transfer”, Cambridge Univ.Press, Cambridge.

[Schulz 1992]: Schulz A, “Der Mikropinch im Vacuumfunken als Quelle harter Roentgenstrahlung” , Doktorarbeit Ruhr-Universitaet Bochum, 1992.

[Schulz et al 1994] Schulz A, Hebach M, Kunze H-J, Rosmej F R, Walden F, JQSRT **51**(1/2), 1994:341

[Shikaliev 1997] Shikhaliev P.M., Rev.Sci.Instrum 68(10), 1997:3676

[Skobelev et al 1978] Skobelev I. Yu., Vinogradov A.V., Yukov E.A., Physica Scripta, 18, 1978:78

[Sobelman et al 1981] Sobelman I I, Vainshtein L A, Yukov E A, Excitation of Atoms and Broadening of Spectral Lines, 1981

[Vainshtein et al 1978] Vainshtein L.A. and Safronova U.I., At. Data Nucl. Data Tables, **21**(1), 1978:49

[Van Regemorter 1962]: Van Regemorter H, Ap.J. **136**, 1962:906

[Vikhrev 1977] Vikhrev V.V., Sov.J.Plasma Phys. **3** (5), 1977

[Vikhrev et al 1977] Vikhrev V.V., Gureev K.G., Zhdanov S.K., Korzhavin V.M., Trubnikov B.A., Plasma Physics and Controlled Nuclear Fusion Research, Vol.3, IAEA, Vienna, 1977:455

[Vikhrev 1978] Vikhrev, V.V., Pis'ma Zh.Experim Teor.Fiz. **27,** 104

[Vikhrev et al 1982] Vikhrev V V, Ivanov V V, and Koshelev K N, Fiz.Plazmy **8**, 1982:1211 (Sov.J.Plasma Phys. **8**, 688)

[Vinogradov et al 1975] Vinogradov A.V., Skobelev I. Yu., Yukov E.A., Sov. J.Quant.Electron., 5, 1975:630

[Walsh 1957] Walsh P J, Phys. Rev, **107**, 1957:338

[Witz 1969] Witz I., Acta Crystal, **A25**(1), 1969 :30

[Wiza 1979] Wiza J.L., Nucl.Instrum. Methods 162, 1979

Appendix.

A. Calculation of η(ν,I) factor.

To calculate a coefficient η a next approach can be explored. Generally an emulsion is a heterogeneous system of AgBr grains embedded in gelatin with a volume fraction of AgBr equal to V. For a highly dispersed mixture, when AgBr-grain size is small compared with the reciprocal linear absorption coefficient of AgBr, the system can be considered homogeneous. The homogeneous absorption coefficient is given by

$$\mu^{/} = (1-V)\mu_0 + V\mu_1 \qquad \textbf{Eq. A-1}$$

The general case was studied by Henke et al [Henke 1984a]. The heterogeneous system is modeled as a system of s layers of thickness d equal to the effective grain size, with the grains absorbing as equivalent, aligned cubes. It is assumed that the total optical transmission of the emulsion may be given by the product of the monolayer-section transmissions. A full model for calculation of ***η(ν,I)*** factor is given in Appendix A. Thus, x-ray transmission factor for the heterogeneous absorber is an averaged value for a large number of incident photons:

$$\tau = \sum_{0}^{s} p_n \tau_n = \exp(-\mu^{/} x) \qquad \textbf{Eq. A-2}$$

where x is the total thickness of the absorber, n is the number of AgBr-grain encounters for a given photon passing through the s layers ranging from 0 to ***s***, $\boldsymbol{p_n}$ is the probability of having n encounters, $\boldsymbol{\tau}$ is an associated transmission factor for a photon passing through $\boldsymbol{n \cdot d}$ thickness of AgBr, multiplied by that for passing through (s-n)d thickness of gelatin. Within a monolayer, the probability of encountering one or no AgBr grains for a single photon passing through this layer is V or (1-V) respectively:

$$\begin{aligned} p &= V \\ q &= (1-V) \end{aligned} \qquad \textbf{Eq. A-3}$$

The photon can have an encounter in any of s layers. One possible outcome could be, for example:

$$P(n)_{n\le s} = \underbrace{p\underbrace{q..q}_{n}p..p}_{s} = q^n p^{s-n} \qquad \textbf{Eq. A-4}$$

The total probability of having n encounters is a sum of all possible outcomes, when the photon meets AgBr grain n times:

$$p_n = C_s^n P(n) = \frac{s!}{(s-n)!\,n!}(1-V)^{s-n}V^n \qquad \textbf{Eq. A-5}$$

The corresponding transmission is:

$$\tau_n = \exp(-\mu_0(x-nd)-n\mu_1 d) = \exp(-\mu_0 x)\exp(-n\Delta\mu d) \qquad \textbf{Eq. A-6}$$

Finding the sum of products and recalling the binomial formula, we obtain for the total transmission:

$$\begin{aligned}\tau &= \exp(-\mu_0 x)\sum_0^s \frac{s!}{(s-n)!\,n!}(1-V)^{s-n}(V\exp(-\Delta\mu d))^n \xrightarrow{\text{Binomial formula}} \\ &= \exp(-\mu_0 x)(1-V+V\exp(-\Delta\mu d))^s = \exp(-\mu' x)\end{aligned} \qquad \textbf{Eq. A-7}$$

Solving this equation for μ' we obtain:

$$\mu' = \mu_0 - \frac{1}{d}\ln(1-V(1-\exp(-(\mu_1-\mu_0)d))) \qquad \textbf{Eq. A-8}$$

B. Johann registration scheme

The crystal K, with the crystal lattice layers parallel to its surface, is elastically bent on a cylinder surface with radius R. X-rays from the source S incident on the crystal at the angle φ, are reflected according to the Bragg-Wolf as

$$2dSin(\varphi) = n\lambda \qquad \textbf{Eq. B-1}$$

where d is a period of the crystal lattice, λ - wavelength of the reflected radiation, n – reflection order.

All rays starting from the point Q on the Rowland circle (the circle of radius R/2) are focused around the point P of this circle. (The angle of incidence on the crystal is about the same.) Aberration PP' is proportional to the $(T/R)^2$, where T is the length of the working area

of the crystal [Witz 1969]. Detector is placed along the Rowland circle – the focal curve of the spectrograph. The range of angles of incidence for rays from the source define the spectrum region.

Spectral dispersion is

$$\frac{d\lambda}{d\varphi} = \frac{2d}{n} Cos(\varphi) \qquad \textbf{Eq. B-2}$$

Usually dispersion is calculated for the detector plane coordinates:

$$\frac{d\lambda}{dl} = \frac{2d}{nR} Cos\varphi = \frac{\lambda}{R} Ctg\varphi \qquad \textbf{Eq. B-3}$$

The spectral coverage for a point-like source placed inside of the Rowland circle at the distance *a* from the crystal is given by

$$\Delta\lambda = \lambda T \frac{\rho - a}{aR} Ctg\varphi = \frac{2d}{n} \frac{T(\rho - a)}{aR} Cos\varphi \qquad \textbf{Eq. B-4}$$

where $\rho = RSin\varphi$ - the distance from the Rowland circle to the crystal center at the angle φ. It can be seen that for a given spectral resolution, the viewing range can be increased only by placing the source closer to the crystal.

The viewing range is greater for the source of the finite size 2*r* than for the point-like:

$$\Delta\lambda = \lambda T \frac{\rho - a}{aR} \left[1 + \frac{2r\rho}{(\rho - a)TSin\varphi} \right] Ctg\varphi \qquad \textbf{Eq. B-5}$$

The crystal for the x-ray spectrograph is chosen from considerations about the working wavelength range (λ<2d, where d is the period of the crystal lattice). Natural or synthetic crystals with d=1-14Å are available [Alexandropoulos 1974].

Spectral resolution. Instrumental function.

Instrumental function width is determined by several reasons.

Inherent geometrical line broadening of the Johann scheme is due to aberrations of the monochromatic rays reflected by the crystal:

The distance PP$^{/}$ is $\Delta l = \frac{T^2}{8R} Ctg\varphi$, so the aberrational line broadening is given by

$$\frac{\Delta\lambda_1}{\lambda_1} = \frac{T^2}{8R^2} Ctg\varphi \qquad \textbf{Eq. B-6}$$

for a point-like source. For the source with size $2r$

$$\frac{\Delta\lambda_1}{\lambda_1} = \frac{1}{8}\left(\frac{2r}{\rho - a}\right)^2 Ctg^2\varphi \qquad \textbf{Eq. B-7}$$

Astigmatism of the cylindrical crystal surface results in geometrical broadening of spectral lines. If h – is the effective crystal height, then

$$\frac{\Delta\lambda_2}{\lambda} = \frac{h^2}{8R^2} Ctg^2\varphi \qquad \textbf{Eq.B-8}$$

From Eq. B-7 and Eq.B-8 it follows, that in order to reduce this broadening effect, h should be taken smaller than T.

Spectral resolution of the spectrograph is limited by the physical parameters of the crystal. If the rocking curve width is $\delta\varphi$, then the associated line broadening is

$$\frac{\Delta\lambda_3}{\lambda} = \delta\varphi Ctg\varphi \qquad \textbf{Eq.B-9}$$

Characteristics of some crystals used in x-ray spectroscopy are reported in [Henke et al 1993].

Another possible source of error can be the slanted incidence of x-rays on the film emulsion, if the film is used as a detector. This type of broadening is negligible for single emulsion films.

If an MCP detector is used, then the line width and the spectral resolution of the diagnostic system can be affected, because the positional resolution of the MCP is limited by the size of an MCP channel.

C. Free-Free (Bremsstrahlung) Radiation

Two kinds of processes contribute to the continuous spectrum. The first is the Bremsstrahlung radiation. The emission spectrum of this radiation for H-like ions with a charge Z is obtained by averaging the emission rate from a single electron over the Maxwellian distribution of velocities.

$$dI_{ff}(h\nu) = \frac{32}{3}\left(\frac{\pi}{3}\right)^{1/2} r_0^2 c\left(\frac{\chi_H}{T_e}\right)^2 Z^2 n_i n_e \exp(-\frac{h\nu}{kT_e}) d(h\nu), \qquad \textbf{Eq. C-1}$$

where $r_0=e^2/mc^2=\alpha^2$, $a_0=2.818\cdot10^{-13}$cm, is the electron electromagnetic radius, c is the speed of light, $\chi_H=13.605$eV is the binding energy of a ground state hydrogen, and n_i, and n_e are the ion and electron densities respectively. $dI_{ff}(h\nu)$ is the energy in eV emitted into 1eV per unit time and per unit volume. This equation was derived from the classical considerations. To account for quantum mechanical effects, a multiplicative Gaunt factor G_{ff} should be incorporated into the equation. For practically interesting cases, the Gaunt factor is quite close to unity.

When ions of more than one charge state are present the emission must be summed over the various kinds of ions, or the charge state can be substituted by an average charge state.

Acknowledgements.

The work was carried out in the Instutut für Experimentalphysik, Heinrich-Heine-Universität Düsseldorf. I would like to thank Prof. Dr. W.Kies and Prof. em. Dr. G.Decker for accepting me into the Fokusgruppe and providing me with an interesting subject and the object of study.

I thank Herr Prof. Dr. Kies for being always ready to discuss the results, for supporting me during these three years, for careful reading of the manuscript and making valuable proposals on its refinement.

I am thankful to Herr Prof. Dr. Decker for ever-warm reception and the attention I received from him in these years.

I am especially grateful to Dr. Konstantin Koshelev (Head of the Plasma Spectroscopy Laboratory, Institute of Spectroscopy, Troitsk), who was always near for advises and discussions not only of scientific subjects.

To Dr.Yu.V.Sidelnikov (Institute of Spectroscopy) I am thankful for help in obtaining experimental data and discussions. Him and Dr. D. Simanovskii I would like also to thank for my first experimental sessions on the SPEED2.

Graduirtenkolleg and Deutsche Forschungsgemeinschaft (DFG) provided me with the financial support. Without it the work couldn't have been carried out.

I am thankful to all colleagues of the Institute of Spectroscopy and the Institut für Experimentalphysik, especially to Herr G. Ziethen, who perfectly kept the SPEED2 functioning. I thank Dr. Peter Röwekamp for that he was always ready to answer every my question. Frau Silke Rosenbohm was patient enough to speak german with me from the beginning and provided with necessary help on many subjects.

I thank my wife for being with me. I am very grateful to my parents for everything I ever received from them, especially to my mother.